

Maren Elise Rognerud

How to avoid gas supersaturation in the river downstream a hydropower plant

June 2020



Norwegian University of
Science and Technology

How to avoid gas supersaturation in the river downstream a hydropower plant

Maren Elise Rognerud

Energy and Environmental Engineering

Submission date: June 2020

Supervisor: Bjørn Winther Solemslie

Co-supervisor: Ole Gunnar Dahlhaug, Bruno G. Pollet

Norwegian University of Science and Technology
Department of Energy and Process Engineering

MASTER THESIS

for
student Maren Elise Rognerud
Spring 2020

How to avoid gas supersaturation in the river downstream a hydro power plant

Hvordan unngå gassovermetting i elv nedstrøms et vannkraftverk

Background

In Norway, more than 10 hydropower plants are known to have caused biologically relevant levels of total dissolved gas supersaturation (TDGS, i.e. above 100 % saturation) in rivers, including fish kills, and more is expected to come due to the trend of increased floods. TDGS in hydropower facilities is an underexplored phenomena and recent studies indicates that it may be a “silent killer” for fish and invertebrates in both new and old hydropower systems. For example, in the 4 km of river downstream Brokke power plant, there were located none fish in a survey done in 2012. TDGS in hydropower facilities occur when pressurised water with high concentration of dissolved gas is exposed to atmospheric pressure in the downstream river. Major causes are spillway air injections and air entrainment at water intakes (often due to clogging of trash-racks), and the problems may be amplified due to hydropeaking (i.e. rapid changes in power generation).

This work will test a technical solution that has the potential to reduce dissolved gas supersaturation in water utilizing ultrasound.

Objective

Test a laboratory setup for reducing gas from water by utilizing ultrasound

The following tasks are to be considered:

1. Literature study
 - a. Gas supersaturation in hydropower plants
 - b. Operation of Francis turbines
2. Software knowledge
 - a. Labview will be used for laboratory measurements
 - b. Matlab will be used for the evaluation of measured data
3. Waterpower Laboratory at NTNU
 - a. Develop procedure to produce water with the desired total dissolved gas level
 - b. Develop and construct a laboratory ultrasonic degassing test rig
 - c. Installation and instrumentation of the test rig
 - d. Calibration of instrumentation utilized in the tests
 - e. Perform tests of degassing supersaturated water utilizing ultrasound
4. If the student is going to Nepal on an excursion, the previous work from the project and the further work in this master thesis will be written as a separate publication and presented at the conference: 10th International symposium on Current Research in Hydraulic Turbines (CRHT-X) at Kathmandu University 31st March 2020.

-- “ --

The work shall be edited as a scientific report, including a table of contents, a summary in Norwegian, conclusion, an index of literature etc. When writing the report, the candidate must emphasise a clearly arranged and well-written text. To facilitate the reading of the report, it is important that references for corresponding text, tables and figures are clearly stated both places. By the evaluation of the work the following will be greatly emphasised: The results should be thoroughly treated, presented in clearly arranged tables and/or graphics and discussed in detail.

The candidate is responsible for keeping contact with the subject teacher and teaching supervisors.

Risk assessment of the candidate's work shall be carried out according to the department's procedures. The risk assessment must be documented and included as part of the final report. Events related to the candidate's work adversely affecting the health, safety or security, must be documented and included as part of the final report. If the documentation on risk assessment represents a large number of pages, the full version is to be submitted electronically to the supervisor and an excerpt is included in the report.

According to “Utfyllende regler til studieforskriften for teknologistudiet/sivilingeniørstudiet ved NTNU” § 20, the Department of Energy and Process Engineering reserves all rights to use the results and data for lectures, research and future publications.

Submission deadline: 10. Juni 2020.

- Work to be done in the Waterpower laboratory
 Field work

Department for Energy and Process Engineering, *10. January 2020*

Bjørn Winther Solemslie
Supervisor

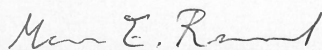
Co-Supervisor(s): Bruno G. Pollet
Ole Gunnar Dahlhaug

Acknowledgement

The work presented in this master thesis has been performed at the Waterpower Laboratory, Department of Energy and Process Engineering at the Norwegian University of Science and Technology.

First, I would like to thank my supervisor Associate Professor Bjørn Winther Solemslie for the guidance during the writing of this thesis. His advice has been a great support and inspiration for me during the past semester. Professor Ole Gunnar Dahlhaug and Professor Bruno G. Pollet are greatly appreciated for always having an open door when new questions arise. A special thanks to Sebastian Franz Stranzl and Ulrich Pulg at NORCE for shearing their experience and ideas and contributing with fruitful discussions and viewpoints to the solutions obtained in this thesis. I would also like to thank Postdoctoral fellow Igor Iliev for detailed and valuable guidance on CFD-calculations in ANSYS CFX when an unexpected lock down changed the scope of my thesis work.

The last year I have been privileged to work at the Waterpower Laboratory. Here, a community of my colleague students and academic staff creates an open, friendly environment for shearing knowledge and experience, making us perform at our best. I am grateful for the opportunity to write my thesis in this unique place.



Maren Elise Rognerud
Trondheim, June 2020

Abstract

In Norway, more than 10 hydropower plants are known to have caused biologically relevant levels of total dissolved gas supersaturation in rivers downstream power plants. This phenomenon is causing gas bubble disease in fish and has large impacts on the biodiversity in the affected water systems. One suggested solution to this problem is employing power ultrasound (20 kHz - 1 MHz) for degassing the supersaturated water prior to releasing it into the lower reservoir.

The degassing effect from ultrasound is dependent on ultrasonic frequency, acoustic amplitude and residence time. Preliminary experiments, carried out at the NTNU Hydrogen Energy and Sonochemistry Laboratory, exploring the behaviour of the degassing process at different ultrasonic frequencies and amplitudes conclude that frequencies of 24 kHz were most effective and the degassing effect increased with increasing acoustic amplitude [1]. Hence, this thesis aims to broaden the understanding of ultrasonic degassing by constructing a test rig for degassing supersaturated, flowing water by employing ultrasound. The test rig is built in the Waterpower Laboratory at the Norwegian University of Science and Technology (NTNU).

The design of the test rig is based on the design of a Francis turbine draft tube to maximize similarity with the final application in a prototype solution. The suggested test rig design is evaluated by performing a CFD-analysis of the flow field in the test rig, and is followed by a discussion of the strengths and weaknesses of the final design configuration.

It is concluded that the suggested setup is fit for conducting well defined experiments on degassing flowing, supersaturated water. The flow pattern through the setup is as expected in the design procedure, but some challenges are detected. Two sharp expansions and an asymmetric inlet section are resulting in an uncertainty of whether experiments with different flow rates are comparable. This uncertainty is eliminated by testing the degassing effect of the setup without ultrasound applied in the system, and evaluate whether different flow rates induce different degassing.

Sammen drag

Gassovermetning i vannkraftverk er en lite kjent, men veldig alvorlig tilstand som har påvirket biologisk mangfold negativt i flere vassdrag i Norge. Det er kjent at 10 kraftverk har hatt redusert biologisk mangfold på grunn av gassovermetning og det er mistanke om at problemet kan være mer omfattende også andre steder. Gassovermetning gir gassblæresyke hos fisk, en dødelig tilstand dersom den varer over lengere tid. En foreslått løsning for å redusere utslipp av overmettet vann er å bruke ultralydbølger til å fjerne oppløst luft fra vannet før det slippes tilbake i vassdraget.

Tidligere arbeid med denne problemstillingen har vist at effektiviteten til avgassingsprosessen er avhengig av ultralydens frekvens, amplitude og vannets oppholdstid i ultralydfeltet. Ultralydfrekvenser i nærheten av 24 kHz var mest effektive og økt akustisk amplitude gir økt avgassingseffektivitet [1]. Denne studien tar sikte på å utvide forståelsen av avgassingsprosessen ved bruk av ultralyd. Dette gjøres ved å designe et forsøksoppsett der avgassing av rennende, overmettet vann kan studeres. Oppsettet bygges i Vannkraftlaboratoriet ved Norges teknisk-naturvitenskapelige universitet (NTNU).

Oppsettets design er basert på designkriterier for sugerøret i Francis-turbiner som en begynnelse på utviklingen av en prototypeløsning. Det foreslåtte designets ytelse kontrolleres ved å gjennomføre en CFD-analyse av strømmingen i oppsettet og følges opp av en diskusjon som avdekker styrker og svakheter ved det presenterte designet.

Det konkluderes med at oppsettet er tilstrekkelig for å gjennomføre veldefinerte eksperimenter med avgassing av rennende, overmettet vann. Strømmingen gjennom oppsettet er som forventet gjennom designprosessen, men noen utfordringer pekes ut. To skarpe kanter ved ekspanderende strømningsareal fører til separasjonspunkter i strømmingen. Ett av to innløpsdesign fører til en usymmetrisk strømming gjennom oppsettet. Det er usikkert hvor mye disse strømningsfenomenene påvirker avgassingsprosessen ved ulike volumstrømmer. Usikkerhet om forsøk med forskjellig volumstrømmer kan sammenlignes kan elimineres ved å teste avgassing i oppsettet for ulike volumstrømmer uten ultralyd og deretter vurdere om en sammenligning kan forsvares.

Table of Contents

Acknowledgement	i
Abstract	ii
Sammendrag	iii
Nomenclature	ix
1 Introduction	1
1.1 Background	1
1.2 Previous work	2
1.3 Objective	4
2 Theory	5
2.1 Hydropower plants and Francis turbines	5
2.1.1 Hydropower plants	5
2.1.2 Francis turbines	7
2.2 Total dissolved gas supersaturation in hydropower plants	12
2.2.1 Dissolved air in water	13
2.2.2 Measurements of total dissolved gas supersaturation in water. . .	14
2.3 Ultrasound utilized for degassing air from water	15
2.3.1 Ultrasound	15
2.3.2 Acoustic cavitation	16

2.3.3	Other phenomena introduced by ultrasound	17
2.3.4	Degassing with ultrasound	18
2.3.5	Acoustic cavitation in flowing water	18
2.3.6	Ultrasonic transducers and probes	21
2.4	Fluid flow	21
2.4.1	Pipe flow	22
2.4.2	Minor losses and characteristics of different flow geometries	24
2.4.3	Open channel flow	27
2.4.4	Errors in experimental data	29
2.5	Computational fluid dynamics (CFD)	30
2.5.1	Discretization	30
2.5.2	Mesh	31
2.5.3	Governing equations	32
2.5.4	Reynolds averaged Navier-Stokes equations (RANS)	33
2.5.5	Turbulence models	34
3	Methodology for the experiment design development	37
3.1	Developing an experiment setup design	37
3.1.1	Initial design proposal	38
3.1.2	Second iteration design proposal	39
3.1.3	Final design configuration	41
3.2	Dimensioning the experiment setup	42
3.2.1	Diffuser dimensions	42
3.2.2	Bend design	44
3.2.3	Flume design	45
3.2.4	V-shaped weir plate design	45
3.3	Producing supersaturated water with air	46
3.4	Flow rate regulation	47
3.5	Obtaining a constant water level in the pressure tank	50
3.6	Ultrasound design	51
3.7	Measurement equipment	52
3.8	Suggested experiment procedure	53

4	Numerical methodology and setup	55
4.1	Geometry	55
4.2	Mesh	56
4.3	Solver settings	61
5	Results and discussion	63
5.1	Numerical results	63
5.2	Flow field evaluation	67
5.3	Ultrasound and the degassing effect	69
6	Conclusion	71
7	Further work	73
	Bibliography	75
	Appendix	79

Nomenclature

Symbol	Description	Unit
a	Speed of sound	[m/s]
B	Width of approach channel	[m]
c_1	Water velocity at runner inlet	[m/s]
$c_{\theta 1}$	Tangential component of water velocity at runner inlet	[m/s]
c_2	Water velocity at runner outlet	[m/s]
$c_{\theta 2}$	Tangential component of water velocity at runner outlet	[m/s]
c_3	Water velocity at outlet to lower reservoir	[m/s]
C_d	Coefficient of discharge	[–]
C_g	Gas concentration at equilibrium	[mg/L]
D	Pipe diameter	[m]
D_h	Hydraulic diameter	[m]
D_{t2}	Turbine outlet diameter	[m]
f	Darcy friction factor	[–]
f_0	Piezoelectric material resonance frequency	[Hz]
f_u	Acoustic frequency	[Hz]
Fr	Froude number	[–]
g	Gravitational constant	[m/s ²]
h	Upstream gauged head above crest level	[m]
h_b	Ambient pressure	[m]
h_e	Effective head in flow calculations with weir	[m]
h_f	Head loss due to friction	[m]
h_{ML}	Head loss due to minor losses	[m]
h_{va}	Water vapour pressure	[m]
h_2	Static pressure in position 2, Figure 2.5	[m]
h_3	Static pressure in position 3, Figure 2.5	[m]
H_G	Gross head	[m]
H_g	Gas solubility constant from Henry's Law	[mg/L · atm]
H_{net}	Net head, head driving the turbine	[m]
ΔH_{loss}	Head loss in hydropower tunnel system	[m]
H_s	Suction head for turbine, always smaller than zero	[m]
I	Acoustic intensity	[W/m ²]
k	Turbulent kinetic energy	[m ² /s ²]
k_h	Surface tension and viscosity compensation factor	[m]
K_b	Hydraulic loss coefficient for pipe bend	[–]
K_{SE}	Hydraulic loss coefficient for sudden expansion	[–]
K_{SC}	Hydraulic loss coefficient for sudden contraction	[–]
K_{DIFF}	Hydraulic loss coefficient for expanding diffuser	[–]
L	Pipe length	[m]
L_c	Characteristic length, i.e. flow depth for wide channels	[m]
$L_{h,t}$	Entrance length for turbulent pipe flow	[m]
\dot{m}	Mass flow rate	[kg/s]
M	Molar mass	[kg/kmol]
N_{ED}	Dimensionless turbine rotational speed	[–]

Symbol	Description	Unit
p	Height of crest relative to the floor	[m]
$p(R)$	Pressure in the liquid at the bubble boundary	[Pa]
p_{gE}	Pressure in the gas at the bubble boundary at equilibrium	[Pa]
$p_{\infty}(t)$	Pressure in the liquid at a large distance from the bubble	[Pa]
p_i	Pressure in the gas at bubble wall	[Pa]
ΔP	Static pressure difference over turbine	[Pa]
P	Static pressure	[Pa]
P_a	Maximum pressure amplitude in acoustic wave	[atm]
P_g	Partial pressure of a gas	[atm]
P_u	Pressure amplitude in acoustic wave	[atm]
P_{∞}	Ambient pressure	[Pa]
Q	Flow rate	[m ³ /s]
Q_{ED}	Dimensionless turbine flow rate	[-]
$R(t)$	Gas bubble radius	[m]
R_E	Gas bubble radius at equilibrium	[m]
Re	Reynolds number	[-]
Re_o	Reynolds number in open channel flow	[-]
R_h	Hydraulic radius	[m]
R_0	Gas constant	[J/Kmol · K]
t	Time	[s]
T	Temperature	[K]
u^*	Friction velocity	[m/s]
u^+	Normalized velocity in turbulent boundary layer	[m/s]
$u(y)$	Local velocity at point y	[m/s]
u_1	Runner rotational velocity at runner inlet	[m/s]
u_2	Runner rotational velocity at runner outlet	[m/s]
U	Free stream velocity	[m/s]
v_1	Relative water velocity at runner inlet	[m/s]
v_2	Relative water velocity at runner outlet	[m/s]
V	Mean water velocity	[m/s]
ΔW	Specific work	[m ² /s ²]
y^+	Normalized distance from wall in turbulent boundary layer	[-]
z	Elevation above reference line	[m]
z_1	Elevation above reference line at turbine inlet	[m]
z_2	Elevation above reference line at turbine outlet	[m]
z_3	Elevation above reference line at outlet to lower reservoir	[m]

Greek letters

Symbol	Description	Unit
α	V-shaped weir notch angle	[deg]
β	Diffuser angle	[deg]
δ	Boundary layer thickness	[m]
η	Turbine hydraulic efficiency	[-]
κ	Polytropic exponent	[-]
ρ	Density	[kg/m ³]
σ	Bubble surface tension	[N/m]
τ	Turbine shaft torque	[Nm]
τ_w	Wall shear stress	[kg/m]
μ	Dynamic viscosity	[kg/m · s]
ν	Kinematic viscosity	[m ² /s]
ω	Turbine rotational frequency	[s ⁻¹]
ξ	Friction loss coefficient	[-]

Introduction

1.1 Background

Hydropower is the most important source for energy production in Norway. 94 % of the total electricity production is generated with hydropower and by the beginning of 2019 the average production was 134,9 TWh per year from the 1626 power plants in operation [2]. Technological development in hydropower has enabled power demanding industry and power system technology to evolve throughout the last 100 years [3]. During this century, knowledge about hydropower systems has grown, and researcher's attention has been directed towards new challenges like preservation of environmental values and biodiversity.

One of the more recent challenges is the issue of gas supersaturation in rivers and lakes downstream hydropower plants. This phenomenon was first observed downstream river power plants in the Colombia and Snake rivers in the 1960s [4]. In Norway suspicion that supersaturated water from power plants could cause fish kills were raised in 1972 when dead fish were observed downstream Matre power plant in Masfjorden [5].

Gas supersaturation occurs if the amount of dissolved air in water is higher than the solubility threshold at a given ambient pressure and temperature. Supersaturated water can occur in hydropower plants when pressurized water with high concentration of dissolved air is exposed to atmospheric pressure in the downstream river or lake. When this phenomenon occurs, fish and other aquatic species die from gas bubble disease if the supersaturation levels are high over a longer period of time [5, 6]. The supersaturated water will naturally degas, but this process is slow, especially in deep and calm rivers or lakes. This results in supersaturated water being transported for tens of kilometres downstream the power plant and affecting biodiversity in vast areas of the water system [5].

The mechanism of degassing begins with precipitation of small bubbles in the water and molecules of dissolved gases start to dissipate into the bubbles. When a bubble becomes sufficiently large it floats to the surface and removes the excess gas.

This master thesis is exploring one potential solution to the challenge of minimizing the discharge of supersaturated water from hydropower plants, by using ultrasound to promote the degassing. Utilizing ultrasound for degassing has been widely used in the food industry to improve quality and durability of food products, and in material technology to ensure better quality of metal, glass and other products [7]. If ultrasound is applied on supersaturated water, the rarefaction induces cavitation bubbles that can contribute to accelerate the degassing mechanism [7].

1.2 Previous work

In preparation for the master thesis, a project thesis was performed during the autumn 2019. The objective was finding the most effective ultrasonic power level and frequency for degassing dissolved oxygen from water [1].

A literature study was performed to gain knowledge on the degassing mechanism in water and a summary of the study is found in the theory section of this thesis. Additionally, small-scale experiments gave an indication of the ultrasound specifications to use in order to obtain effective degassing.

The experiments were performed in the Hydrogen Energy and Sonochemistry Laboratory at NTNU on 1.2 litres of water saturated with oxygen. The level of dissolved oxygen was logged while different frequencies of ultrasound were applied to the supersaturated water. When the most effective frequency was found, similar experiments were done with different power amplitudes for one fixed frequency.

The main findings of these experiments were that the degassing effect is dependent on both acoustic amplitude and frequency. Various phenomenon introduced by acoustic cavitation results in a high degassing effect for low frequencies around 24 kHz and higher frequencies around 860 kHz with a less effective region between them. The increase in power results in a higher degassing efficiency, and the power must be increased to maintain the degassing efficiency when the sonicated water volume is increased. The fastest completed degassing of 1200 mL water from 230 % saturation with a frequency of 24 kHz and a transmitted acoustic power of 134 W was measured to take about 20 minutes. These results are presented in Figure 1.1.

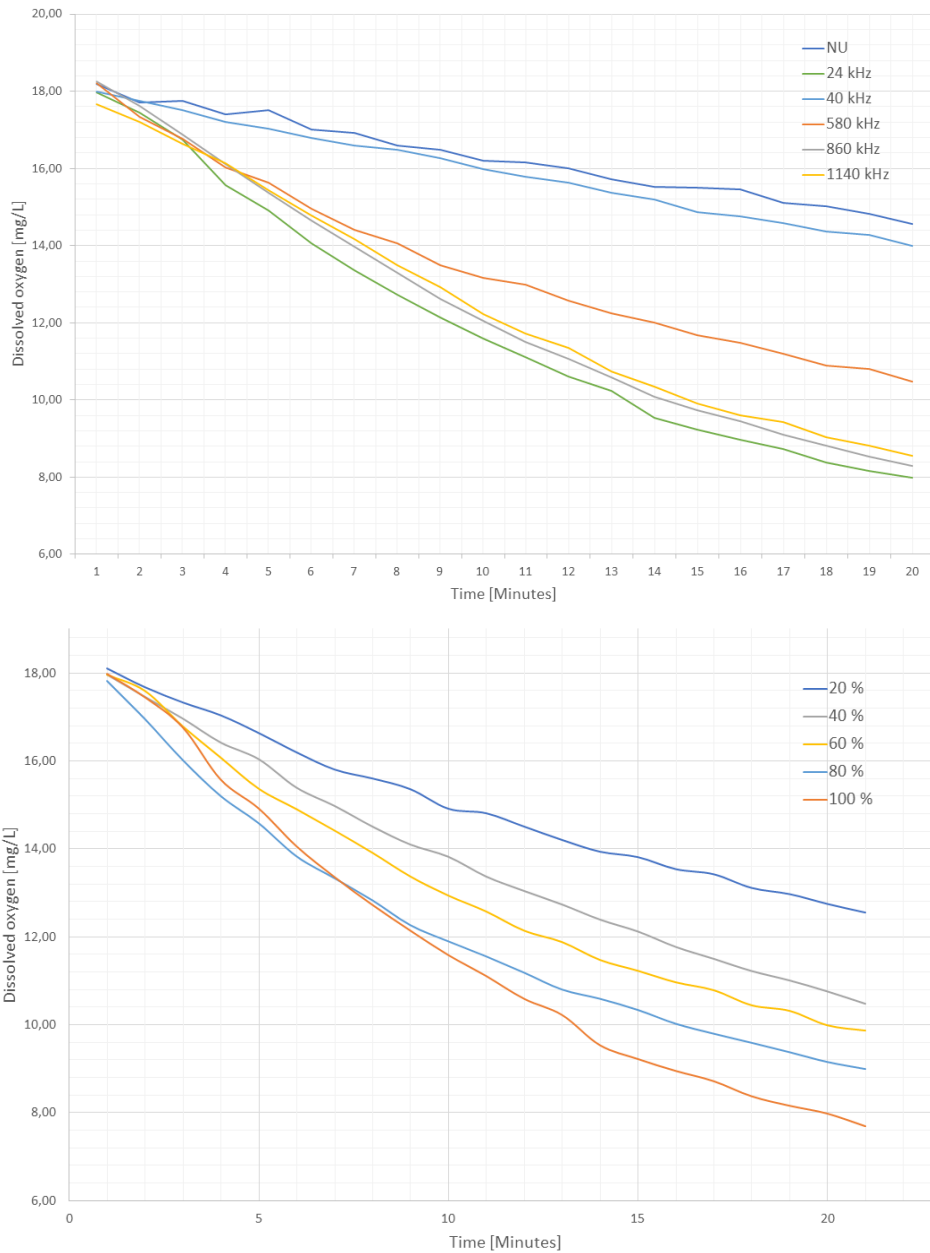


Figure 1.1: The top graph: Level of measured dissolved oxygen over time for ultrasonic the frequencies 24 kHz, 40 kHz, 580 kHz, 860 kHz, 1140 kHz and no ultrasound (NU). The lower graph: Level of measured dissolved oxygen over time for ultrasonic frequency of 24 kHz and amplitudes of 20 %, 40 %, 60 %, 80 % and 100 %.

1.3 Objective

The final goal in this project is investigating the possibility of whether degassing water from hydropower plants by utilizing ultrasound is a possible and practical solution. The process of evaluating the practical implementation of an ultrasonic degassing solution in commercial hydropower plants is initiated by developing an experimental setup in small scale.

From results obtained in the previous work, the challenge of degassing large amounts of water has been illustrated. Investigating the degassing effect on supersaturated water moving through an ultrasonic field, with a shorter time of exposure to the ultrasonic waves, is of interest. Therefore, the main objective of this thesis will be to develop an experiment test rig for experiments on reducing the air content in supersaturated, flowing water by employing ultrasound in the Waterpower Laboratory at NTNU.

The work will include designing the experimental rig with an effective hydraulic design, develop a procedure for producing supersaturated water with air, specifying a system for taking accurate measurements and validating the setup geometry by performing CFD-calculations on the flow field to ensure a good hydraulic design.

Additionally, a literature study will be performed to build basic knowledge on hydropower plants and Francis turbines, the theory of fluid flows in open channels and pipes, ultrasound and acoustic cavitation in water, the degassing mechanism and the behaviour of dissolved air in water, and finally a theoretical background for CFD-calculations.

Chapter 2

Theory

This section introduces background knowledge to build an understanding of the challenge of total dissolved gas supersaturation in hydropower plants and the possible solution of ultrasonic degassing. The chapter opens with an introduction to the physical structure of hydropower plants and how Francis turbines are parts of these power systems. Furthermore, a description of how total dissolved gas supersaturation occurs in hydropower plants, how it behaves and how the dissolved gas can be measured is given. Thereafter, ultrasound is introduced and the degassing mechanism is described. Different flow regimes, measurement methods and experimental error handling is introduced to underpin the design process and the experimental setup. Finally, an introduction to CFD-analysis is presented to build background knowledge on the use of this analysis method.

The following sub-subsections are partly reproduced and modified from the author's project thesis [1]: 2.2.0, 2.2.1, 2.3.1, 2.3.2, 2.3.3, 2.3.4 and 2.3.6.

2.1 Hydropower plants and Francis turbines

Total dissolved gas supersaturation can occur in hydropower plants if the conditions are right. Some parts of the hydropower system are better suited for the degassing process than others. This section aims to introduce a typical Norwegian hydropower system with Francis turbines to explain how the problem can occur, and where it should be solved.

2.1.1 Hydropower plants

The typical Norwegian hydropower plant is a high head power plant with storage magazines at high altitude, equipped with Francis turbines. The water is often taken from multiple intakes both from larger magazines, but also from smaller intakes where water

resources from creeks are utilized [8]. A typical example is illustrated in Figure 2.1. Surge shafts are installed to dampen out flow surges during turbine regulation, and the turbine is driven by the net head, H_{net} ; the total difference in height between the lower reservoir surface and the upper reservoir surface, H_G , minus the hydraulic losses in the tunnel system, ΔH_{loss} .

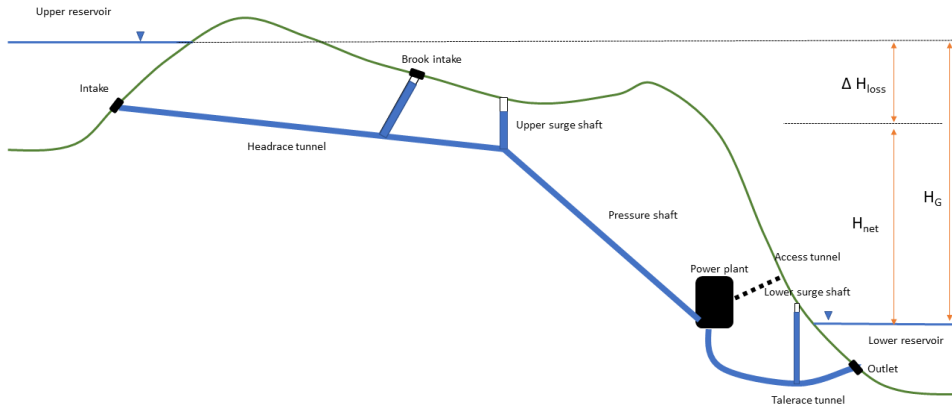


Figure 2.1: A typical Norwegian hydropower system (not drawn in scale).

The Bernoulli equation, Equation 2.1, states that *“the sum of kinetic, potential and flow energies of a fluid particle is constant along a streamline during steady flow when compressibility and frictional losses are negligible”* [9].

$$P + \frac{\rho V^2}{2} + \rho g z = \text{constant} \quad (2.1)$$

Each term in the Bernoulli equation represents a pressure. P is the static pressure and represents the actual thermodynamic pressure in the fluid. $\rho V^2/2$ is the dynamic pressure and represents the pressure energy rise in a fluid with velocity V being brought to rest isentropically. Finally, $\rho g h$ is the hydrostatic pressure. This pressure is due to the weight of the water column above the fluid particle [9].

The assumptions made in the Bernoulli equation are not always valid in hydropower systems. The flow is not steady during flow regulation, friction is present in the tunnels and turbine, and the flow cannot be considered incompressible at all times. Additionally, as the Bernoulli equation is an equation assuming that energy is conserved, and is not applicable through the turbine where energy is taken out through shaft torque and heat is escaping from or added to the system due to viscous forces and heat transfer from the bearings. Nevertheless, during normal operational conditions the flow is assumed to be

steady and incompressible, and the friction losses in the system can be modelled with simple relations like the Manning equation or the Darcy-Weisbach equation, Equation 2.2 [8]. The Bernoulli equation is therefore a good tool for understanding the changes in pressure throughout the hydropower system, although smaller changes in energy content are not accounted for.

$$h_f = f \frac{L}{4R_h} \frac{V^2}{2g} \quad (2.2)$$

Here, f is the friction factor determined from a Moody diagram. It is dependent on the surface roughness, the Reynolds number and the duct shape. L and R_h are the tunnel length and the hydraulic radius respectively.

The static pressure in a hydropower system can be visualized by looking at the levels of the water columns in the surge shafts. From Figure 2.1 one can observe the system losses from the upper reservoir to the upper surge shaft as the difference in height of the water levels at the two points in the system. Further, the pressure in the pressure shaft is increasing as the hydrostatic pressure increases closer to the turbine inlet, where the highest pressure in the system is found. In the turbine, pressure energy is converted to rotational kinetic energy and removed from the water system. This results in a low pressure at the outlet of the turbine, creating the pressure difference which is the major driving force of the Francis turbine.

2.1.2 Francis turbines

Hydraulic turbines are utilizing the potential energy of water to produce electricity with an extraordinary efficiency of up to 95 % [10]. Hydropower turbines can be divided into two main types, impulse turbines and reaction turbines. In impulse turbines, e.g. Pelton turbines, all pressure energy is converted into kinetic energy in the inlet nozzle. In reaction turbines only parts of the pressure drop occurs in the inlet section, and the fully submerged turbines utilizes this over-pressure in addition to the velocity of the water to rotate the turbine runner [10]. The most common reaction turbine type is the Francis turbine invented by James Francis in 1848. This turbine type generates about 60 % of the global hydropower based electricity production and is used for a large range of heads, usually below 700 meters [11, 12].

The water approaching from the pressure shaft is evenly distributed to the inlet of the runner by the spiral casing with stay vanes and the adjustable guide vanes. The opening degree of the guide vanes is gradually regulated to control the flow rate through the turbine. The runner blades are not adjustable in Francis turbines, and it therefore has an optimum operational point at fixed speed without swirl at the runner outlet [10]. An illustration of a Francis turbine is given in Figure 2.2. The specific work, ΔW , created over a turbine is given by Euler's turbine equation, Equation 2.3 [10].

$$\Delta W = u_1 c_{\theta 1} - u_2 c_{\theta 2} \quad (2.3)$$

Here $c_{\theta 1}$ and $c_{\theta 2}$ are the components of c_1 and c_2 in the tangential direction on the turbine. This specific work is largest when the swirl component $c_{\theta 2}$ equals zero. Figure 2.3 shows a Francis turbine runner and a schematic of the velocity triangles at the inlet and the outlet of the runner.

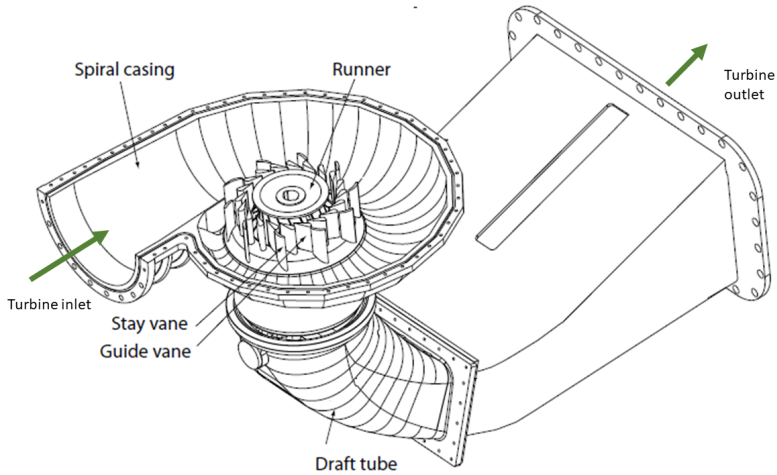


Figure 2.2: Francis turbine. Reproduced and modified from [13]

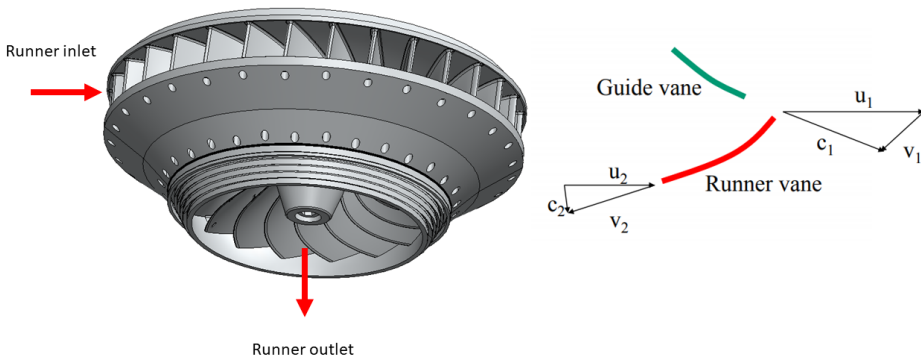


Figure 2.3: To the left: Francis turbine runner. To the right: Schematic of velocity diagrams at inlet and outlet of the runner blade. Here u is the runner rotational velocity, c is the water velocity and v is the relative water velocity, relative to a rotational coordinate system. Subscript 1 is indicating the runner inlet and subscript 2 indicates the runner outlet. Reproduced from [14]

The turbine efficiency is defined by the energy taken out of the flow through shaft torque divided by the available energy in the water as described in Equation 2.4

$$\eta = \frac{\omega\tau}{\rho g H_{net} Q} = \frac{\dot{m}\Delta W}{\rho g H_{net} Q} \quad (2.4)$$

ω is the rotational frequency of the turbine, τ is the shaft torque produced by the turbine, H_{net} is the available head, Q is the flow rate and \dot{m} is the mass flow rate [10]. The head, H_{net} , is defined by Equation 2.5 with ΔP as the pressure difference over the turbine and $z_1 - z_2$ is the difference in elevation between the inlet and outlet of the turbine [15].

$$H_{net} = \frac{\Delta P}{\rho g} + \frac{c_1^2 - c_2^2}{2g} + (z_1 - z_2) \quad (2.5)$$

In order to evaluate the turbine performance and compare different turbines the IEC60193 standard defines the parameters N_{ED} and Q_{ED} as dimensionless numbers representing flow rate and rotational speed of a turbine [15]. These parameters are used together with the efficiency curves which become contour lines like hills are represented on a map to reveal the characteristics of the turbine over the entire operational range. These plots are called hill-charts and are frequently used to present the properties of a Francis turbine. An example of a hill-chart is shown in Figure 2.4

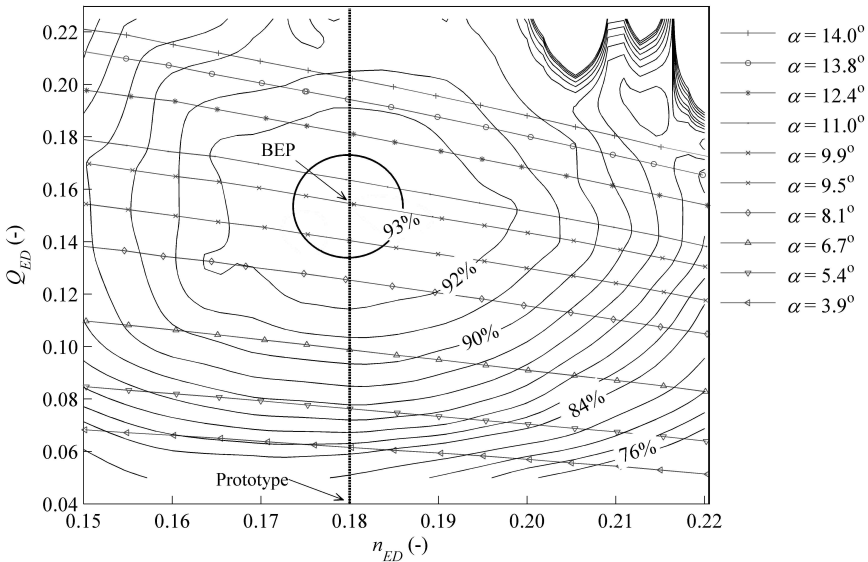


Figure 2.4: Example of a hill-chart. This chart is describing the runner developed in the Francis 99 project [16].

$$N_{ED} = \frac{\omega D_{t2}}{\sqrt{gH_{net}}} \quad (2.6)$$

$$Q_{ED} = \frac{Q}{D_{t2}^2 \sqrt{gH_{net}}} \quad (2.7)$$

where D_{t2} is the outlet diameter of the turbine runner. The same values of N_{ED} and Q_{ED} gives equal velocity diagram shapes for geometrically similar turbines and is therefore a useful tool when evaluating a model turbine's performance prior to building the prototype [17]. The turbine modelled in the hill-chart will have a point where the operational conditions are ideal, and the turbine efficiency is optimized. This is called the best efficiency point, BEP.

Draft tube

At the runner outlet the velocity of the water, c_2 , is small compared to the inlet velocity, but still represents a lost potential for energy production in the system. This results in a lowering of the total efficiency of the turbine compared to an ideal system. To recover this loss, the turbine is equipped with a draft tube with the purpose to convert the kinetic energy at the outlet to pressure energy. Hence, contributing to increase the total pressure difference over the turbine. This is done by increasing the flow area from the outlet for the runner to the outlet of the draft tube. By employing this strategy the pressure at the runner outlet can be below the atmospheric pressure when introducing a draft tube [18].

A common draft tube design, see Figure 2.2, begins as a circular tube with an vertical axis and a small expansion angle. This part is beginning the deceleration of the water. The next section of the draft tube is a bend, leading the water from a vertical to a horizontal flow direction. The bend has a constant cross-section area, but the shape often changes from circular to oval through the bend section. The final part in the draft tube assembly is another expanding section where the cross-section area is increasing and the shape changes from oval to rectangular. This part also has the purpose of decelerating the flow.

One challenging point in draft tube design is avoiding flow separation in the diffuser sections where the flow is decelerating. A decelerating flow is characterized by an adverse pressure gradient. If this negative gradient becomes too strong, the pressure force will push the flow backwards, and separate it from the draft tube walls. To avoid flow separation in diffusers the diffuser angle must be kept sufficiently small, and recommended diffuser angles range from maximum expansion from the centreline of 3° to 6° [19, 20]. The draft tube bend is also exposed to flow separation as the flow accelerates at the bottom of the bend and can cause separation at the sharpest corner of the bend. This phenomenon is avoided by introducing a small expansion from the outlet of the runner to the inlet of the bend to decelerate the flow before this point and continue the expansion after the bend. Some draft tubes are also designed to accelerate the flow through the bend to improve the flow behaviour [18].

When constructing a draft tube many considerations must be made to ensure good solutions, hydraulically, construction wise and economically. Improving the total efficiency of a turbine is a good investment, but also comes at a cost. A good hydraulic design is demanding small expansion angles, long bends and deeply submerged draft tubes. These requirements demand more excavation work, and the construction becomes expensive. Therefore, the draft tube design is often a result of a cost - benefit analysis where a compromise between good hydraulic designs and construction work costs is made [20].

An important consequence of introducing a draft tube is that the pressure at the runner outlet is lowered. This can be seen by applying the Bernoulli equation along a streamline from the outlet of the runner to the outlet of the draft tube and assuming losses in this region are negligible. If the energy is assumed to be conserved in this area, a reduction in flow velocity at the outlet of the draft tube must lead to an increase in pressure at a constant volume flow rate when the continuity equation for an incompressible flow is satisfied. Hence, the pressure at the runner outlet is lowered.

Cavitation

When lowering the pressure at the runner outlet, the risk of cavitation in this area increases. Cavitation is the formation of gas cavities as pressures below the water vapour pressure forces the liquid into gas phase. If the local pressure is below the cavitation threshold pressure, cavitation occurs at the turbine outlet. When this happens it can initially result in an increased turbine efficiency because the wall friction is slightly reduced, but as the cavitation becomes more dominating the larger volume of gas bubbles will displace water, reduce the flow area and decrease the turbine efficiency [18]. Cavitation bubble collapse on a solid surface is eroding the turbine as the bubble collapse creates jets of extreme pressure and temperature on the solid surface.

Figure 2.5 is a schematic view of a Francis turbine system with draft tube and outlet to a lower reservoir. Point 2 in this figure is at the outlet of the turbine and point 3 is at the outlet to the lower reservoir. The energy line is drawn from point 2 to 3 and the loss in this section is $\xi c_2^2/2g$. By applying the Bernoulli equation from point 2 to 3 Equation 2.8 can be deduced, where H_s is the submergence of the turbine below the energy level at the outlet.

$$h_2 + \frac{c_2^2}{2g} = h_b - H_s + \xi \frac{c_2^2}{2g} \quad (2.8)$$

$$-H_s = h_3 + \frac{c_3^2}{2g} + z_3 - z_2 \quad (2.9)$$

To avoid cavitation at the runner outlet the pressure head $h_2 = \xi c_2^2/2g - c_2^2/2g - H_s + h_b$ must be larger than the cavitation threshold pressure, h_{va} . Here h_b is the ambient pressure [12]. As H_s is a negative quantity it is seen from Equation 2.8 that cavitation can be avoided by further submerging the turbine or increasing the friction loss coefficient, ξ , in

the draft tube. Both solutions come with a cost, either for the construction work or the loss of total turbine efficiency.

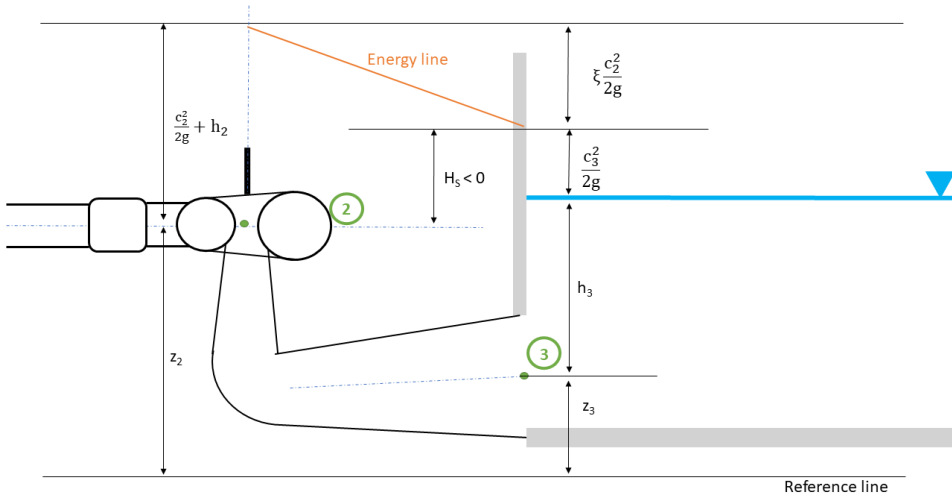


Figure 2.5: Francis system with draft tube and outlet to the lower reservoir. Point 2 represents the outlet of the turbine runner and point 3 represents the outlet to the lower reservoir

2.2 Total dissolved gas supersaturation in hydropower plants

Gas supersaturation can be created by hydropower plants, but is also a natural phenomenon that can occur in rivers. The physical principles allowing for gas supersaturation in rivers are that the solubility of air in water is high for high pressure and low temperature [21]. A high ambient pressure will compress the gas and increase the concentration, and at low temperatures less molecular vibration allows for the concentration of dissolved gasses to increase. Naturally supersaturated water may occur when water is dragged into deep, calm parts of rivers downstream waterfalls where air has been mixed into the water and pressure is higher than the ambient pressure. In deep waters solubility is increasing, causing free bubbles to dissolve in the water. When water containing high concentrations of dissolved air is exposed to the pressure at the surface, it becomes supersaturated because the ambient pressure is lower than the pressure in the depths [5].

This same mechanism can occur in hydropower plants if air is transported through the brook intake, see Figure 2.1. Air is mixed with water going into the pressure shaft, where the pressure is high, and air solubility is much higher compared to the atmospheric pressure. When passing through the turbine, the pressure decreases, and when the water flows into the lower reservoir or river it is exposed to atmospheric pressure. Solubility is here lower and the water becomes supersaturated. The supersaturation often has a longer duration and is more severe when it comes from hydropower plants because difference in

pressure from the pressure shaft to the lower reservoir is much larger than between deep and shallow parts of a river [22]. While natural air supersaturation normally reaches a maximum of 110 % in rivers, supersaturation from hydropower plants can reach levels higher than 200 % [23].

The issue of supersaturated water from hydropower plants is often present in high head power plants with reaction turbines i.e. Francis turbines. When the river downstream the power plant is deep, the degassing process is slow, and the supersaturated water can travel for tens of kilometres downstream. At Brokke power plant in the southern part of Norway the supersaturated water could still be detected 30 km downstream the turbine [22]. Levels of supersaturation that are considered lethal to fish are levels larger than 110 %, but if the supersaturation is lasting for longer periods of time, levels down towards 105 % can be lethal to fish and other aquatic species [5]. Figure 2.6 shows some symptoms of gas bubble disease in fish caused by total dissolved gas supersaturation.

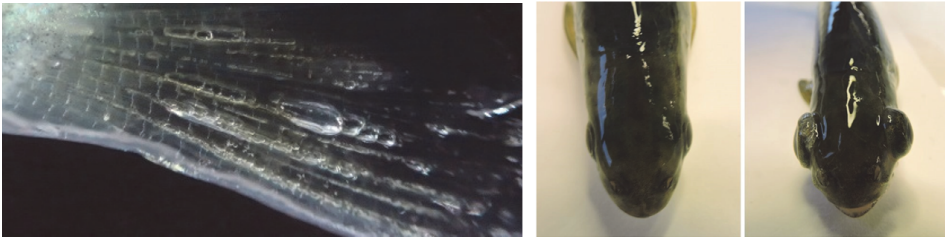


Figure 2.6: To the left: Gas bubbles accumulating in fish fins. Middle picture: fish without gas bubble disease. To the right: Fish with gas bubble disease. All pictures are reprinted from [22]

The source of air entering the waterways of hydropower plants is usually the brook intakes [24]. The intakes are mostly designed to avoid air from entering the system. Although, undersized intakes and flood situations with high water levels causes turbulent flows around the intakes and results in air transportation into the tunnel system. It is important to note that air mixed into the water is very different from dissolved air in water. Mixed in air is small air bubbles distributed in the water that makes it look milky white and can accumulate in the tunnel system. Dissolved air, on the other hand, is not visible in water and gas molecules are blended between the water molecules in a stable equilibrium. Air mixed into the water can cause major problems like blowouts and interruption of the normal flow conditions in the power plant. Dissolved air is not causing blowouts, and is often accepted from a maintenance point of view, but can still be damaging for the biodiversity downstream [8].

2.2.1 Dissolved air in water

Air is a mixture of different gasses including about 20 % oxygen (O_2) and 78 % nitrogen (N_2). Each gas has a partial pressure, and according to Dalton's law of partial pressures, the total pressure is the sum of the different partial pressures of the gasses in the mix, including the water vapour pressure [25]. When air is dissolved in water, the total gas

pressure equals the ambient air pressure. According to the ideal gas law, this partial pressure is increasing proportionally with the concentration of the gas [10].

$$P_g = \frac{\rho}{M} R_0 T \quad (2.10)$$

Here, R_0 is the gas constant, 8314 J/kmolK, and M is the molar mass of the gas in kg/kmol, ρ is the density and P_g and T are pressure and temperature in Pa and K respectively. When the sum of the partial pressures of all dissolved gasses in a liquid equals the ambient pressure, the system is at equilibrium. This amount of gas dissolved in water is the solubility of that gas in water at one specific pressure and temperature. If the system is at equilibrium, no net gas transport occurs between the water and the surrounding air. On the other hand, if water is undersaturated, air from the ambient will be transported into the water. Likewise, if the water is supersaturated, air is transported from the water into the ambient air [5].

The concentration of a gas in a medium (air or water) is proportional to the compression. Henry's law then states that the equilibrium concentration of a gas, C_g , is proportional to the partial pressure of the gas, P_g , with a proportionality constant H_g [5].

$$C_g = P_g H_g \quad (2.11)$$

This proportionality constant, H_g , is dependent on the medium, and in air $H_{O_2} : H_{N_2}$ is approximately equal to 1:4, but in water it is 1:2. From this information it is possible to calculate the total amount of air dissolved in water from only measuring the dissolved oxygen. Although it is a possibility to calculate the concentration of total dissolved gases from only knowing the dissolved oxygen, a more accurate method for obtaining the total dissolved gas level is by measuring the total dissolved gas pressure in the water. The total gas pressure is the important parameter governing the supersaturation level which is causing gas bubble disease in fish [21].

2.2.2 Measurements of total dissolved gas supersaturation in water.

Obtaining accurate measurements of the dissolved oxygen in water is done with dissolved oxygen probes which can give accurate results with a short response time. The above theory may be used to calculate the total gas pressure if the ratio between the different dissolved gasses is known. Although, this calculation requires the river to be in an equilibrium state, which is rarely the case in real rivers. If the aim is to measure the supersaturation level in a rapidly changing system, using the dissolved oxygen is not sufficiently accurate. The problem with supersaturation in rivers comes from the precipitation of bubbles when the total gas pressure in the water is too high. Therefore, measuring the total gas pressure in the water is the best way to monitor the supersaturation level [21].

The measurement technique used to measure the total dissolved gas supersaturation in water is based on comparing the gas pressure to the ambient barometric pressure. The difference between these two values is called ΔP_g . For a positive ΔP_g the water is supersaturated, while for a negative ΔP_g it is undersaturated and lastly, when ΔP_g is zero the system is at equilibrium. The most common method for measuring ΔP_g is using Weiss

saturometers, which utilizes the membrane diffusion method. These instruments consists of a gas permeable silicone rubber tubing connected to a transducer. All the dissolved gasses in the water, including water vapour can diffuse through the membrane and the pressure sensor measures the total gas pressure [21].

Although this measurement technique is practical in use, the membrane diffusion method has multiple sources of error and operational problems. The largest drawback with the method is caused by the large amount of time needed for the pressure within the membrane to reach an equilibrium with the actual gas pressure in the water. Therefore, all measurement readings before this equilibrium occurs will give erroneous results. Secondly, in supersaturated water bubbles are forming, which will disturb the measurement if they adhere to the membrane. This can be avoided by conducting the measurement at deep water or ensuring a flow of water over the probe to remove the bubbles. Thirdly, leakages or tares in the membrane are hard to detect and is an important source of error in the measurements.

2.3 Ultrasound utilized for degassing air from water

This section presents an introduction to ultrasound, the working principles and which phenomena may appear when exposing supersaturated water to an ultrasonic field. In addition to a brief explanation, how ultrasound can enhance the degassing process and the behaviour of ultrasound in flowing water is described.

2.3.1 Ultrasound

Ultrasound is acoustic waves with frequencies above the human hearing range i.e. above 10 - 20 kHz and is commonly classified based on frequency and power [26]. Ultrasound with frequencies above 1 MHz is classified as low power ultrasound transmitting low levels of power with high frequencies. This type of ultrasound usually has an acoustic power of less than 10 W and the medium of propagation remains unaffected by the field. Therefore, it can be used for medical imaging and diagnostics [27]. Ultrasound with low frequencies, i.e. between 20 kHz and 1 MHz, is classified as power ultrasound. These acoustic waves are transferred through a medium with power larger than 10 W, and the acoustic waves are altering the medium of propagation. This range of ultrasonic frequencies is used in sonochemistry where acoustic waves are introduced to produce chemical reactions in the medium of propagation, for instance to produce hydrogen from water [28].

An acoustic wave can be described mathematically with Equation 2.12.

$$P_u = P_a \sin(2\pi f_u t) \quad (2.12)$$

P_a is the maximum pressure amplitude, f_u is the frequency and t is time [29]. The maximum pressure amplitude is directly proportional to the input power from the transducer.

One important measure used for ultrasound is the ultrasonic intensity, I , defined as follows.

$$I = \frac{P_a^2}{2\rho a} \quad (2.13)$$

Here, ρ is the density and a is the speed of sound in the medium. The intensity is defined as the average rate of flow of energy through a unit area normal to the direction of propagation [26].

2.3.2 Acoustic cavitation

Ultrasonic waves are pressure pulsations moving through a medium as illustrated in Figure 2.7. If the rarefaction pressure is below the vapour pressure for water, small bubbles of water vapor starts to form in the liquid. The rarefaction is followed by a compression phase where the pressure no longer can sustain the water vapour, resulting in a violent collapse of the bubble. This collapse launch shock waves into the water that can increase temperatures to about 5000 °C and pressure to 2000 atm at this point [28]. The bubble implosion can induce light emission (sonoluminescence) and chemical reactions where highly reactive radicals are produced (sonochemistry) [30]. If the bubble collapse happens close to a solid wall, the bubble implodes in an asymmetric manner and creates a jet with speeds up to 200 m/s directed towards the solid surface [28]. The forces induced by the collapse have erosive effects on the wall [26]. The process of bubble formation, growth and collapse due to changes in acoustic pressure is called acoustic cavitation. Acoustic cavitation is comparable to boiling, with two major differences. Firstly, boiling is a result of increased temperature in a liquid, not a pressure decrease. Secondly, in boiling the bubble collapse is not present [26].

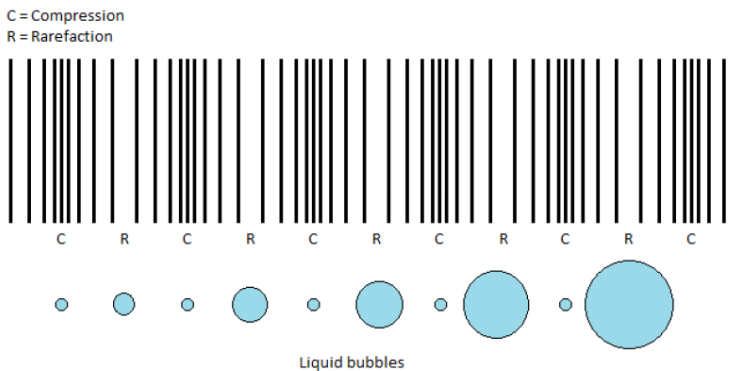


Figure 2.7: Ultrasonic pressure wave propagation and growth of a cavitation bubble during some cycles of ultrasound [31].

2.3.3 Other phenomena introduced by ultrasound

In an ideal system with a fluid exposed to an ultrasonic wave, one parcel of fluid is moving back and forth to the same place with the ultrasonic pressure pulsation. However, in a real fluid the parcel will not move in this manner, and the position will change over time. This phenomenon is called acoustic streaming and results in a direct current flow in the wave propagation direction. This motion can be explained by the fact that the pushing of a viscous fluid along the direction of the acoustic wave is stronger than the pulling of it due to the moment of inertia of the fluid. This creates motion in the liquid. Acoustic micro-streaming is a phenomenon that occurs when the length scale of streaming caused by viscous stress near an object or wall is smaller than the acoustic wavelength [26].

Brotchie, Grieser and Ashokkumar studied the effect of ultrasonic frequency and power on the bubble size of cavitation bubbles [32]. When investigating bubble size for frequencies from 20 kHz to 1136 kHz it was shown that the bubble size decreased considerably with increasing frequency and increased with increasing power. Also, the study concluded that the difference in bubble size was larger for lower frequencies, i.e. higher power. To understand this phenomenon one can look at the mechanism of bubble collapse in an ultrasonic field. When a cavitation bubble is created it is vibrating with a natural frequency much higher than the ultrasonic frequency. The bubble starts growing and when the surface area becomes larger, the natural vibration frequency decreases. This process will continue until the oscillation frequency of the bubble equals the frequency of the ultrasonic field which will cause the bubble to collapse [30]. At high frequencies, the maximum bubble size is limited to a smaller size compared to lower frequencies.

Kasaai investigated the effect of ultrasonic power on the propagation medium [29]. It was found that low frequencies produce high temperatures due to energy dissipation from high power ultrasound, cavitation and micro-streaming. For higher frequencies cavitation becomes less violent, and for frequencies in the MHz - range, only acoustic streaming is observed. The study concluded that the mode of action of ultrasonic waves changes as a function of input power. At low input powers no chemical or physical changes are detected, while at high power the medium changes chemically or physically. Additionally, Ashokkumar points out that bubble collapse is an almost adiabatic process where all energy is converted into heat [33]. For low frequencies, the bubbles are larger and the energy discharge from the bubble collapse is stronger compared to smaller bubbles.

When a bubble collapses, it produces highly reactive radicals due to the high temperature and pressure. Additionally, fewer cavitation bubbles are introduced at low frequencies compared to higher frequencies. All together this means that the radical production, which is attractive to achieve for sonochemistry applications, will have a maximum when both bubble size and bubble numbers are large. For creating shear stress and movement in the solution on the other hand, frequencies lower than this are effective [33].

The cavitation threshold in water, the pressure limit where cavitation is initiated, is calculated by the pressure that is needed to overcome the tensile strength of pure water. Theoretically this limit is at about 1000 atm. Although, experiments show that the actual cavitation threshold is much lower than this limit. The reason for this phenomenon is that the cavity is more easily able to form around micro particles or bubbles that are already

present in the water, so-called cavitation nuclei. In water small bubbles will always be present and the amount of bubbles will increase with the amount of dissolved air in the water [33]. Yasui presents experimental results showing a decrease in cavitation threshold with increased dissolved air [26]. This can be seen as evidence that the cavitation bubbles also contain air, not only water vapor. Therefore, cavitation bubbles can theoretically enhance the degassing process.

2.3.4 Degassing with ultrasound

Ultrasound can have many effects on the medium of propagation. During the rarefaction phase acoustic cavitation occur if the rarefaction pressure is below the cavitation threshold pressure. When cavitation bubbles starts to form, they are pulsating and dissolved air is transported into the bubbles with diffusion [34]. When the pressure is high the bubble decrease in size and the gas diffuses from the bubble into the liquid. When the pressure decreases, the bubbles expand, and gas diffuses from the liquid into the bubble. During the rarefaction the surface area is larger, and more gas can diffuse in through the bubble surface compared to the amount that escapes during the compression phase. This phenomenon is called the area effect on gas diffusion. Additionally, there is a resistance for molecules to move from a low density environment inside the bubble to a high density environment in the liquid phase of water. This effect is called the shell effect. Both the area effect and the shell effect prevent air from leaving the bubble [33]. Hence, the bubble acts like a pump; for each expansion the bubble gain more gas than it loses during the compression and is gradually filled with air. The bubble grows until buoyancy forces become sufficiently strong and drives it to the surface. This process is called rectified diffusion [33].

Microscopic acoustic streams are generated in the viscous boundary layers around the bubble surface and contribute to mass transfer that supplies the bubble with new liquid. When the bubbles starts moving it creates convective flows that contribute to increase the degassing efficiency as the bubbles are distributed around in the liquid [7]. The growth of a cavitation bubble during some cycles of ultrasound is described in Figure 2.7.

Temperature affects the degassing through gas solubility, diffusivity and viscosity of the liquid. The viscosity and gas solubility decreases with higher temperatures and diffusivity increases. Therefore, efficiency of degassing increases with temperature [7].

Additionally, the treatment time and volume are affecting the degassing. The degassing is most effective in the beginning of the process when there is a lot of gas available to diffuse into the bubbles, but over time the efficiency goes down. Larger volumes of liquid require more time to be degassed properly. This phenomenon can also be observed from the results obtained in Figure 1.1. However, stirring to make movement in the liquid or introducing turbulence improves the degassing [7].

2.3.5 Acoustic cavitation in flowing water

The acoustic cavitation appearing in a flow constitutes a complex system which is challenging to model. This two-phase flow is affected by the forces applied by the ultrasound,

the streaming effect and the induced bubble vibrations, but also by the forces working in the flow, like pressure, viscous forces, buoyancy forces and gravity. If the cavitation appears as clouds with little space between the bubbles, one cavitation bubble can affect the bubbles around it. This phenomenon is caused by so-called Bjerknes forces where two bubbles oscillating in an acoustic field can attract or repel each other depending on whether they are oscillating in or out of phase [35]. This subsection aims to give a brief introduction into the modelling of cavitation bubbles in water to illustrate the complexity of these systems and give a brief understanding of the modelling concepts used in previous work within the field.

When modelling the growth of a single cavitation bubble the Rayleigh–Plesset equation is the most used modelling equation. The development of this equation begun in 1917 with Rayleigh modelling the collapse of a gas filled cavity in a large mas of liquid with the assumptions of an incompressible liquid, isothermal compression of the gas and neglecting liquid viscosity and bubble surface tension. Additionally he assumed no velocity component except from the radial component generated at the bubble expansion or collapse and constant pressure far away from the bubble [36]. With these assumptions applied to the momentum equation Rayleigh derived Equation 2.14.

$$R\ddot{R} + \frac{3}{2}\dot{R}^2 = \frac{p(R) - p_\infty}{\rho} \quad (2.14)$$

ρ is the liquid density, p_∞ is the constant pressure in the liquid at a large distance from the bubble, $R(t)$ is the bubble radius and $p(R)$ is the pressure in the liquid at the bubble boundary [37]. Dots are indicating differentiation with respect to time, and this results in speed in the radial direction expressed as $dR/dt = \dot{R}$ and acceleration of the bubble boundary expressed as \ddot{R} .

Plesset extended this equation to include a changing pressure in the liquid, $p_\infty(t)$, surface tension and viscosity by modifying the pressure of the liquid at the bubble boundary as follows.

$$p(R) = p_i - \frac{2\sigma}{R} - \frac{4\mu}{R}\dot{R} \quad (2.15)$$

p_i is the pressure in the gas at the bubble wall, σ is the surface tension constant and μ is the dynamic viscosity of the liquid. Inserting this modification into Equation 2.14 the generalized Rayleigh-Plesset equation is obtained [37].

$$R\ddot{R} + \frac{3}{2}\dot{R}^2 = \frac{1}{\rho}(p_i - p_\infty - \frac{2\sigma}{R} - \frac{4\mu}{R}\dot{R}) \quad (2.16)$$

The surface tension and viscous terms in this equation are most significant for small bubble radii [36]

The modelling of gas bubbles in water is depending on the physical condition of the bubbles. In gas bubbles created from heat transfer and boiling, the energy equation is an important part of the modelling as the heat is causing the vapour content in the bubble to be significant and the bubble motion is altered by the heat energy. In a cool liquid, on the other hand, the vapour density is low and the vapour content in the bubble is negligible. In these flows the bubble motion is altered only by the inertia in the water [37].

The dissipation of non-condensable gas into the gas bubbles is not accounted for in the given equation. One suggested solution by Plesset was modelling the gas diffusion with the term $p_{gE}(R_E/R)^{3\kappa}$. p_{gE} is here the gas pressure at the bubble boundary when the bubble is at an equilibrium state defined as the radius $R_E = 2\sigma/(p_i - p_\infty)$. When modelling degassing with ultrasound this is a crucial point to model correctly. This can be modelled by assuming that the gas behaves in a polytropic manner. κ is therefore the polytropic constant, where $\kappa = 1$ represents a isothermal behaviour, while $\kappa = \gamma$ represents an adiabatic behaviour, where γ is the ratio of heat capacities in the gas [36]. This modelling principle is challenging because the polytropic exponent is strongly dependent on the ultrasound frequency [37]. With this modelling the volume of non-condensable gas inside the bubble is assumed to be constant, but the gas content in the bubble can be solved by the gas diffusion equation with the energy equation to model the polytropic exponent [36].

When allowing for a changing ambient pressure with time, $p_\infty(t)$, modelling of bubble formation, growth and collapse can be done with the Rayleigh-Plesset equation [38]. More complex pressure fields like the pressure field generated from an ultrasound source can also be modelled. Plesset suggested doing this by defining the pressure as an harmonic wave like shown in Equation 2.17 [37].

$$p_\infty(t) = P_\infty(1 + P_a \cdot \sin(2\pi f_u t)) \quad (2.17)$$

When the modelling of the bubble creation, pulsation a collapse is decided, other aspects of the flow field must be taken into consideration. Exemplified by Zwart, one approach to cavitation modelling in a flow field includes mass conservation models for both the gas phase and the liquid phase. Also, conservation of momentum for both phases assuming no interphase slip by modifying Navier-Stokes equation is needed. Finally, mass sources are modelled from interphase mass transfer, and at the same time constraining the calculation by allowing both phases to fill the existing volume at all times. For turbulent flows, a turbulence model must also be added to the modelling equations, in this case a modified version of the $k - \epsilon$ model is used. Finally the Rayleigh - Plesset equation is used for the cavitation modelling [39].

The differential equations developed in this analysis are not analytically solvable and must be solved with numerical methods and computational fluid dynamics (CFD). Each problem requires individual modelling techniques, and custom-made equations, often requiring large computational power. However, cavitation modelling is highly useful in multiple applications like turbo machinery cavitation, cavitation in water jets, over hydrofoils or in pumps etc. [39–41].

2.3.6 Ultrasonic transducers and probes

The basic principle used in constructing ultrasonic transducers is the inverse piezoelectric effect. A piezoelectric material is deforming when it is put in an electric field. The material will oscillate at the same frequency as the voltage applied to it. When a material is vibrating in contact with a liquid, it will radiate an ultrasonic wave in the liquid with the same frequency as the applied AC voltage [26]. The piezoelectric material is vibrating most strongly when it is vibrating at its resonance frequency, f_0 , which is dependent on the volume and shape of the material if the density is constant. By varying these parameters one can obtain transducers producing different frequencies. The acoustic pressure amplitude is controlled by the area of the ultrasonic transducer. Equation 2.13 show ultrasonic variations based on pressure amplitude, and for constant power supplied to a transducer the pressure amplitude will increase with decreasing surface area of the transducer [26].

There are mainly two types of experimental setups with ultrasonic transducers. The first is when the transducer is in direct contact with the liquid. For instance, an ultrasonic horn or plate transducer. The other type is ultrasonic bathes where the transducer is connected to the outside of a container and uses a vibration plate to transfer the ultrasonic waves [26]. In this thesis the first mentioned type is of interest.

The basic ultrasound transducer is made by applying an electrical field to a piezoelectric material which is vibrating at a certain frequency and transmits this ultrasonic energy to a load, the material exposed to the ultrasound. When looking at the transducer system as a mechanical oscillator system, a forced vibration of a damped oscillator is often a used modelling case. When a force like this is applied to a cylindrical rod-shaped ultrasound probe, the probe will stretch and contract with the applied frequency enabling the ultrasonic wave to propagate in the longitudinal direction of the probe. Additionally, this stretching and contraction of the rod will induce in an expansion and contraction in the radial direction, resulting in wave propagation in this direction as well. This is called the Poisson effect. Different geometries can therefore be used to direct the vibrations in the desired directions from the rod-shaped probes, for instance ultrasonic horns are designed to concentrate the ultrasonic waves on to a small area [42].

2.4 Fluid flow

In the development process of an experimental setup the aim is to predict the behaviour of the fluid flowing in the pipes and channels. Avoiding unwanted behaviour and minimizing the impact from unexpected phenomenon can be done by performing some relatively basic fluid mechanics calculations. This is done to ensure that the setup created is simulating the intended properties and avoid unnecessary uncertainties in the system. This section is introducing some useful concepts and flow regimes that will be used to determine the experimental setup geometry. Additionally, a measurement method for flow rate is introduced together with a brief theory section on experimental errors in flow measurements.

2.4.1 Pipe flow

Pipe flow is an internal flow where the fluid is flowing in a closed conduit and is fully bounded by solid surfaces [9]. The flow in a pipe can be either laminar, turbulent or in the transition region between the two. The flow condition is determined by the Reynolds number, defined in Equation 2.18 [9].

$$Re = \frac{\text{Inertia forces}}{\text{Viscous forces}} = \frac{\rho V D_h}{\mu} \quad (2.18)$$

For laminar flow, the $Re < 2300$ and for turbulent flow the $Re > 4000$ in circular pipes. The transition region is found between the two [9]. From Equation 2.18 it is found that for laminar flow the viscous forces of the fluid are large compared to the inertia forces, and for turbulent flow the opposite is occurring.

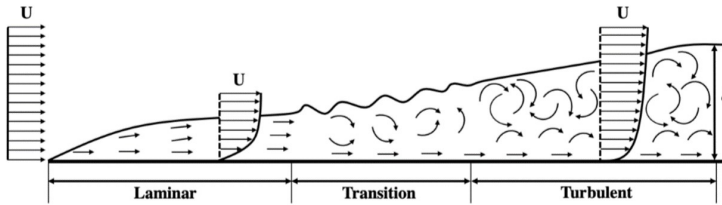


Figure 2.8: Viscous boundary layer over a flat plate. Reprinted from [43]

The velocity profile has different characteristics in laminar and turbulent flow. This can be understood by looking at the boundary layer developing over a flat plate. In the flow over a flat plate, the transition from laminar to turbulent flow can be visualized like illustrated in Figure 2.8.

If the Reynolds number is sufficiently low the flow will remain laminar, but if the Reynolds number increases, the flow will enter the transition region or the turbulent region. Here, the flow is more chaotic and irregular and characterized with small velocity fluctuations in the x , y and z -directions in addition to the mean flow motions. The flow is slowed down and the boundary layer thickness increases. For turbulent flow, the velocity fluctuations contribute to mixing, and results in a flatter velocity profile in the upper part of the boundary layer.

By assuming that the boundary layer development in a pipe is similar to the development over a flat plate, where the plate is curved around the centre of the pipe, the boundary layer thickness will increase until it meets the boundary layer immersing from the opposite wall. This is illustrated in Figure 2.9. When a flow enters the pipe, a boundary layer is developing on the pipe wall. For a viscous fluid the velocity at the wall is zero due to the no slip condition. Initially, the boundary layer is thin, and the velocity gradient, du/dy , is large through the boundary layer, resulting in a large shear stress on the wall, as described by Equation 2.19. This shear stress slows the flow and increases the boundary

layer thickness. This process continues until the boundary layer thickness reaches the centre of the pipe. At this point the flow is fully developed and the velocity profile in the pipe has a constant shape, $u(y)$, beyond this point. The inviscid region in the centre of the pipe is gone, and a fully viscous flow has developed [44]. From this point the pressure drop in the pipe becomes linear both for laminar and turbulent flow and can be described by Equation 2.2.

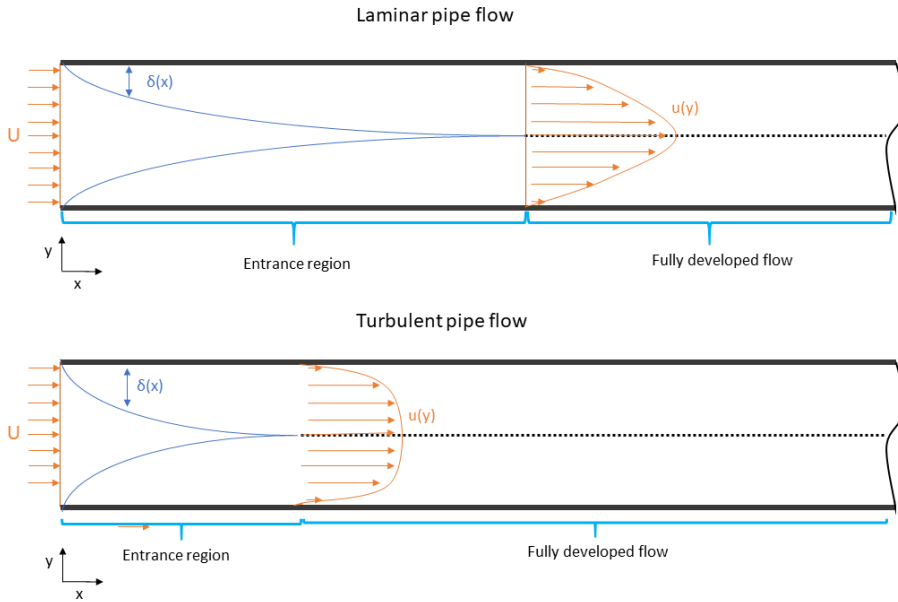


Figure 2.9: Laminar and turbulent boundary layer development in a pipe.

$$\tau_w = \mu \left. \frac{du}{dy} \right|_{y=0} \quad (2.19)$$

The length from the entrance of the pipe to the point where the flow is fully developed is called the entrance length. The entrance length is different for laminar and turbulent flow, and is shorter for turbulent flow due to the mixing caused by turbulent velocity fluctuations as demonstrated in Figure 2.9. The turbulent entrance length, $L_{h,t}$, is defined as follows,

$$L_{h,t} = D \cdot 1.359 \cdot Re^{\frac{1}{4}} \quad (2.20)$$

where D is the pipe diameter, and Re is the Reynolds number. For longer pipes one can also use that the entrance length for turbulent flows is about $10 \cdot D$. In shorter pipes this approximation may underestimate the shear stresses on the pipe wall [9].

2.4.2 Minor losses and characteristics of different flow geometries

The major losses in fluid flow systems are caused by friction losses. Additionally, smaller contributions to the total loss comes from bends, expansions or contractions and diffusers that are introduced in the flow. The main pipe losses introduced in Equation 2.2 will be important, but additional minor losses are added when introducing these parts into the flow. The following subsections will present some important properties of diffusers, bends and sudden expansions or contractions in a pipe system.

Flow through bends

When water is flowing through a bend in a pipe an additional loss is added to the original friction loss in the pipe. In the outer diameter of the bend the flow is accelerated and the speed at this point is larger compared to the flow velocity at the inner diameter of the bend. This creates a positive pressure gradient towards the inner diameter. This, together with the centripetal acceleration from the change of flow direction creates a swirling secondary flow in the bend [44]. This extra loss is depending on the relationship between the pipe diameter, D , and the bend radius, R , as shown in Figure 2.10.

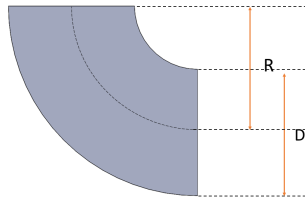


Figure 2.10: Pipe bend

The two factors governing the loss coefficient in the bend is the length of the bend, which gives a larger friction loss when the bend length increases, and the loss created by the secondary flow. This relationship has a minimum loss for one specific R/D - ratio. For circular cross-sections this loss coefficient, K_b , can be found for 90° bends from Equation 2.21, which is a curve-fitting based on experimental results [45].

$$K_b \approx 0.388 \cdot \left[0.95 + 4.42 \left(\frac{R}{D} \right)^{-1.96} \right] \left(\frac{R}{D} \right)^{0.84} Re^{-0.17} = \frac{h_{ML} \cdot 2g}{V^2} \quad (2.21)$$

Additionally it is favourable to maintain a constant or decaying cross-section through the bend to keep the flow attached and less disturbed [18].

Flow through sudden expansions or contractions

In sudden contractions the loss is highly dependent on the sharpness of the edge, while for sudden expansions the loss is less dependent it. The reason for this is the separation occurring at the contraction. This can be minimized by smoothing out the entrance region. In an expansion, the velocity is lost to viscous dissipation regardless of the shape of the expansion. Therefore it is favourable to use smooth contractions, but not important to have smooth expansions. In the sudden expansion the losses from shear stresses in the dead-water regions downstream the expansion can be described by Equation 2.22. Here, V is the velocity in the small pipe.

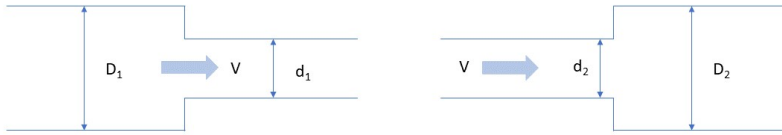


Figure 2.11: To the left: sudden contraction. To the right: sudden expansion.

$$K_{SE} = \left(1 - \frac{d_2^2}{D_2^2}\right)^2 = \frac{h_{ML} \cdot 2g}{V^2} \quad (2.22)$$

This theoretical loss coefficient gives similar results as obtained from experiments [44].

When estimating the loss over a sudden contraction, on the other hand, the separation causes the effective flow area to decrease through the contracting section. Therefore, the estimation of losses in this region are based on experimental data and is given in Equation 2.23.

$$K_{SC} \approx 0.42 \left(1 - \frac{d_1^2}{D_1^2}\right) \quad (2.23)$$

This equation is valid for contractions where $d_1/D_1 < 0.76$. For larger values, the loss is estimated with Equation 2.22 [44].

Flow through expanding diffusers

The losses in an expanding diffuser are balanced between the friction losses in long diffusers with small expansion angles and the losses caused by flow separation when the expansion angle becomes larger.

The loss coefficient through the diffuser can be calculated with Equation 2.24, which is obtained from experiments [44].

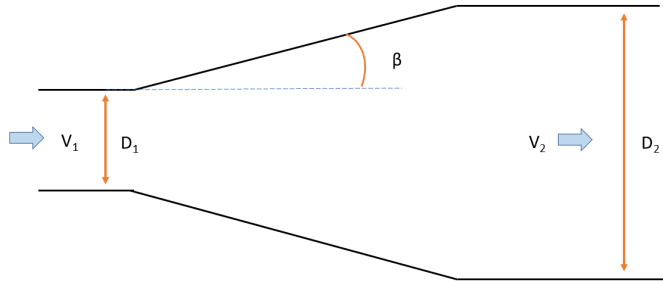


Figure 2.12: Expanding diffuser

$$K_{DIFF} \approx 2.61 \sin(\beta) \left(1 - \frac{D_1^2}{D_2^2}\right)^2 + f_{avg} \frac{L_d}{D_{avg}} \quad (2.24)$$

Here, the diffuser length is L_d , and the averaged diameter and friction coefficients are D_{avg} and f_{avg} respectively. This equation is applicable for diffuser angles, 2β , smaller than 45° . Runstadler has reported data on experiments on flat walled diffusers and found that separation occurs depending on the diffuser angle and the ratio between the inlet height and diffuser length [46]. Data from his findings is listed in Table 2.1.

Diffuser length to diffuser inlet height ratio	Diffuser angle, 2β [deg] separation limit
1	20
2	17
4	12
7	10
10	9
20	6

Table 2.1: The separation limit in flat walled diffusers given by diffuser length to height ratio [46]

To obtain an effective and undisturbed flow through a diffuser it is important to ensure that the flow is attached, and that boundary layer separation is avoided.

2.4.3 Open channel flow

Open channel flow is characterized by a flow of a liquid with a liquid-gas interface, often open to the atmosphere. Flow in channels or partly filled conduits are open channel flows. Unlike pipe flow, the driving force of the flow is gravity only. Along all solid wetted surfaces the no-slip condition is applied, and one example of a typical axial flow velocity profile is given in Figure 2.13.

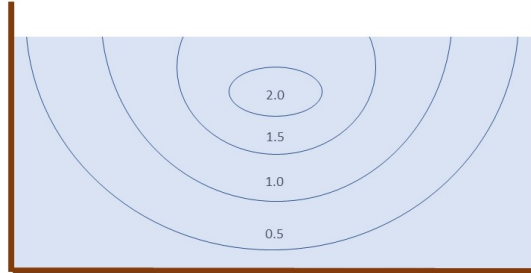


Figure 2.13: Typical constant velocity contours in an open rectangular flume [47].

Open channel flows are classified as steady or unsteady. A steady flow is characterized by a constant flow depth at a certain point in space over time. Like pipe flows the open channel flow can be laminar, turbulent or in the transition region. The Reynolds number in an open channel flow is defined in Equation 2.25, where the hydraulic radius is defined as the flow area divided by the wetted perimeter [9]. The open channel flow is usually laminar for $Re_o < 500$ and turbulent for $Re_o > 2500$.

$$Re_o = \frac{\rho V R_h}{\mu} \quad (2.25)$$

Another classification of open channel flow is subcritical, critical or supercritical flow. This flow condition can be determined by calculating the Froude number given in Equation 2.26.

$$Fr = \frac{\text{Inertia forces}}{\text{Gravity forces}} = \frac{V}{\sqrt{gL_c}} \quad (2.26)$$

For a $Fr < 1$ the flow is subcritical, $Fr = 1$ gives critical flow and $Fr > 1$ gives supercritical flow. This is comparable to the definition of the Mach number describing the relationship between the flow speed and the wave speed in air, with subsonic, sonic and supersonic flow. For open channel flow, the Froude number also describes the quotient of the speed of the water and the wave speed [9].

Flow measurements with V-shaped weirs

Measuring the flow rate in an open flume is an important part of controlling the flow characteristics. Sharp-crested weirs are vertical plates placed perpendicular to the flow in a channel with a rectangular or triangular notch made for the flow to escape through. It can be used for accurate flow measurements in open channels without disturbing the subcritical flow far upstream the weir plate. Closer to the weir the flow becomes critical and eventually supercritical as the water is accelerated closer to the weir crest [9].

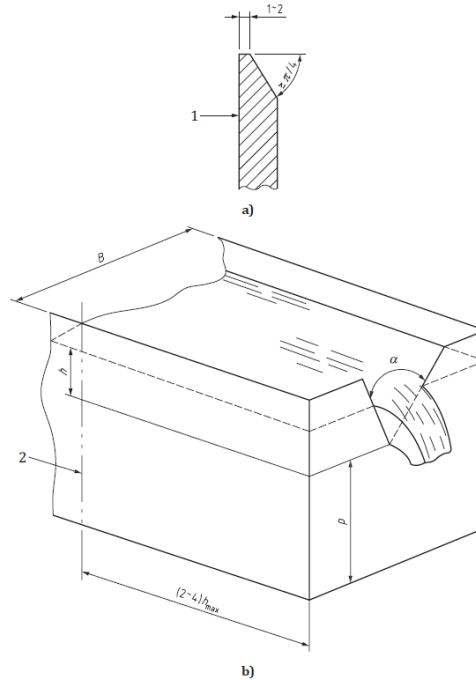


Figure 2.14: Requirements in the design of a V-shaped sharp-crested weir [47]. a) Cut view of the weir plate. The number 1 indicates the upstream phase of the weir plate. Thickness of the sharp edge is 1-2 mm and the angle indicated is minimum $\pi/4$. b) Perspective view of the weir plate with the immersing flow channel. The number 2 indicates the upstream part of the weir and the flow direction.

The requirements for design, installation and calculations of flow with sharp-crested weirs is described by the standard ISO1438 [47]. The notches are rectangular or triangular with free, fully ventilated overfalls to assure atmospheric pressure underneath it. The advantage of the rectangular cross-section of the notch is that the weir is maintaining a relatively large head, h , as seen in Figure 2.14, although the flow rate is small. This is due to the rapid reduction in flow area with decreasing h . This results in an accurate flow measurement for a large variety of flow rates [9].

ISO1438 specifies that the approach channel is defined by a channel of length five times

the nappie width at maximum head upstream the weir [47]. The channel should be straight, and the flow is steady and uniform, similar to the flow shown in Figure 2.13, upstream the influence of the weir. Head measurements are to be performed in the flow upstream the weir to be able to calculate the flow rate. The standard states that the measurement should be made sufficiently far upstream to avoid the region where the head is dropping due to the notch, but at the same time sufficiently close to the weir so the losses in the channel between the measurement point and the weir are negligible. The standard suggests 2 to 4 times h at maximum discharge to be sufficiently far upstream to make the measurement.

The discharge flow is calculated from the measured head value and the following Equation 2.27.

$$Q = C_d \frac{8}{15} \tan\left(\frac{\alpha}{2}\right) \sqrt{2g} h_e^{5/2} \quad (2.27)$$

C_d is the coefficient of discharge and is determined from experiments. This coefficient is given in the standard for a notch angle of $\pi/2$, and is dependent on the ratios h/p , p/B and the notch angle α . The variable h_e is the sum of the measured head, h , and the experimentally determined quantity k_h which compensates for the combined effects of surface tension and viscosity.

2.4.4 Errors in experimental data

When taking a measurement during an experiment, the measurement will never be absolutely correct. The error can come from different sources, like the instrument used in the measurement, an error in the calibration or the value of an assumed known physical quantity like the mass of a weight or the magnitude of the gravitational constant [48].

Errors in experimental data are divided into three different categories. Accidental or intended mistakes is the first category, and is useful to be aware of during experiments, but is not considered in the error analysis. Experiments with this type of errors should be discarded because the error can be avoided in the next experiment. The second category is the systematic errors. Examples of systematic errors are a wrong gradient in a measurement, an incorrect offset, response sensitivity or a non-linearity. The systematic error is often resulting from an inaccurate calibration or an error in the instrument used for the measurement. Thirdly, the random errors make up the final category. These errors are caused by unpredictable, physical noise that alter the measurement and becomes an unavoidable disturbance. When a measurement of the exact same value is to be measured many times, the measurements will spread around an average value creating a probability distribution, usually the normal distribution mathematically known as the Gauss function. The systematic errors are controlled by thorough calibration and by using different measurement equipment and comparing the results, while the random error is minimized by conducting more measurements. By increasing the number of measurements and calculating the mean of the measurements, the random error is minimized [48].

2.5 Computational fluid dynamics (CFD)

Computational fluid dynamics, CFD, is a numerical tool for solving complex and sometimes analytically unsolvable differential equations, often partial differential equations. It includes computer based analysis of systems involving fluid flow and heat transfer and spans a wide variety of topics like aerodynamics, hydrodynamics, combustion, flows inside rotating turbo machinery or chemical reactions [49]. The development of numerical methods and the use of it is highly dependent on the computational capacity of the computers used for the calculations, which has seen a huge development in the few past decades. Problems that would have taken years to solve 50 years ago can now be solved in a few seconds of computer time on a modern computer. Although the development and use of CFD in the industry has grown largely in recent years, some of the ideas and principles behind the numerical calculations and conservation principles originated with Newton, Bernoulli, Euler, Navier and Stokes [50]. As more user friendly numerical solvers are developing it is important to keep in mind that the numerical methods are solving mathematical equations only. The connection from the mathematical equations to correct physical modelling require knowledge and control from the user of the CFD- solver.

In fluid flow problems the mathematical equations to be solved are the Navier-Stokes equations. These equations are describing the the motion of a viscous fluid in a three-dimensional domain in time. The equations can be solved on differential form by using finite differences, or in integral form by using the finite volume method. The software ANSYS CFX uses an element-based finite volume method where the finite volumes are used to conserve quantities like, mass, momentum and energy [51].

In steady state problems the solution will converge towards one solution with one specific velocity and pressure distribution. The solver will get closer to this solution for each iteration, and the convergence of the solution is monitored in ANSYS CFX by calculating the RMS value of the residuals, the root-mean-square of the change in the solution from one iteration to the next. In this thesis residual values of the order $1e-05$ are considered very good results, but results in the order $1e-04$ are also accepted. The discretization error is highly dependent on the number of grid cells in the mesh, and obtaining accurate results hence requires good computational capacity.

2.5.1 Discretization

The Navier-Stokes equations describing a flow field are theoretically describing the flow field in any place in a continuous space where the equation is applicable. To structure the calculation points, the flow domain is divided with a grid to create a finite number of grid cells where calculations are made. The grid cells are control volumes where the conservation equations are applied and this is allowing for a structured calculation for the continuous flow domain by discretizing the domain in space. Hence, discretization is the process of replacing a continuum with a finite number of calculation locations.

The finite volume method is applying conservation principles to control volumes, in this case the grid cells. The conservation equations are applied to a finite volume, fixed in

space, and are often presented on integral form to evaluate the changes inside the control volume by calculating the change over the cell boundaries [50].

When discretizing a domain there will be a discretization error depending on the number of cells that are created. When the number of cells is large the calculation can capture more details compared to fewer cells, but also requires a larger computational capacity to perform the calculations. To make sure that the calculations are accurate and grid independent a mesh dependency study can be performed [49].

2.5.2 Mesh

When solving a numerical problem the main inputs to the computer program are the mathematical equations describing the physical problem, the boundary conditions describing what is entering and leaving the flow domain and the mesh which describes the discretization of the physical domain. A well-constructed mesh is therefore an important part of obtaining good results. Requirements for the mesh is that it should be sufficiently detailed to capture the flow, but not too detailed as this will require an unnecessarily large computational capacity. For instance, boundary layer flows require more cells close to the wall to capture the large velocity gradients in these regions, but less cells in the inviscid flow regime outside the boundary layers [49].

The cell sizes close to a solid wall in a flow domain are often characterized by the dimensionless parameter y^+ . This parameter is originating from turbulent boundary layer theory over flat plates where the turbulent boundary layers are divided into three parts. The inner layer, called the laminar sub-layer where the molecular viscous shear dominates the flow, the log-layer where the turbulent eddy-viscosity is dominating, and finally, the buffer layer between the two where both viscous effects and turbulence are affecting the flow [52]. The three regions are illustrated in Figure 2.15.

The parameters y^+ and u^+ are defined below as functions of u^* . u^* is the friction velocity defined as the square root of the wall shear stress divided by the density, see Equation 2.29, and functions as a scaling parameter for the flow velocity. Here, y is the length scale normal to the wall.

$$y^+ = \frac{yu^*}{\nu} \quad u^+ = \frac{V}{u^*} \quad (2.28)$$

This modelling of the turbulent boundary layer illustrates a linear relationship between the dimensionless parameters u^+ and y^+ , $u^+ = y^+$ in the inner region. In the log-layer a logarithmic relationship is developing, $u^+ = \ln(y^+)/\kappa + A$, where A is a constant. The scaling of the boundary layers by using the u^+ and y^+ parameters enables a generalization of the viscous boundary layers; the shape is constant for comparable viscosity and free stream velocity. This makes y^+ a good parameter for measuring the required cell size close to the wall in any turbulent boundary layer [52].

When choosing a y^+ value for the cell closest to the wall, the aim is to capture the boundary layer sufficiently well. Different methods are used to model the boundary layer in turbulent flows, and these methods will be discussed later in the turbulence modelling sec-

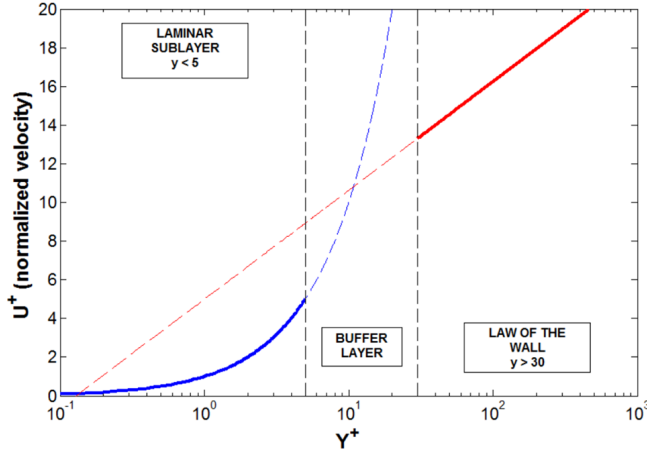


Figure 2.15: Normalized velocity, u^+ , for different normalized distances from the wall, y^+ , in a flat plate turbulent boundary layer. Reprinted from [53].

tion. The calculation of the initial guess of the first cell height, Δs , is based on theory on the turbulent boundary layer over a flat plate, and can be calculated from knowing the y^+ requirement for the applied turbulence model. The calculation for a flat plate is considered a suitable approximation to the boundary layer in any turbulent flow and is given below.

The desired cell height, $y = \Delta s$ is given from equation 2.28 for one specified y^+ value. In order to complete this calculation, the friction velocity must be calculated. As mentioned above this parameter is calculated by Equation 2.29.

$$u^* = \sqrt{\frac{\tau_w}{\rho}} \quad (2.29)$$

For the turbulent boundary layer the wall shear stress can be modelled with Equation 2.30.

$$\tau_w = \frac{c_f \rho V^2}{2} \quad (2.30)$$

where c_f is defined as follows [52].

$$c_f = \frac{0.027}{Re^{1/7}} \quad (2.31)$$

2.5.3 Governing equations

The motion of a viscous fluid is described by conservation equations for mass and momentum, often referred to as the continuity equation and the Navier-Stokes equations respectively. The continuity equation states that the rate of change of mass in a control volume equals the mass transportation over the boundaries of that control volume. For an incompressible fluid the continuity equation is expressed as follows [50].

$$\nabla \cdot \mathbf{V} = 0 \quad (2.32)$$

Here $\mathbf{V} = [u(x, y, z, t), v(x, y, z, t), w(x, y, z, t)]$ and the velocity components u , v and w are the velocities in the x , y and z directions respectively.

The Navier-Stokes equations are expressing Newton's second law of motion on an infinitesimal, fixed control volume. The incompressible Navier-Stokes equation applied on a Newtonian fluid with constant viscosity is expressed in Equation 2.33[50].

$$\rho \frac{D\mathbf{V}}{Dt} = \rho \mathbf{f} - \nabla p + \mu \nabla^2 \mathbf{V} \quad (2.33)$$

The first term on the left-hand side is expressing the convective and local acceleration by the substantial derivative. This term can be simplified for steady state solutions by applying that the change of velocity over time is zero for a steady state solution as shown below.

$$\rho \frac{D\mathbf{V}}{Dt} = \rho \left(\frac{\delta \mathbf{V}}{\delta t} + \mathbf{V} \cdot \nabla \mathbf{V} \right) = \rho \mathbf{V} \cdot \nabla \mathbf{V}$$

On the right-hand side of the Navier-Stokes equation the forces affecting the fluid are expressed. In the first term, $\rho \mathbf{f}$ represents a body force, most commonly represented by gravity. ∇p represents pressure forces on the control volume and finally, $\mu \nabla^2 \mathbf{V}$ represents viscous forces on the fluid element.

Together these expressions constitute four equations, one for mass conservation and three for conservation of momentum in the x , y and z directions. The equations are solved for the four unknown variables, the velocity components in x , y and z directions in addition to the pressure.

2.5.4 Reynolds averaged Navier-Stokes equations (RANS)

The Navier-Stokes equations and the continuity equation presented above are applicable to both laminar and turbulent flows. Although, the random and fluctuating nature of a turbulent flow creates challenges when modelling the velocities and pressures in the turbulent flow regimes. The velocity and pressure values are characterized by small fluctuations in all directions and varying with time from the average value. Additionally the turbulence creates eddies ranging over a large variety of length scales from the Kolmogorov length scales characterizing the smallest turbulent eddies to eddies in the scale of the cross section of the flow passages [52].

To express the velocities and pressures in the incompressible Navier-Stokes equations Reynolds divided the variables into a mean value and a fluctuation like shown in Equation 2.34. The mean is indicated with a bar and the fluctuation with an apostrophe and the mean

value is a time averaged mean of the flow variable. This is called Reynolds decomposition, and allows for a statistical approach to the turbulence closure problem.

$$u = \bar{u} + u' \quad v = \bar{v} + v' \quad w = \bar{w} + w' \quad p = \bar{p} + p' \quad (2.34)$$

By inserting this approximation of the turbulent flow into the Navier- Stokes equations and taking the time average of the equation, the RANS equations are obtained. Equation 2.35 is the continuity equation for the mean flow.

$$\frac{\delta \bar{u}}{\delta x} + \frac{\delta \bar{v}}{\delta y} + \frac{\delta \bar{w}}{\delta z} = 0 \quad (2.35)$$

By subtracting Equation 2.35 from Equation 2.32, the continuity equation for the fluctuations is obtained in Equation 2.36.

$$\frac{\delta u'}{\delta x} + \frac{\delta v'}{\delta y} + \frac{\delta w'}{\delta z} = 0 \quad (2.36)$$

Finally, the averaged momentum equation is expressed as follows.

$$\rho \frac{D\bar{\mathbf{V}}}{Dt} = \rho \mathbf{f} - \nabla \bar{p} + \nabla \cdot \tau_{ij} \quad (2.37)$$

with the stress tensor

$$\tau_{ij} = \mu \left(\frac{\delta u_i}{\delta x_j} + \frac{\delta u_j}{\delta x_i} \right) - \overline{\rho u'_i u'_j}$$

The averaged momentum equation for the mean flow is very similar to the original equation apart from the second term in the stress tensor, modelled as turbulent share stress in this form of the equation. Although this term is not a stress it has been known as the Reynolds stresses due to this organizing of the equation. In turbulence modelling the modelling of this turbulent stress is an important challenge because no certain information about it is obtained from the theory. Only statistical data can be used to create expressions which are modelling the Reynolds stresses sufficiently accurate. To fully define and close the problem of modelling the RANS equations different turbulence models are used to model the Reynolds stresses [52].

2.5.5 Turbulence models

Turbulence modelling is a challenging task for many reasons. Turbulence is a three-dimensional phenomenon which is difficult to predict due to its random nature and large

range of length scales. The Navier-Stokes equations are considered valid modelling equations for both laminar and turbulent flows, but in CFD the large range of length scales makes the direct modelling with the Navier-Stokes equations almost impossible. Being able to directly simulate a turbulent flow, without averaging the Navier-Stokes equations is called direct numerical simulations (DNS). This requires a large number of grid cells and extreme storage capacity on the computers used to solve the problems. This becomes especially apparent in the boundary layers of the flows to be modelled due to the large pressure gradients close to the wall.

This challenge is resolved by modelling the Reynolds stresses in the RANS equations with different turbulence models. The most widely used turbulence models are the two-equation models which are using separate transport equations for velocity and length scales. The most well known examples are the $k-\epsilon$ and the $k-\omega$ models which are using the turbulent kinetic energy and the turbulent dissipation rate to model the turbulence. As the $k-\epsilon$ model is not ideal for boundary layers with an adverse pressure gradient, a mix of the $k-\epsilon$ and the $k-\omega$ models called the SST model is used in this thesis [51].

Share stress transport (SST) turbulence model

The SST turbulence model is giving good results for flow separations in adverse pressure gradient flows. It is a two-equation turbulence model with model equations for the turbulent kinetic energy, k , and the specific dissipation rate, ω . The model is combining the $k-\epsilon$ and the $k-\omega$ models by applying the $k-\epsilon$ model in the free stream flow outside the boundary layer and the $k-\omega$ model in the viscous boundary layer, efficiently exploiting the benefits of both models. This strategy is enhancing the modelling of the flow in the boundary layer, but also increases the requirement for the y^+ value of the cells closest to the wall, making them smaller compared to the $k-\epsilon$ model requirement [54].

The turbulent kinetic energy k is defined as follows [50].

$$k = \frac{1}{2} \overline{u_i'^2} \quad (2.38)$$

In this model the Reynolds stresses are computed with the Boussinesq assumption as shown in Equation 2.39 for an incompressible case [50].

$$-\overline{u_i' u_j'} = \nu_t \left(\frac{\delta u_i}{\delta x_j} + \frac{\delta u_j}{\delta x_i} \right) - \frac{2}{3} k \delta_{ij} \quad (2.39)$$

δ_{ij} is the Kronecker delta which for $i = j$, $\delta_{ij} = 1$ and for $i \neq j$, $\delta_{ij} = 0$. μ_t is the turbulent viscosity, a model parameter obtained from multiple experiments. The transport equation for the turbulent kinetic energy used in the SST model is the following transport equation [54].

$$\frac{\delta k}{\delta t} + u_j \frac{\delta k}{\delta x_j} = P_k - \beta^* k \omega + \frac{\delta}{\delta x_j} \left[(\nu + \sigma_k \nu_T) \frac{\delta k}{\delta x_j} \right] \quad (2.40)$$

The specific dissipation rate is modelled as follows [54].

$$\frac{\delta \omega}{\delta t} + u_j \frac{\delta \omega}{\delta x_j} = \alpha S^2 - \beta \omega^2 + \frac{\delta}{\delta x_j} \left[(\nu + \sigma_\omega \nu_T) \frac{\delta \omega}{\delta x_j} \right] + 2(1 - F_1) \sigma_{\omega 2} \frac{1}{\omega} \frac{\delta k}{\delta x_i} \frac{\delta \omega}{\delta x_i} \quad (2.41)$$

The model constants in this model has been adjusted after the release of the model in 1993. The constant values are presented below and were used unchanged in this thesis [55].

$$\begin{aligned} \sigma_k &= 0.85 & \sigma_{\omega 1} &= 0.5 & \sigma_{\omega 2} &= 0.856 & \beta^* &= 0.09 \\ \beta_1 &= 3/40 & \beta_2 &= 0.0828 & \alpha_1 &= 5/9 & \alpha_2 &= 0.44 \end{aligned}$$

The SST model requires y^+ in the order of 1 for the cells close to the wall and a sufficient resolution inside the boundary layer. This is achieved with growth ratios less than 1.15, and will roughly result in up to 30 cells inside the boundary layer [55].

Methodology for the experiment design development

The rig design is based on basic principles described in the Theory. The scope of this chapter is a detailed description of the development of a test rig design. This development process is divided into three separate steps.

Firstly, the choice of the hydraulic design principle is described. The design is made with an ambition of creating a setup applicable to actual hydropower systems. Therefore, the design is made to imitate the draft tube section in a turbine, where the static pressure is at its lowest. This section will introduce three initial alternative setups and explain how the final setup was chosen.

Thereafter, the dimensioning of all parts of the test rig based on theoretical principles will be presented. The hydraulic design of the test rig is governed by basic fluid mechanics and the study aims to construct a rig with a predictable, attached flow pattern through the system and hence, obtain a justified design of the setup geometry.

Finally, two procedures for producing supersaturated water are suggested along with an example of how flow rate regulation and obtaining a constant flow rate can be implemented in the setup. A presentation of the ultrasound equipment and the measurement probes required to execute and monitor the experiments accurately is given. The chapter is completed by a suggested methodology for performing the experiments on the test rig.

3.1 Developing an experiment setup design

The rig to be designed needs to fulfill a certain set of criteria. The purpose of the rig is to conduct experiments to determine whether degassing flowing water from a hydropower plant by employing ultrasound is an effective solution. As well as proving the concept,

determining whether the test rig can be a design starting point for a prototype solution is of interest. The test rig will also be used for investigating which factors are affecting the degassing to optimize this process. The following criterion are set for the test rig:

- Production of supersaturated water should be done in the setup. The supersaturation level must be measurable and at a constant maximum level between 160 % and 200 %.
- The geometry should allow for flow of supersaturated water in an ultrasonic field and monitor the supersaturation level upstream and downstream the applied ultrasound to document the degassing effect.
- The geometry should be designed in order to minimize degassing effects from other influences than ultrasound.
- The rig should allow for a controlled supply of supersaturated water. Monitoring the flow rate, pressure and temperature in the system is required to control the flow conditions and uncertainties during experiments.
- The geometry should be comparable to a hydropower plant with a Francis turbine to represent a small scale solution which can be scaled up in a future continuation of the project.
- The rig will be built in the Waterpower Laboratory at NTNU, and is constrained by the facilities found there.

3.1.1 Initial design proposal

The main ingredient for the experiment setup is supersaturated water. From theory, the solubility of air in water is increasing with increasing pressure and decreasing temperature. The temperature in the lab is stable and a pressure tank where 15 m³ of water can be pressurized is available. This tank was chosen to be the starting point for the test rig.

A first draft of a test rig was developed and can be seen in Figure 3.1. This initial proposal was made as a concluding setup for the project thesis delivered the autumn 2019 [1]. The setup was made with oxygen-saturated water, and dissolved oxygen probes will not be sufficiently accurate for determining the air saturation level, as described in the Theory. The setup presents two different configurations. Both configurations start at the pressure tank, to the right in the figure, where supersaturated water is flowing from right to left. In the first configuration a small pipe beginning at the bottom of the pressure tank leads the supersaturated water into the rig. The pipe goes through an ultrasound transducer, where ultrasound is applied. It continues through the pipe where dissolved oxygen content is measured with a DO-probe. From here the water is dumped in the lower reservoir below the building. The second configuration leads the water through the Francis test rig. A flow meter is monitoring the flow rate and ultrasound is applied to the water. Further, the water is led through the draft tube tank. In this setup the pressure and temperature are measured

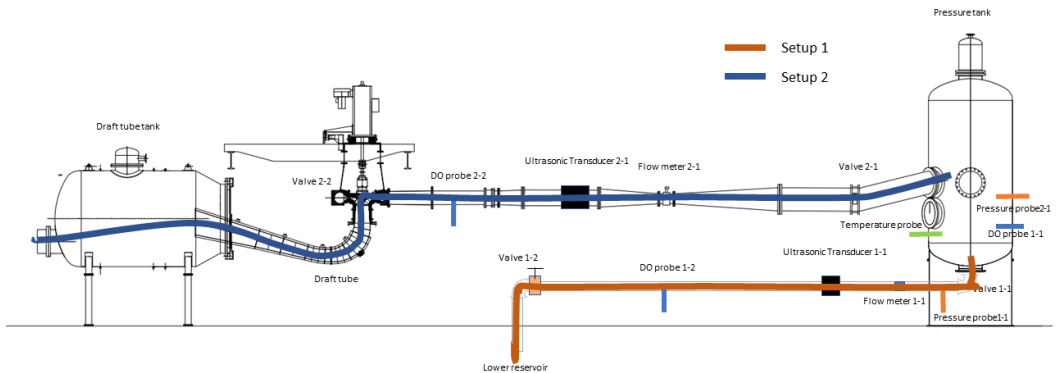


Figure 3.1: A first draft of the test rig in the Waterpower Laboratory at NTNU.

in the pressure tank, and dissolved oxygen is measured before and after ultrasound is applied to the water.

The advantage of scaling up from a small scale first configuration to a second configuration with higher flow rates is clear in this setup. Although, some disadvantages were noted. Firstly, producing sufficient amounts of supersaturated water for the second configuration is difficult as the outlet from the pressure tank is located at the midpoint of the tank. Hence, the lower half of the water content is not available for the experiment. Secondly, the uncertainty of whether degassed air can escape from the water, avoiding to be dissolved back into the system when flowing in a closed pipe is present. This phenomenon is hard to control, and therefore, the configuration containing closed pipes was discarded.

3.1.2 Second iteration design proposal

When rejecting the initial design proposal, the following learning points were considered. It was decided that taking water from an outlet at the bottom of the pressure tank was advisable due to the larger water volume available here. Additionally, the idea of applying ultrasound in a region with low pressure, i.e. in a draft tube bend, was a result of this setup configuration. Due to the low solubility of air at low pressures it is assumed that lowering the pressure further during the rarefaction part of the ultrasound cycle, can contribute to a more effective degassing process.

The design was developed further by keeping the pressure tank as the starting point of the setup. The ultrasound was to be applied in a draft tube-shaped bend, and the degassed air had to escape to the atmosphere after ultrasound was applied to the water. A new setup configuration was proposed and is shown in Figure 3.2.

At the outlet from the pressure tank, a draft tube-shaped pipe leads the water into a container with a weir plate. Downstream the weir plate the water flow down an open flume and is disposed in the lower reservoir by flowing over a new, lower weir plate. The ultrasound is supplied with a rod-shaped probe mounted on the pipe bend. The open flume

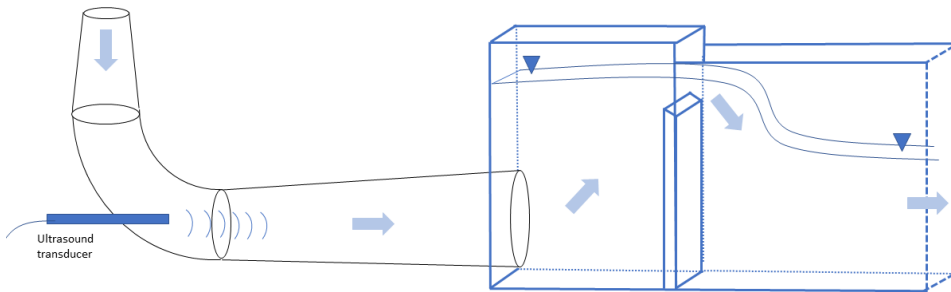


Figure 3.2: Entry section for the second setup configuration.

configuration has an advantage of enabling dissolved air to escape through the water-air interface. Easy access to the degassing water allows for more dissolved air measurements to be made in the open channel. Hence, observing how the degassing is developing in multiple locations downstream the ultrasound source is possible.

The second setup tackles one set of problems and presents a new set of challenges. Flow rate measurement in the setup is important to know the flow characteristics. If the flow is measured upstream the ultrasound source the size of the flow meter is limited by the small space beneath the pressure tank. One typical flow measurement method in closed pipes is by using ultrasonic flow meters. The introduction of two ultrasound sources to the setup is deemed suboptimal due to the resulting uncertainty in separating their individual effect. Therefore, the preferred flow measurement method is a V-shaped weir plate mounted at the end of the long flume. This solution allows for flow measurements which do not disturb the flow in the measurement section of the flume.

The purpose of the initial overflow weir is to ensure a uniform flow in the flume and avoid surface waves disturbing the flow measurement over the V-shaped weir. Separation in the diffuser section of the draft tube will induce surface waves in the flume, creating a transient flow regime. However, this weir plate will introduce an uncertainty to the degassing process, as predicting the flow field in the section between the outlet from the circular diffuser pipe and the weir-plate is challenging. The flow over the top of the weir-plate introduce mixing of water downstream the plate. This flow pattern is dependent the flow rate and introduce an uncertainty in comparison of the degassing process at different flow rates.

Further, flow rate control could be done by introducing a valve at the outlet from the pressure tank. Although, a valve will disturb the flow and create large turbulent recirculation regions, highly dependent on the flow rate. This is not a favourable property as comparison of different flow rates again produces large uncertainties. Therefore, a different control mechanism of the flow rate is proposed. By supplying the setup with water through one or two hoses the flow rate can be controlled by varying the length, diameter or number of the hoses. Hence, it becomes possible to make comparable setups for different flow rates by varying the friction loss. The flow rate in the flume is depending on the potential energy of

the water stored in the pressure tank. This is defined by the height of the water column and the losses through the enclosed water system, including sudden expansion losses, diffuser losses, bend losses and friction losses in the enclosed part of the system. From Equation 2.2; for a constant flow rate, the friction loss in a pipe is increased by increasing the length or decreasing the flow area. By utilizing this phenomenon, a flow rate control mechanism can be constructed and is exemplified in section 3.4.

When applying the flow control mechanism, the water level in the pressure tank will decrease with time, and measurements cannot be taken for long periods with the same flow rate. The surface area in the pressure tank is relatively large compared to the flow area in the setup, so the change in potential energy over time is assumed to be negligible in short time intervals. Although, this point must be monitored carefully to be aware of any uncertainties related to the flow rate and is discussed further in section 3.5.

The cross-section of the draft tube-shaped bend is affected by production costs, and should be made as cheap as possible. Conventional draft tubes often have a transition from circular pipes to rectangular shapes, but in this setup rectangular shapes are used for all three parts of the draft tube. While the setup differs from the traditional draft tube design, the results are still believed to be transferable and to give novel insight. This makes the flow structure cheaper in production and the mounting of the ultrasound transducer more convenient.

3.1.3 Final design configuration

Concluding the design development procedure, the final design configuration is as presented in Figure 3.3.

Supersaturated water is produced in the pressure tank. It flows into the draft tube-shaped bend through one or two hoses of adjustable length and diameter. A valve is placed at the draft tube inlet to remove air when filling the rig. At the bottom of the pressure tank a measurement section is installed with an option to close of the setup completely from the pressure tank to allow for other experiments on the Francis rig while this rig is installed. The measurement section will monitor pressure, temperature and air saturation in the tank. Supersaturated water is led through a draft tube-shaped structure where ultrasound is applied to the water in the bend. The water flows steadily into the open flume where it is degassing, and measurements of air saturation can be made multiple places. Finally, the water flows over a V-shaped weir plate and a pressure measurement is determining the flow rate in the system.

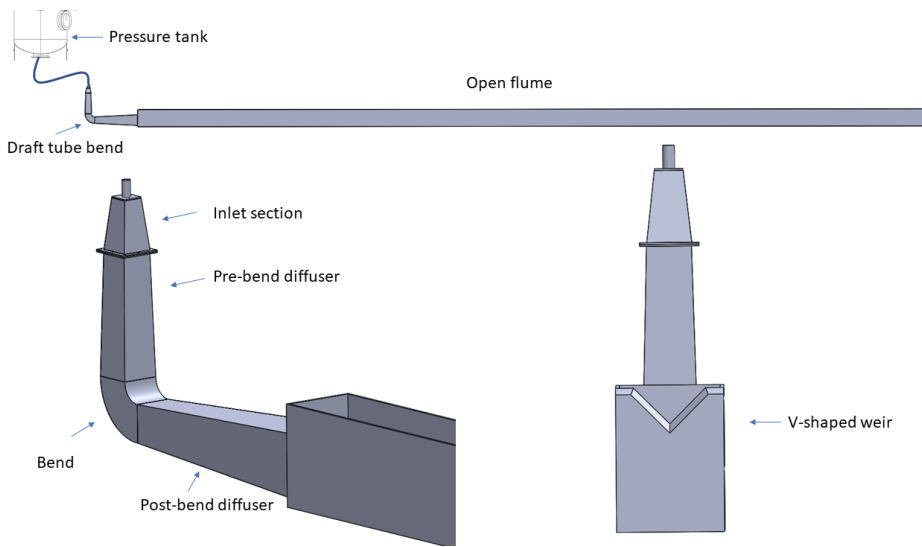


Figure 3.3: Final experiment setup layout.

3.2 Dimensioning the experiment setup

Dimensioning the parts in the chosen setup includes specifying the dimensions of the inlet diffusers, the pre- and post-bend diffusers, the bend, the flume and the weir plate. The design criteria include obtaining an attached flow in the draft tube-shaped section prior to the flume, a steady sub-critical flume flow and a weir plate with a capacity of measuring flow rates up to 4 L/s accurately. This flow rate is assumed to be a fair compromise between the large flow rates used in hydropower research and the small flow rates used in ultrasound research. It is a starting point for the implementation of ultrasound technology into hydropower research.

3.2.1 Diffuser dimensions

The dimensioning of the setup begins with the diffuser sections. The two main diffusers are placed on either side of the bend as seen in Figure 3.3. The first diffuser is slowing down the flow before the bend to avoid separation through the bend, and the second diffuser is slowing the flow down further towards the outlet to the flume. In addition to these two diffusers, the inlet section is diffuser shaped. This is done because the number of hoses leading water to the draft tube inlet should be easy to change. Therefore, two diffuser shaped inlet parts are made as shown in Figure 3.4. The single-inlet part fits only a single hose to the draft tube inlet and the double-inlet part fits two hoses at the inlet. These two diffusers are shorter and with a larger expansion angle. Dimensions and properties of the diffusers are shown in Table 3.1.

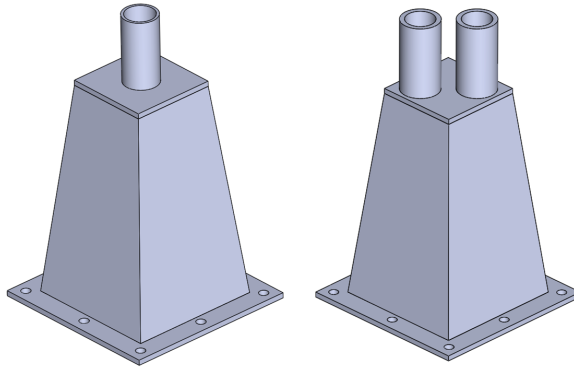


Figure 3.4: Two different inlet sections made for the setup. To the left: option to connect one hose, inlet 1. To the right: option to connect two hoses, inlet 2.

The inlet diffusers 1 and 2 lead the water from the hose to the pre-bend diffuser with the aim to make this transition as smooth as possible by increasing the flow area. As stated in Table 3.1 the diffuser is not exposed to separation in a case where a uniform, fully developed flow is entering the diffuser. Although, the inlet part also has a sudden expansion which makes the approaching flow anything but attached in this region. The reason for making this rather violent transition is to enable an easy change from using one hose to two hoses by replacing a relatively small part in the setup. This region can be problematic for comparing different flow rates as the flow pattern will change with changing flow rates. The hoses to be fitted to the inlet sections has an inner diameter of 40 mm but can be changed to smaller diameters if needed.

Diffuser name	Inlet height	Diffuser length	Outlet height	Diffuser angel, β	Predicted separation
Dimension	mm	mm	mm	deg	yes/no
Inlet 1	80	200	125	6.4	no
Inlet 2	80	200	125	6.4	no
Pre-bend	125	480	150	1.5	no
Post-bend	150	1000	250	3.0	no

Table 3.1: Diffuser dimensions for the different diffusers included in the setup. Predicting the separation in these diffusers based on the data in Table 2.1 is also included in this table.

The pre-bend diffuser is designed conservatively to allow the flow to reattach and slow down before the bend. An expansion of $2\beta = 3^\circ$ is smaller than the required maximum expansion of 12° to avoid separation. The final, post-bend, diffuser is also conservatively designed. This diffuser has a challenging inlet flow as the bend induces a rotational velocity component, and the flow direction is changed 90° prior to the diffuser. To make sure that the outlet flow from this diffuser is attached and uniform it is designed with a total expansion of $2\beta = 6^\circ$ instead of the required maximum of 10° . The expansion for both the

pre- and post-bend diffusers is within the recommended expansion angles for draft tubes of $3^\circ - 6^\circ$ from the centreline. Ensuring an attached flow in this area, avoiding unsteady flow and surface waves in the downstream flume, assures accurate flow measurements with the V-shaped weir which is depending on a uniform, steady flow upstream. Making the diffuser longer is an option but is avoided as the risk of air bubbles dissolving in the water in this region is increased with a longer diffuser. It is also favourable to utilize the available space in the lab for monitoring the degassing in the open flume.

3.2.2 Bend design

The bend cross section is set to 150 x 150 mm to fit the diffusers. The R/D- ratio is decided to obtain the lowest loss through the bend possible. From the theory, a low loss is resulting from an attached, efficient flow which is favourable. By using the maximum flow rate of 4 L/s, losses for different R/D-ratios are calculated with Equation 2.21, and plotted in Figure 3.5. The bend loss equation is made for circular pipe cross sections, but is assumed applicable in this case. A small bend is cheaper to produce and, hence, a R/D-ratio of 1 is chosen for this setup. It is seen from Figure 3.5 that the loss reaches a minimum around $R/D = 2$, but the change in loss is small and lowering the ratio to 1 can be done without any major disadvantages.

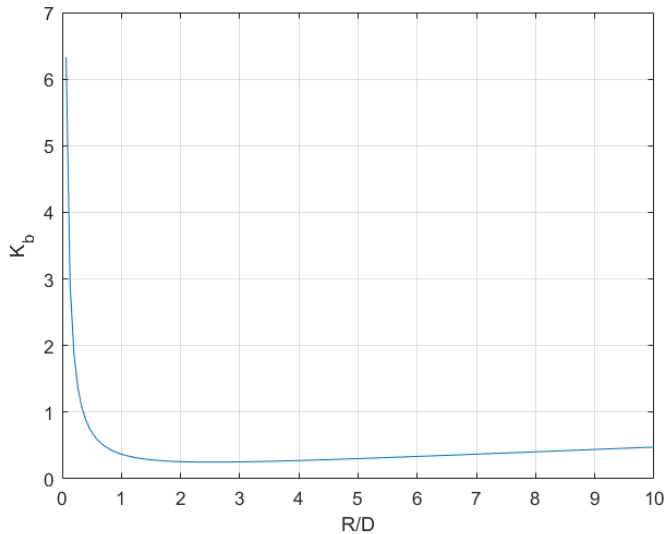


Figure 3.5: Plotted loss coefficient for bend at a flow rate of 4 L/s for different values of R/D.

3.2.3 Flume design

The open flume has a relatively simple design, although some complicated flow structures can occur here. The flume must be sufficiently wide to obtain a good design for the weir-plate downstream, and sufficiently high to sustain a flow rate of 4 L/s. Additionally, the size of the flume is constrained by the total weight of the water and the flume structure on the floor of the lab. The width of the flume is set to be 300 mm and the height to be 400 mm. This results in a sudden expansion in the transition between the outlet of the post-bend diffuser and the flume. The length of the flume is important for measuring the evolution of the dissolved air content downstream the ultrasound source. Since the degassing efficiency is unknown at different distances from the ultrasound source it is useful to be able to measure the total dissolved gas content multiple times in the flume. Measurements should have 5 meters distance between them and avoid measurements at the inlet where the flow is stabilizing and at the outlet where the weir plate is changing the flow regime upstream the plate. With a total length of 17.5 meters the flume can fit inside the lab, allow for three measurement points for the total dissolved gas measurement and avoid operating in the disturbed flow downstream the flume inlet and upstream the weir plate.

The flow loss in the flume can be estimated from a variation of Equation 2.2 where the definition of the hydraulic radius for an open channel is applied to the equation along with an estimated friction factor of 0.03. The flow loss in the flume is determined by the potential energy stored in the slope of the water surface. This slope is given as the tangent of the slope angle. By estimating an average flow area of 0.3m x 0.395m at the maximum flow rate of 4 L/s, the obtained loss in the system is in the order of 1e-05 meters, which is very small. This is due to the low flow velocity in the flume. Also, the angle of the water is negligible, and an overflow at the inlet of the flume is not a problem unless the flow is unsteady with surface waves. Hence, the loss in the flume is neglected in further calculations.

3.2.4 V-shaped weir plate design

The V-shaped weir plate is designed according to the ISO1438 standard. The standard dictates that the thickness at the top of the plate should be 1-2 mm. The slope from the top edge is set to 45 ° and the total thickness of the plate is 10 mm. The V-notch has an opening angle which is chosen to be 90° due to detailed data provided in the standard for this notch angle. The height of the notch is set to be 100 mm. With this configuration flow rates from 0 to 4.5 L/s can be measured. The flow rate with different heights is calculated with Equation 2.27 and is plotted in Figure 3.6 along with the weir plate design.

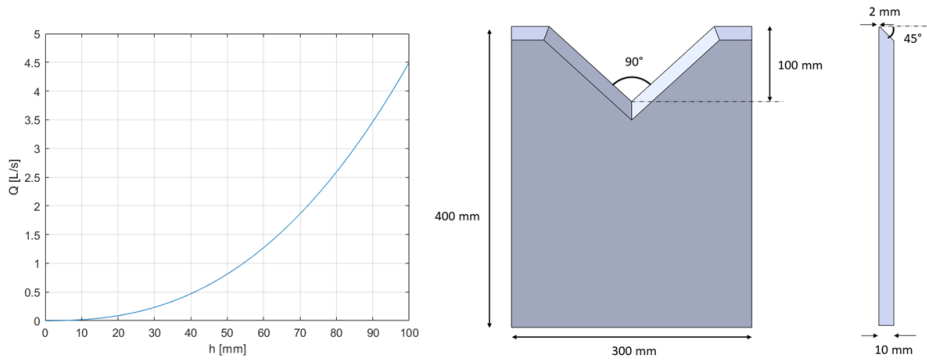


Figure 3.6: Left: Flow rate, Q , through the V-shaped weir notch for measured heights above the notch bottom, h , between zero and 100 mm. Right: weir plate with dimensions.

3.3 Producing supersaturated water with air

The main ingredient for the experimental setup is supersaturated water. Producing supersaturated water is a process that is dependent on pressure, temperature and available air in a closed system, in addition to the time constants for the process where air is dissolved in water. The required maximum supersaturation level in the tank is between 160 % and 200 % which correspond to the levels in hydropower rivers found in the literature. A brief outline of some possible production strategies is illustrated in this section.

Supersaturated water can be created with different approaches. Firstly, it is possible to pressurize the pressure tank with air and leave the system to rest. An equilibrium between the air pressure in the air and the partial pressure in water will eventually occur. This however, is a slow process as air has to diffuse through the surface into the water.

A similar approach is injecting air into the tank from the bottom through a filter that creates micro bubbles. This technique is used in beer brewing to inject micro bubbles of oxygen into the wort prior to fermentation. By using a diffusion stone placed in a pipe, micro bubbles are produced as air pressure is applied to it through the pipe. When the tank is under pressure and bubbles are injected from the bottom, air is evenly distributed into the liquid. It is assumed that the time constant for obtaining an equilibrium will be shorter by using this approach as air is distributed in the water and the effective surface area is increased. When air is injected in the liquid for a specified time period, and the gas content is monitored by a probe at the bottom of the tank, the resulting supersaturation level can be controlled.

The above described strategies for creating supersaturated water will result in a limited water volume available during the experiments. The flow rate is regulated with the pressure loss in the pipe system and the pressure head in the pressure tank. It is favourable for the experimental quality to have a constant pressure head in the tank to ensure a constant flow rate, and this is possible by utilizing a solution from the aquaculture industry. To ensure a

stable supply of oxygen rich water to aquaculture fish an oxygenation cone is used. The principle is illustrated in Figure 3.7.

Water is led into the top of the cone where gas and water is injected through separate inlets. Gas bubbles which are not dissolved in the water will float to the top of the cone and avoid being transported with the supersaturated water leaving the cone at the bottom. With a pressurized system the saturation level in the water will increase as the water velocity is reduced when flowing through the expanding cone. It is important to ensure a sufficiently high pressure in the pipe system to avoid degassing of water after leaving the cone [56]. Additionally, avoiding that the water experiences a steep pressure gradient towards the outlet, by prolonging the outlet pipe, allows the water to sustain the supersaturation level. In the described setup, the cone can be placed between the pressure tank and the draft tube rig and pressurized air is supplied at the top of the cone. With a constant water level in the pressure tank the flow rate will be constant through the system, without a pump to supply the cone with water. Thus, a constant flow of supersaturated water into the experiment rig is possible.

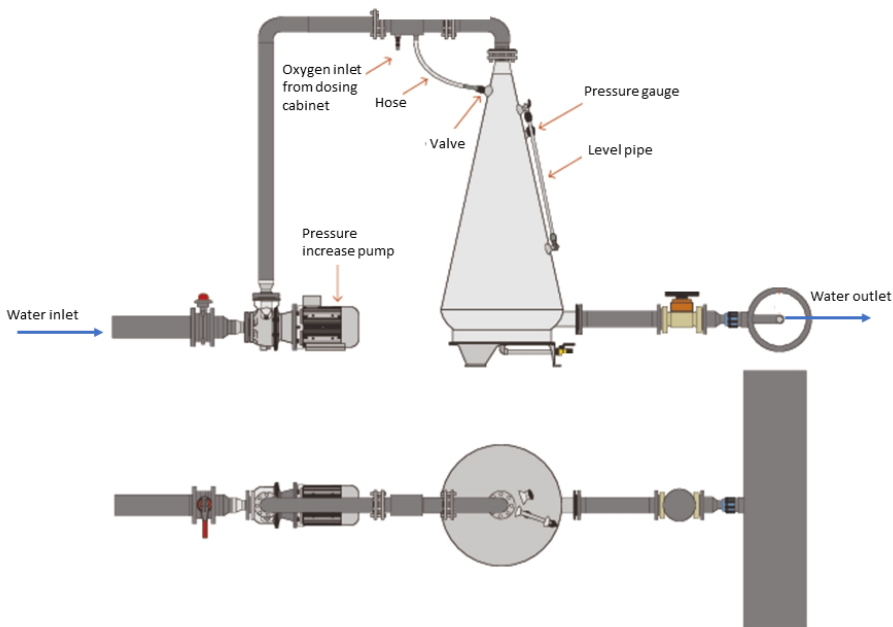


Figure 3.7: Working principle of oxygenation cone used in aquaculture. Modified from [56]

3.4 Flow rate regulation

Two alternatives for producing supersaturated water were presented in the previous section. The first configuration allows for production of a fixed volume of supersaturated water in the pressure tank. The second configuration allows for a constant water level in

the pressure tank and a constant flow rate in the setup as supersaturated water is produced in the cone-system. For the first configuration it is useful to look at an approximation of the flow rate as a function of liquid height in the pressure tank. Further, in both configurations it is of interest to establish a method for calculating the length of the pipes which produces the required friction loss and hence, flow rate through the setup. This section is briefly demonstrating such a calculation, and further presents advantages and disadvantages with the two principle designs for creating supersaturated water. All calculations in this section are based on fluid flow equations given in the Theory, and the MATLAB script used to generate the figures is attached in the Appendix.

For all loss calculations the friction factors in the setup are estimated. The friction factors are varying with Reynolds number in the flow range used in this thesis but are assumed to be constant for demonstration purposes. The inlet pipes are plastic pipes with estimated friction factors between 0.02-0.04. Hence, 0.03 is used as an approximation. The same number is used for the draft tube and flume which are made from stainless steel, AISI304. The friction factor is in general increasing with decreasing flow rate.

Figure 3.8 shows how the flow rate changes with water column height in the pressure tank minus the flow losses. The flow rate is obtained by using Torricelli's law which states that all available potential energy is converted into kinetic energy. The losses are dependent on the flow velocity, and are estimated in Figure 3.9, excluding the loss in the inlet pipes. Controlling the flow rate by varying the loss in the inlet pipe is done by calculating the pipe losses for the desired flow rate. How the loss is changing with pipe length and flow rate for a single-inlet pipe configuration is calculated and presented in Figure 3.10 for five different flow rates.

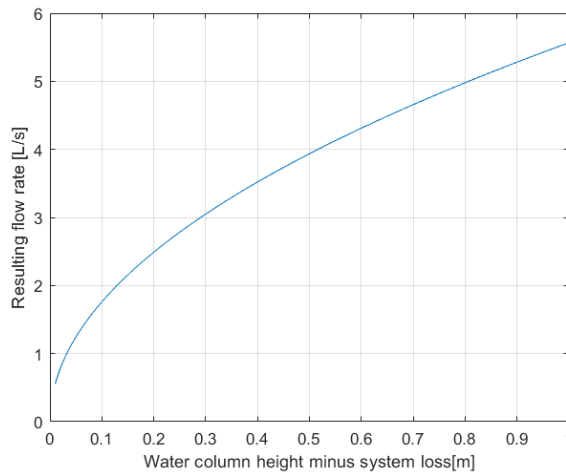


Figure 3.8: The resulting flow rate in the system obtained from applying Torricelli's law in the tank. The resulting flow rate is a result of the potential energy in the water column height in the pressure tank minus the hydraulic loss in the system.

Exemplifying a method for obtaining a desired flow rate of 3 L/s in the system Figures 3.8,

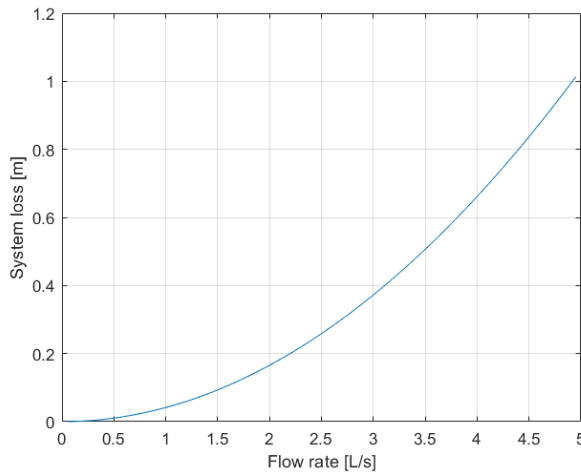


Figure 3.9: The total losses in the system excluding the friction losses in the inlet pipes. The losses vary with flow rate.

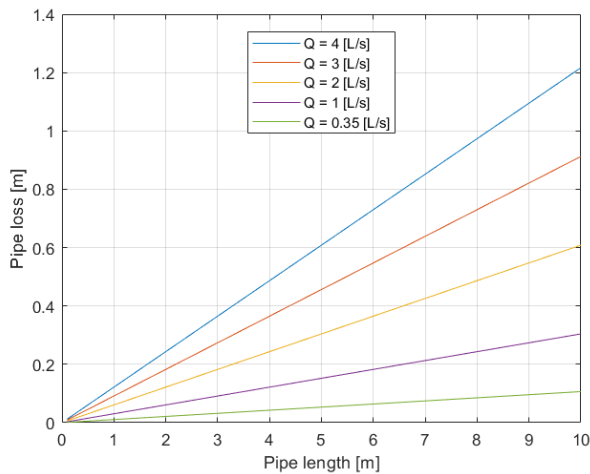


Figure 3.10: Pipe loss or single-inlet pipe configuration with pipe lengths varying from 0 to 10 meters and flow rates of 0.35, 1, 2, 3 and 4 L/s.

3.9 and 3.10 are used. From Figure 3.8 a flow rate of 3 L/s is obtained by having a total head of 0.3 meters (actual head minus the system head loss). From Figure 3.9 it is found that the system loss excluding the pipe loss will be about 0.38 meters at 3 L/s. Further, Figure 3.10 shows that a flow rate of 3 L/s and a pipe length of 5 meters gives a pipe loss of approximately 0.45 m by using a single pipe inlet. By choosing this configuration the required level in the pressure tank is 1.13 meters to obtain the desired flow rate of 3 L/s.

Additionally, the same flow rate can be obtained by a shorter pipe and a lower pressure tank level, or a longer pipe and a higher water level.

3.5 Obtaining a constant water level in the pressure tank

When applying the aquaculture cone for producing supersaturated water in the setup, a constant water level in the pressure tank can be used. Controlling the flow rate is crucial for obtaining low uncertainty in the experiments. With a desired flow rate of 4 L/s and a fixed volume of supersaturated water, the tank level will sink at a rate of 6,3 centimetres per minute. This results in a lowering of the tank level of 31.6 cm during a five-minute period and the flow rate will decay significantly during this time. The lowering of the water level in the tank is therefore complicating the experimental process. Hence, keeping a constant water level in the pressure tank is of interest for minimizing uncertainty and improving the setup. A close to constant tank level will allow for standardisation of the pipe lengths needed for different experimental flow rates.

Such a solution can be implemented in the Waterpower laboratory at NTNU by applying the pump located in the basement of the lab to supply the pressure tank with water from the lower reservoir. The setup in the lab is illustrated in Figure 3.11.

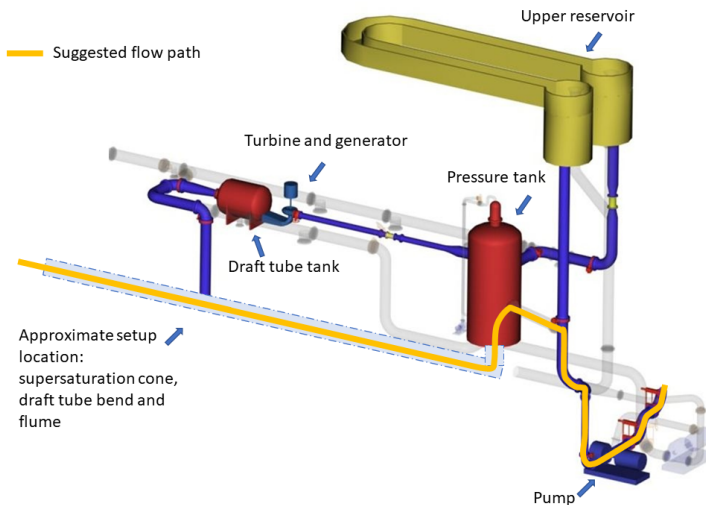


Figure 3.11: The suggested flow path in the Waterpower Laboratory at NTNU. The flow is directed from the pump into the pressure tank and through the supersaturation cone, draft tube bend and flume, before flowing back into the lower reservoir.

The pressure head delivered by a pump at a given flow rate and rotational speed is determined by the pump characteristics. For the test rig the flow rate is relatively small compared to the capacity of the pump, and hence at one constant rotational speed the pressure head in the pressure tank can be considered constant. Obtaining a suitable rotational

speed for the pump is done by experiments, and for this fixed head, standardized pipe lengths for flow regulation can be made. The pump will be working in idle with a low flow rate, but this mechanism is an effective head regulator. The minimum water level in the pressure tank is the level of the inlet pipe to the tank shown in Figure 3.11. After entering the pressure tank, which is closed off from the upper reservoir and the Francis rig, water will flow through the flow regulation pipes with sufficient friction loss, the cone to become supersaturated and further into the flume through the draft tube bend. With this configuration experiments will be easier to conduct, and results will be less affected by uncertainties.

3.6 Ultrasound design

As previously mentioned, it is favourable to place the ultrasound transducer and probe in the draft tube section of the setup to mimic a degassing process in a low pressure area of a future prototype. The goal is to expose the water to ultrasound for as long as possible and at the same time disturb the flow as little as possible. Nevertheless, the main goal of this thesis is creating a setup which can prove whether the degassing of flowing water is efficient. Hence, the ultrasound design is made mainly with the intention of prolonging the residence time of the water in the ultrasonic field. The ultrasound equipment must be able to transmit ultrasound to the water at a relatively low frequency and at high power levels, which restricts the options of how the probe can be constructed.

The proposed transducer and probe design by SinapTec Ultrasound Technology is mounted in the draft tube bend as shown in Figure 3.12 below.

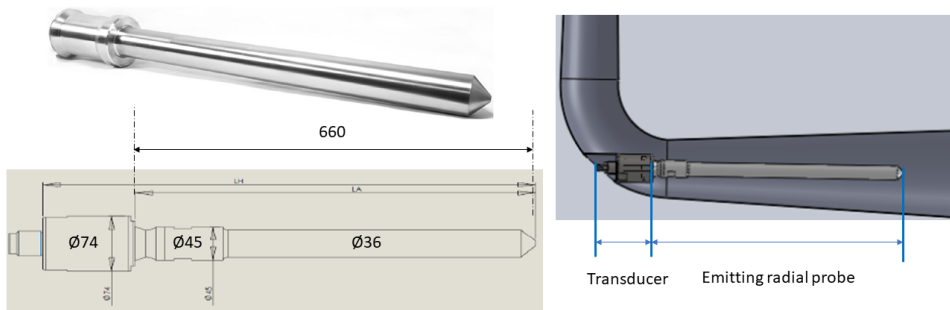


Figure 3.12: Ultrasound transducer and probe design and positioning in the bend section of the rig. The design is provided by SinapTec Ultrasound Technology and all stated dimensions are given in mm.

The probe is emitting ultrasound mainly in the radial direction, normal to the flow, exposing the water flowing through the bend and the post-bend diffuser to the ultrasonic field. Some ultrasonic waves will also be emitted in the flow direction. The purpose of the long probe is to prolong the residence time. The transducer is placed inside the flow area to

enable cooling of the transducer with the water flowing in the system. The transducer power is estimated to be 1000 - 1200 W rms by SinapTec Ultrasound Technology and the ultrasonic frequency is 20 kHz, close to the recommended frequency of 24 kHz, obtained in the project thesis [1].

3.7 Measurement equipment

Obtaining good results from an experiment demands correct choices of measurement probes. This subsection presents the different measurement probes for the setup, some specifications and the location of the probes. The location of the probes is specified in Figure 3.13 and probe specifications are listed in Table 3.2.

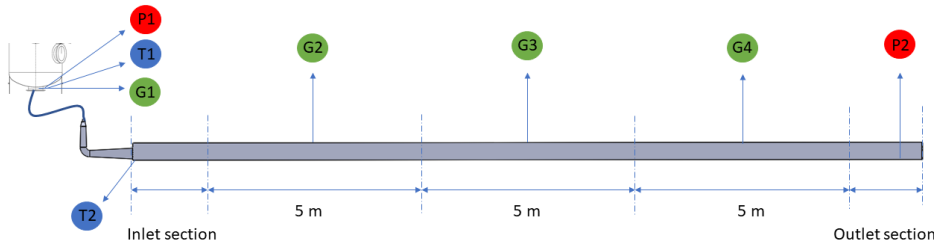


Figure 3.13: Location of all measurement probes in the experimental setup.

Sensor	Measurement	Probe type
P1	Gauge pressure	0 - 3 bar pressure sensor, GE UNIK 5000
P2	Gauge pressure	Specified in ISO1438
T1	Temperature	PT100
T2	Temperature	PT100
G1	Gas pressure in water	Permanent, long response time, 20 minutes
G2	Gas pressure in water	Temporary, short response time, 5 minutes
G3	Gas pressure in water	Temporary, short response time, 5 minutes
G4	Gas pressure in water	Temporary, short response time, 5 minutes

Table 3.2: Measurement probe specifications for the measurements to be made in the setup.

Monitoring the properties of the water entering the draft tube section is important. Therefore, pressure, temperature and gas saturation are measured at the outlet of the pressure tank using pressure probe P1, temperature probe T1 and gas saturation probe G1. Further, when utilizing the water in the rig as cooling water for the ultrasound transducer it is necessary to monitor the temperature change caused by the cooling. A temperature change in the water can affect the degassing process, therefore, temperature sensor T2 is placed at the inlet to the flume to capture this change. Further, the gas saturation level is measured at three points in the flume with 5 meters distance between them with gas probes G2, G3

and G4. Finally, the pressure measurement for the weir flow is located upstream the outlet to determine the flow rate. Specifications for this sensor is described in the ISO1438 standard.

The temperature sensors are required to measure temperatures in the range between 10°C and 50°C. The change in temperature over time is small and detecting rapid changes in temperature is not necessary as the temperature in each location is assumed to be close to constant during each experiment. The choice of temperature probe for the experiment is therefore a PT100-element for application T1 and T2.

For the gas saturation measurements two different probe types are required. G1 is a permanent installation and is required to be in place for a long time. The saturoimeters which can sustain this treatment without changing behaviour tend to have a longer response time, 20 minutes, before accurate measurements can be taken. This is due to the time required for the gas pressure to equalize in either side of the measurement membrane of this probe. The second probe type is a short response time saturoimeter with a 5-minute response time. These saturoimeters can only be placed in water for a restricted time period as the membrane cannot be in contact with water for more than about 1 hour. Therefore, these probes require easy access and must be removed between each experiment to maintain accurate results. As a permanent probe is required, the choice for G1 is therefore a permanent saturoimeter with long response time. The saturoimeters G2-4 are chosen to have shorter response time to be able to conduct effective experiments where the water is running for as short as possible before the measurements can be taken.

The probe used in the pressure tank to monitor the pressure in the tank is a 0 - 3 bar probe. This is sufficient for monitoring the level in the tank during the experiments as no rapid changes or pulsations are expected in this area.

3.8 Suggested experiment procedure

Performing experiments on degassing water with ultrasound requires minimizing the experimental error by conducting well defined experiments. From theory, the random error is minimized by performing a large number of measurements during each experiment, in addition to repeated experiments. The resulting measurement values are averaged for each experiment and similar experiment are compared. Additionally, the systematic errors are minimized with thorough calibration of the measurement equipment. It is important to ensure all measurement equipment is well calibrated before measurements can begin.

Initially, commissioning tests are essential to document different properties of the setup. Three major question marks arise regarding the behaviour of the setup. Firstly, establishing how supersaturated water in the pressure tank behaves is of interest. For a case where supersaturated water is produced in the pressure tank these tests include monitoring what pressure should be applied to the tank, how much air should be injected and what time intervals are required to establish an equilibrium in the tank to obtain the desired supersaturation levels. Further the change in gas saturation in the tank when the over-pressure is released must be monitored. The over-pressure is released when a sufficient saturation

level is reached. For a case where an aquaculture cone is used to produce supersaturated water the obtained levels must be monitored by measuring gas saturation downstream the cone. For this application, a measurement section can be made close to the draft tube inlet, with a long response time permanent satumeter probe.

Secondly, the flow rate control system is established. If a fixed volume of water is used, the flow rate must be monitored over time to evaluate the effects on the flow rate as the water level in the tank is reduced. This is necessary due to lack of knowledge of the exact friction factors and detailed information about the flow filed impacting the losses in the system. For a case where a constant level in the tank is chosen, the ideal water level should be identified in order to produce the flow rates desired in the experiments by regulating with losses in the inlet pipes.

Thirdly, verifying that the flow is smooth and steady in the flume at all applied flow rates is essential for accurate flow rate measurements.

When the commissioning tests are completed the experiments can begin. The strategy should be to divide the experiments into test series where each series has one specific flow rate. The individual series should include tests with different ultrasound power levels, for instance with amplitudes from 0 % to 100 % with 20 % increments. All experiments are repeated three times and results are averaged from these three repetitions. Beginning with a relatively low flow rate, which implies a relatively large residence time, and a high ultrasound power level will give an impression of whether the concept of degassing flowing water is effective.

Irrespective of which strategy is used for creating supersaturated water, the measurements should be taken during a time period where the total dissolved gas content in water and the flow rate is constant, or it is reasonable to assume constant values.

Numerical methodology and setup

The tool used in this thesis to verify the previous flow calculations is computational fluid dynamics (CFD). The flow in the experiment setup can be modelled in a steady state calculation to obtain a good picture of the flow structure and possible challenges related to the flow field during experiments. The numerical calculations can also be helpful in predicting which operational conditions of the setup that can be compared in experiments as an impression of the location and size of the recirculation zones and separation points can be obtained from this analysis. Although, the analysis is simplified to some extent compared to the physical setup to avoid complex modelling. The model inlet is in the draft tube inlet and the first meter of the flume is included but modelled as a closed pipe. Additionally, the model does not include supersaturated water, and the ultrasound probe is excluded. The procedure of building the geometry, meshing and running the simulation is described in the following subsections.

The software used for numerical simulations is ANSYS CFX. CFD-solvers like ANSYS CFX are built up with five different software packages. The first is building the geometry, the second is constructing the mesh and the third is preparing the input files for the solver. The fourth software is the solver computing the solution, and the final software is post-processing the results. In this thesis ICEM CFD is used for creating the geometry and preparing the mesh, CFX - pre is the pre-processing software and CFX-Solver Manager is used for setting up and perform the computations. Finally, CFD - post is used for post-processing the results.

4.1 Geometry

The geometry used for the numerical calculation is a representation of the planned geometry for the setup with some simplifications. As mentioned earlier in this thesis, two-phase flow is complex to model, and therefore the flume part of the setup is simplified to be a

filled pipe avoiding the modelling of a water - air interface. The height of this flume pipe was set to 350 mm as the height will vary between 300 and 400 mm in this region for different flow rates. This is an approximation made to simplify the analysis, and the resulting flow in this area must be considered with this simplification in mind. Additionally, only the first meter of the flume is modelled in the calculation assuming that the most interesting flow patterns and flow rate-dependent phenomena are located in the draft tube-shaped part of the rig and in the outlet to the flume. The pipes leading water from the pressure tank to the inlet of the inlet diffuser are not included, and the inlet diffuser opening is the inlet of the simulated domain. Otherwise, the geometry is similar to the one described previously. The ultrasound transducer is not modelled in the geometry for this flow problem.

To compare the flows using the two different inlet diffusers one geometry is created for each inlet. The two geometries are drawn in ICEM CFD including the wetted surfaces only. The geometries are shown in Figure 4.1 below.

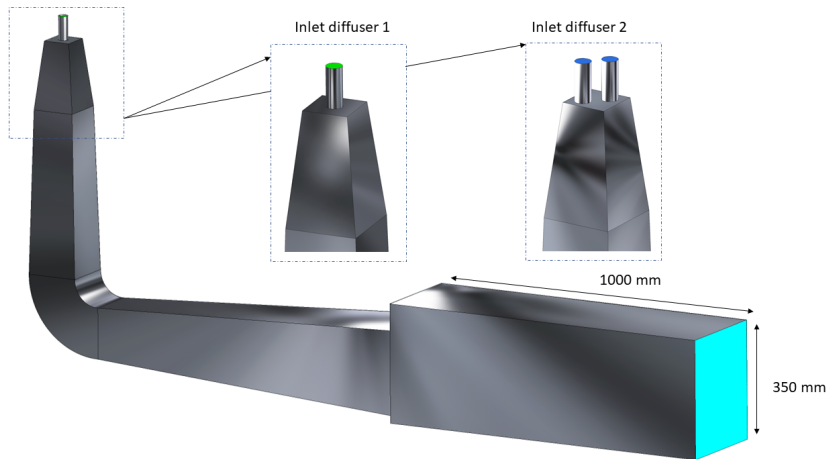


Figure 4.1: Model geometry created in ICEM CFD showing the two different inlet diffusers and the approximated flume geometry. The inlet surfaces are coloured green and blue, while the outlet surface is turquoise.

4.2 Mesh

The different cases to be simulated using CFD are one low flow rate and one high flow rate case for each flow geometry and turbulent flow. Additionally, one low flow rate case for each flow geometry with a laminar flow is modelled. The point of this choice is to reveal the differences in behaviour when the flow is in a laminar flow condition and a turbulent flow condition in the bend. Additionally, observing how the flow pattern at high and low flow rate behaves is of interest. Hence, these conditions have very different requirements for the mesh quality as the turbulent flow boundary layers need more cells to be modelled correctly.

The required cell height values for the first cell for the different flow regimes were calculated using Equations 2.28 - 2.31. Table 4.1 is showing details from the calculations of the flow conditions in the bend region.

Flow condition	Laminar	Turbulent 1	Turbulent 2
Free stream velocity, V [m/s]	0.0158	0.044	0.1778
Volume flow rate [L/s]	0.35	1	4
Water density at 19° C, ρ [kg/m ³]	998	998	998
Water dynamic viscosity at 19° C, μ [kg/m · s]	1.0256 · 1e-3	1.0256 · 1e-3	1.0256 1e-3
Reference length scale, bend height [m]	0.15	0.15	0.15
Required y^+ [-]	N/A	1	1
Bend Reynolds number, Re [-]	2 300	6 422	25 952
First cell height requirement, Δs [m]	0.001-0.002	0.0003	0.0001

Table 4.1: Input parameters and results from calculation of first cell height requirement for the mesh in laminar and turbulent flow condition in the bend.

There is no y^+ requirement in laminar flow, but a good modelling requires the gradients in the boundary layer to be captured well. Therefore, the first cell height used in the calculation was $\Delta s = 1 - 2$ mm over the geometries. By using a y^+ -requirement of 1 for the turbulent flow cases, required by the SST scheme, the Δs -value for the wall cells in the mesh for the high flow rate case was 0.1 mm, and 0.3 mm for the low flow rate case. The difference in the requirement for first cell height automatically leads to a large difference in the number of cells in a high quality mesh for the cases, but it is assumed that the same mesh can be used for the two turbulent flow cases with the most strict requirement fulfilled.

The main principles followed during the creation of the mesh was using a hexahedral, structured mesh. This is a natural choice in the presented geometry as it is characterized by square shapes. The mesh is also made to strictly obey the minimum size of the first cell, and the cells are made to gradually increase in height with the distance from the wall with a rate no larger than 10 % to 20 %. Also, cells must gradually increase in size to ensure that the cells in the vicinity are almost the same size as the cell of interest. The mesh is made with a large number of cells to ensure good results, and is designed using the criterion for mesh design in draft tubes found in the first Francis 99 workshop from 2014 [16].

To evaluate the quality of the mesh ICEM CFD includes a mesh quality tool where all cells are evaluated with different parameters. The ANSYS theory guide has specified a set of required minimum and maximum values for these parameters which must be satisfied to approve the mesh [51]. In this thesis the following requirements are evaluated and used to improve the quality of the mesh; the aspect ratio, minimum angle, the 2x2x2 determinant and the overall quality. Table 4.2 shows the requirements for these parameters in ANSYS CFX, and the obtained values from the different meshes used in the simulations.

When meshing a geometry in ICEM CFD, blocks are created to split the geometry into smaller parts. The mesh is then projected from the blocks on to the geometry surfaces. In

Parameter	Requirement	Laminar 1	Laminar 2	Turbulent 1	Turbulent 2
Angle	$> 36^\circ$	$> 40^\circ$	$> 40^\circ$	$> 40^\circ$	$> 39^\circ$
Aspect ratio 2x2x2	< 1000	< 25	< 20	< 83	< 136
determinant	> 0.5	> 0.67	> 0.75	> 0.92	> 0.87
Quality	> 0.3	> 0.65	> 0.65	> 0.65	> 0.64

Table 4.2: Mesh quality requirements and values for the four different meshes used. Laminar 1 and 2 are the meshes for the laminar flow with one and two inlet pipes respectively. The same system applies to the turbulent meshes.

the inlet section the mesh is more complicated compared to the rest of the flow domain as the geometry is exposed to a sudden expansion and changes from a circular cross-section to a square cross-section. This section is meshed by using an O-block topology from the inlet, propagating through the inlet diffuser, but not further into the geometry. For the inlet diffuser with two inlet pipes some additional splits of the blocks had to be made as shown in Figure 4.2

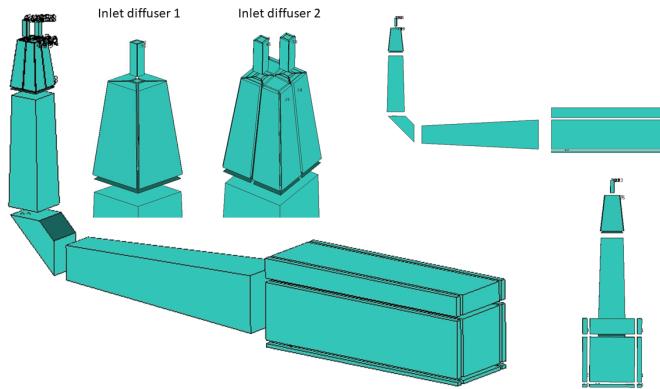


Figure 4.2: The block topology of the two geometries.

The meshes for the two different geometries are illustrated in Figures 4.3 and 4.4 below. Here it is clearly visible that the meshes are different both in the number of cells, but also in the distinction between the boundary layer flow and the free stream. In the laminar case the velocity gradient is less steep and the estimated requirement for the first cell height is so large that all cells can have the same width independent of whether it is located in the boundary layer or the free stream. In the turbulent cases, on the other hand, the y^+ requirement causes the boundary layer cells to be very small, and an increase in cell size from the walls towards the free stream is required in order to minimize the total number of cells in the domain. Also, some growth ratios are introduced in the interface between some of the blocks to avoid a large increase in cell size from one cell to the next. The growth ratios used are between 10 % and 20 %.

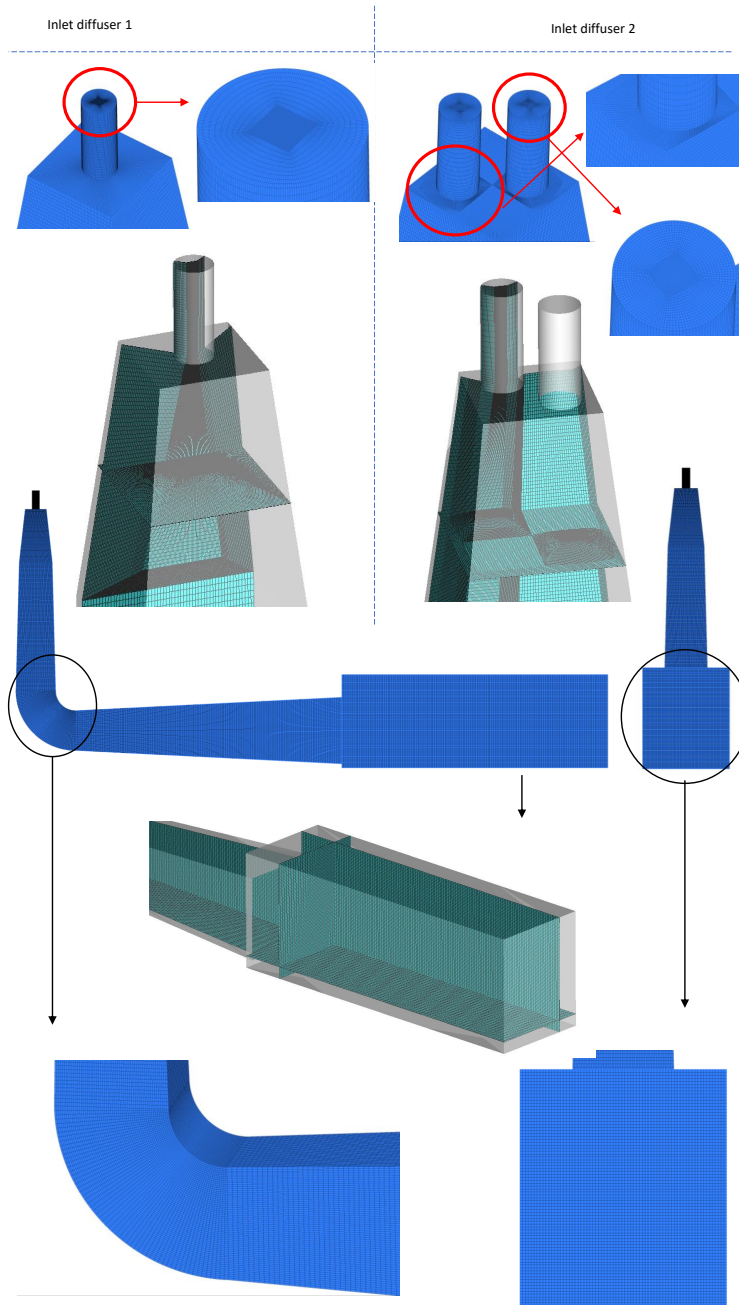


Figure 4.3: Mesh for the laminar flow cases.

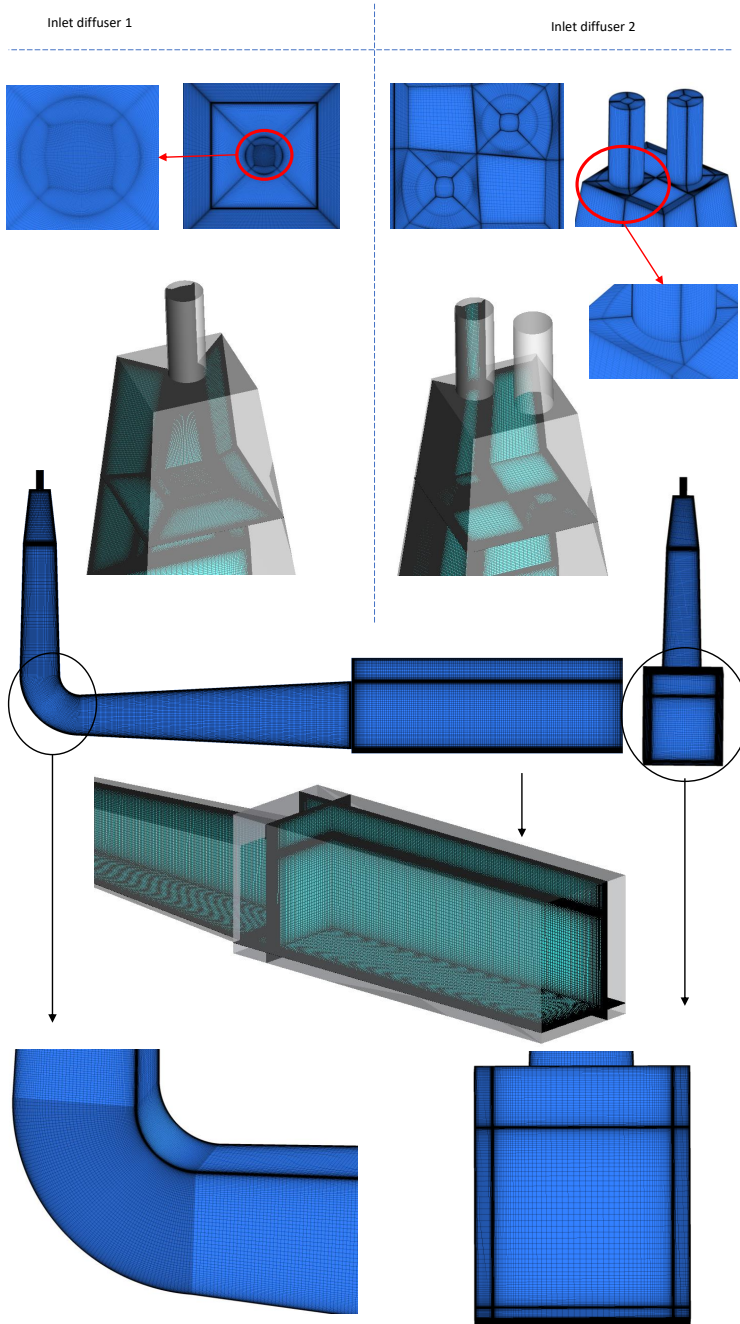


Figure 4.4: Mesh for the turbulent flow cases.

4.3 Solver settings

The setup for the solver is the next step in preparing the run of the simulation. The setup is slightly different for the laminar and the turbulent cases because the laminar cases does not require any turbulence modelling.

Initially the analysis type is set to steady state. The fluid domain is defined as water at $19^{\circ}C$ with a reference pressure of zero and an absolute pressure of 1 atm, 101325 Pa, specified at the outlet of the domain. The heat transfer option is set to isothermal. The turbulence model selected for the turbulent cases is the SST with automatic wall functions and no turbulence model is used in the laminar cases. Further, the boundaries are specified as follows: The walls are modelled as no-slip walls. The inlet is defined by the mass flow rate and the total mass flow rate in the turbulent low flow cases was 0.998 kg/s and the high flow cases was 3.992 kg/s. The mass flow rate in the laminar cases was 0.3537 kg/s. For the second geometry with two inlets the flow is in all cases equal through both inlets. The turbulence intensity is assumed to be medium (5%) in the turbulent flow cases. For the outlet, the boundary type "opening" is used in order to capture any flow patterns where water is flowing back into the domain in the outlet region. This outlet boundary is set to have atmospheric pressure.

In the solver control the advection scheme as well as the turbulence numerics is set to high resolution. The minimum number of iterations is 500 and the maximum is 2000. For the residual calculations RMS is chosen and the convergence criteria is $1e-05$. For the time scale control the auto time scale and conservative length scale control is chosen. Additionally, it was experienced that the solver run into a problem due to the large difference in velocity at the inlet and the outlet of the domain. This resulted in a very large correction after the first iteration, which stopped the solver. The following time scale factor expression was used to correct this issue. Here, the timescale factor is slowly increased from 0.01 to 2 in the first 1000 iterations and kept at 2 for the rest of the calculation.

$$\text{if}(\text{CurrentIterationNumber} < 1000, 0.01 + (\text{CurrentIterationNumber}/1000) * 1.99, 2)$$

The settings used in this analysis are summarized in Table 4.3.

Parameter	Description
Analysis type	RANS, steady state.
Boundary conditions	Mass flow defined inlet, static pressure outlet and no-slip walls.
Turbulence	Share stress transport, SST, with 5% turbulence intensity at the inlet for turbulent flow cases and none for laminar flow cases.
Convergence criteria	RMS of continuity, momentum, pressure and turbulence quantities $\leq 1e-05$.
Mesh elements	Laminar, one inlet: 3 021 509 Laminar, two inlets: 3 099 417 Turbulent, one inlet: 20 085 197 Turbulent, two inlets: 20 233 918
Mesh type	Hexahedral, structured
y^+ -values	For flow rate 1 L/s: Ranging between 0.0002 to 13 in the entire domain for the single inlet geometry and 0.0001 to 11 in the double inlet geometry. Overall average is 0.37 for the single inlet geometry and 0.36 for the double inlet geometry. For flow rate 4 L/s: Ranging between 0.0008 to 34 in the entire domain for the single inlet geometry and 0.0013 to 29 in the double inlet geometry. Overall average is 1.25 for the single inlet geometry and 1.37 for the double inlet geometry. Only applicable to turbulent flow cases.
Iterations per run	2 000
Physical timescale	Iteration dependent with values ranging from 0.01 to 2, linear.
Discretization	Advection scheme: High resolution Turbulence numeric: High resolution
Run type	MPI parallel

Table 4.3: Summary of the solver setup and mesh description for the solution of the flow problem in ANSYS CFX.

Chapter 5

Results and discussion

In this chapter the main findings of the thesis in terms of numerical results are presented. A discussion identifying strengths and weaknesses with the proposed setup based on the numerical results, provides useful information when performing future experiments on the test rig.

In section 5.1 results from the numerical calculations are presented. Section 5.2 evaluates how the flow field behaves by comparing the numerical results to the expected behaviour from early estimates, and how these findings are impacting the experiment. Finally, the ultrasound design and expected degassing effect is evaluated in section 5.3. Whether the setup is successfully testing the degassing from ultrasound is discussed.

5.1 Numerical results

Numerical simulations is the tool used for evaluating the properties of the suggested setup. This section is summarizing the findings from the numerical calculations by presenting the flow fields. The laminar case with flow rate 0.35 L/s, and the turbulent flow cases with 1 L/s and 4 L/s are presented in Figures 5.1, 5.2 and 5.3 respectively. Additionally, the estimated loss in the geometries from the numerical calculations is compared to the previous estimates of the losses in the system.

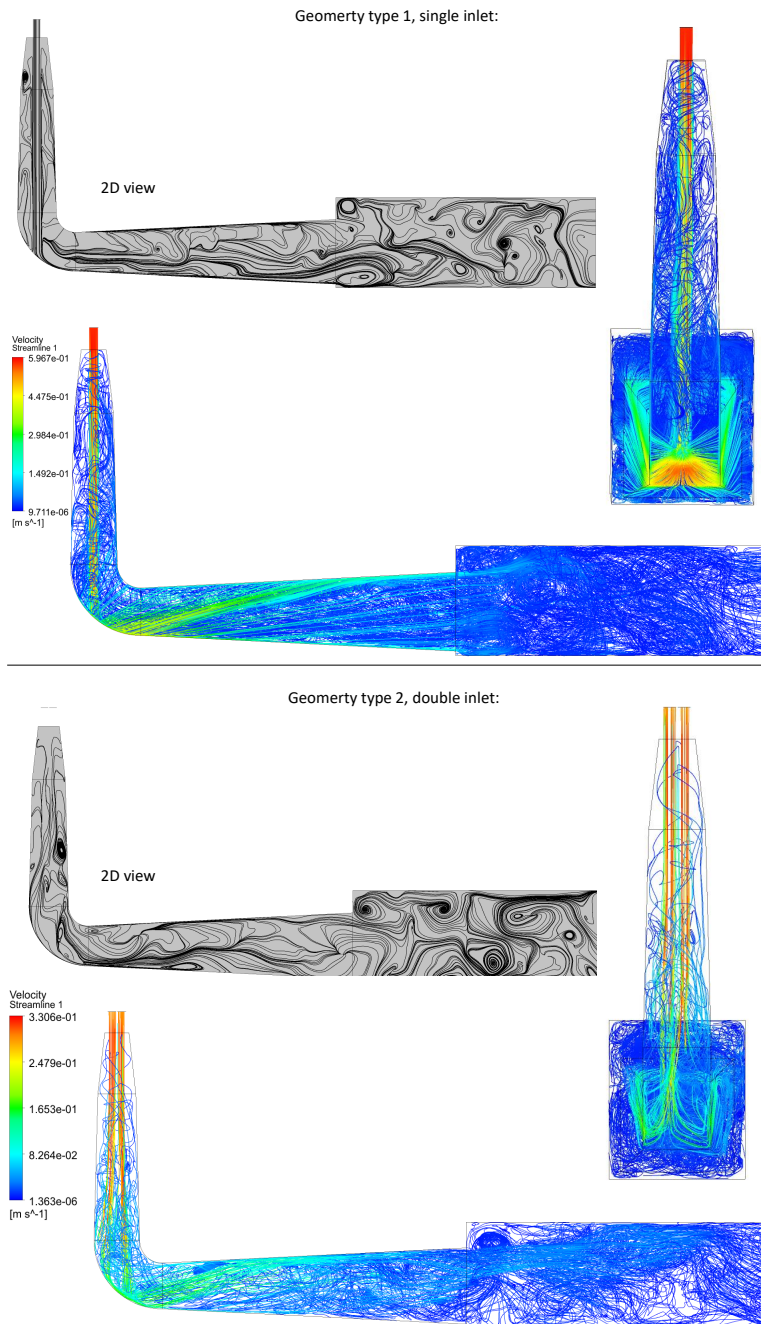


Figure 5.1: Streamlines for the laminar flow case with flow rate of 0.35 L/s. 3D-views of the flow are in colours and a 2D cross-section is given without colours for the two inlet designs.

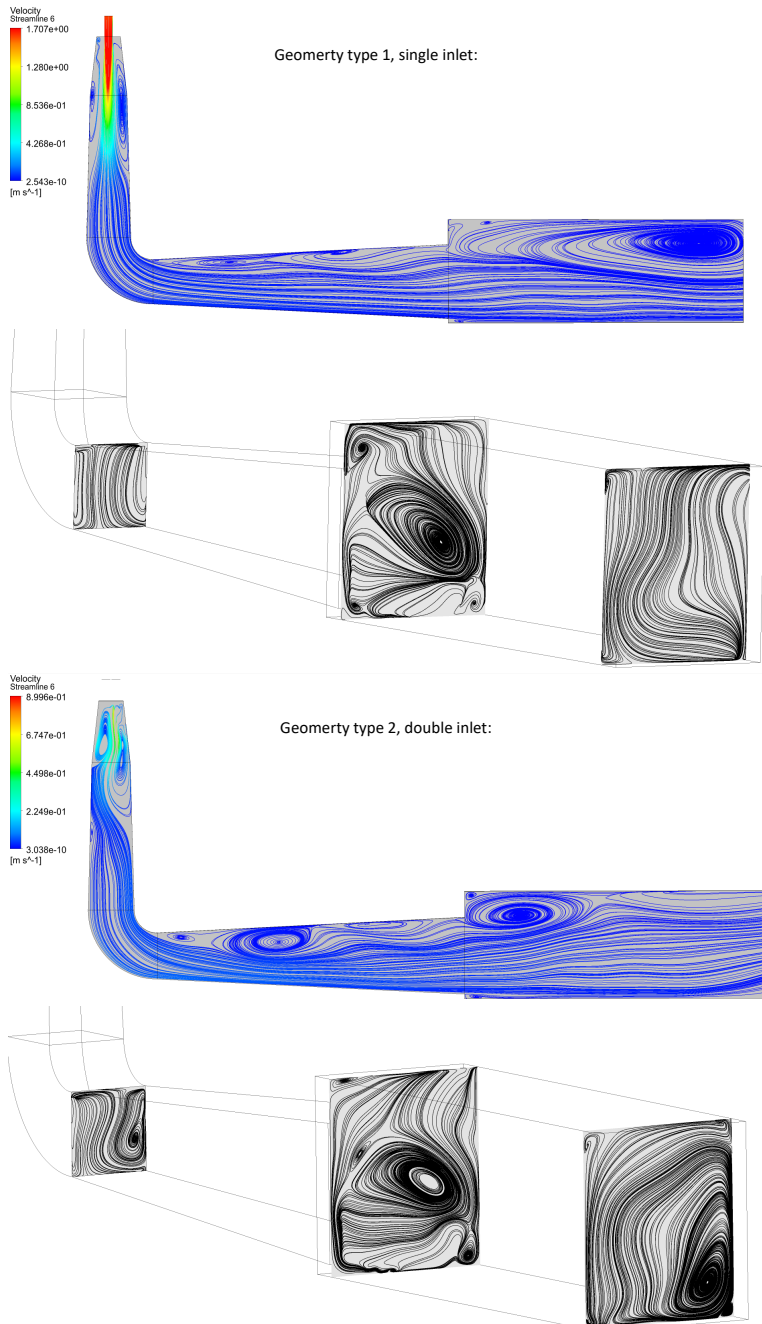


Figure 5.2: Streamlines for the turbulent flow case with flow rate of 1 L/s. 2D cross-sections of the flow are given on the mid-plane of the rig and on three planes perpendicular to the mean flow. At the outlet of the bend, inlet and of the flume and 1 meter into the flume for the two inlet designs.

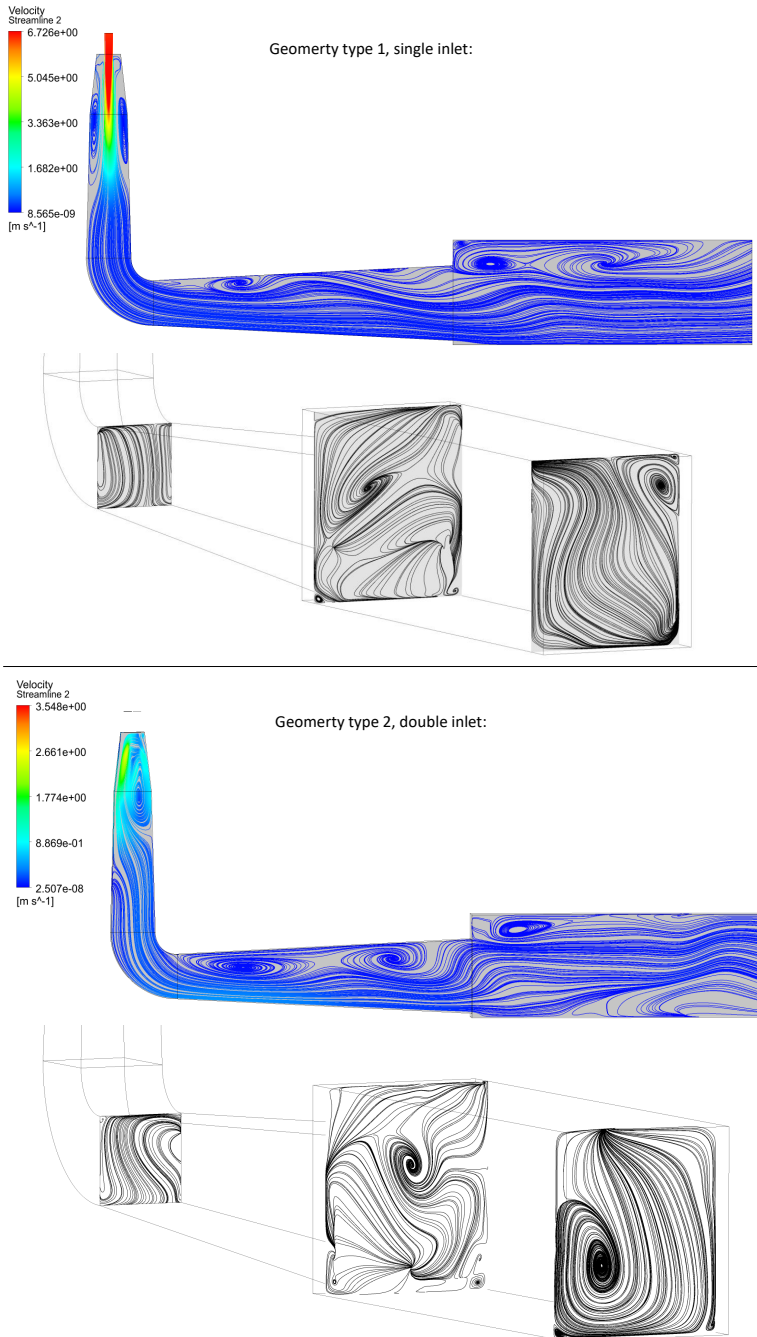


Figure 5.3: Streamlines for the turbulent flow case with flow rate of 4 L/s. 2D cross-sections of the flow are given on the mid-plane of the rig and on three planes perpendicular to the mean flow. At the outlet of the bend, inlet of the flume, and 1 meter into the flume for the two inlet designs.

The losses in the rig has been calculated for a single-inlet case. This is done by adding the flow losses from the sudden expansion at the rig inlet and the flume inlet, diffuser losses in the inlet diffuser, pre-, and post-bend diffuser and the bend. Additionally, the mass flow averaged values of the total pressure is used on the CFD-calculation results to calculate the total pressure loss in the system geometry from inlet to outlet. These calculations are presented in Table 5.1.

Flow rate [L/s]	Early estimate loss [m]	CFD one inlet [m]	CFD two inlets [m]
0.35	0.005	0.018	0.005
1	0.042	0.138	0.032
4	0.662	2.147	0.500

Table 5.1: Loss calculation from early estimates compared to obtained loss form CFD-calculations.

To obtain a rough estimate of the expected flume loss, the pressure loss in the second half of the flume is calculated by the change in the mass flow average of the total pressure from the middle of the flume to the flume outlet. This number is multiplied with 35 to obtain an estimated pressure loss for the total length of the flume of 17,5 meters. For a flow rate of 4 L/s and a single inlet this calculation estimates a total loss of 1.6 mm in the flume. This estimate is conservative as the loss due to the upper wall in the simulation is not present in the actual setup, and the flow in the flume inlet section is more disturbed compared to the flow downstream. Although, the small total loss obtained from this conservative estimate favours the decision of neglecting the flume loss in the previous calculations.

5.2 Flow field evaluation

The laminar flow cases presented in Figure 5.1 show a slow flow pattern where the inlet jets are maintained for a long time through the setup. Although the jets look rapid, the velocity is small, in the order of 0,6 m/s at the largest. The flow is characterized with small, slow vortexes moving through both geometries. Although there are swirls multiple places in the setup the flow is attached in the entire flow geometry. The convergence level of these simulations was in the order of $1e-03$, meaning that the location of the swirling flow structures can be moving to different locations in the geometry. The convergence history for all simulations are found in the Appendix.

In Figure 5.2 the 1 L/s flow simulations are presented. The flow is characterized with streamlines mostly in the mean flow direction and appears more orderly compared to the swirly laminar flow case. The flow fields show separation zones at the inlet diffuser as expected in the design procedure. The flow reattaches before the bend. For the single-inlet case, through the bend a secondary flow has occurred and can be seen in the cut-view at the outlet of the bend. At the flume inlet, larger circulation zones occur from the sudden expansion, although the flow is relatively well attached at the outlet of the post-bend diffuser. In the flume a large vortex is developing close to the outlet. This vortex occurs due to the configuration with a closed conduit in this region and will not be present

in an open flume, although the surface structure here is uncertain. For the double-inlet case the flow reattaches quicker before the bend, but has an asymmetric structure through the bend and larger separation zones in the post-bend diffuser.

For the 4 L/s flow simulations, presented in Figure 5.3, the flow is similar to the smaller flow rate turbulent case, but the recirculation zones observed in the previous case has grown in size. The inlet flow reattaches before the bend also in this case, but larger separation is observed in the post-bend diffuser. Additionally, the flow field is more exposed to separation and an asymmetric pattern in the double-inlet geometry has occurred. This is due to the asymmetric location of the inlet pipes, diagonally placed on the inlet diffuser. This phenomenon is not favourable as the flow in the flume is assumed to be more disturbed in this case. The asymmetry can also be observed in the cut-view at the bend outlet, as the secondary flow pattern is shifted compared to the single-inlet case. For all turbulent flow rate cases the convergence was in the order of $1e-04$, which are well converged solutions.

The results presented indicate a similarity in the flow fields for the turbulent flow cases. The cut-views through the midpoint of the rig show relatively straight streamlines and recirculation zones which are limited in size in the post-bend diffuser. The size of these zones is increasing with increasing flow rate and is larger for the double-inlet geometry. Due to the simplification of the flume to be modelled as a closed conduit it is uncertain how this separation will propagate downstream, but it is assumed that the flow will stabilize quickly after entering the flume due to the low flow velocity in this area. Additionally, the length to width ratio of the flume is large and will stabilize the surface. The risk of an overflow at the outlet due to the sudden expansion is present for high flow rates. Although, if this happens the V-shaped weir plate can be lowered to avoid an overflow at the flume inlet. If this is done it is important to always keep the ultrasound probe and transducer submerged and assure that the requirements for the flow upstream the weir plate are fulfilled according to the ISO1438 standard [47].

Due to the simplifications of the flow field in the flume made in the CFD-calculations, the results in this region will not be similar to the actual resulting flow in the flume inlet. For high flow rate cases the flow area in the flume will be larger compared to lower flow rates as the weir plate is lifting the surface when the flow rate increases. Also, the additional wall surface at the top of the flume is adding shear stresses to the flow which will not be present in the actual setup. Hence, the velocity at the top surface will not be zero. If the surface of the water proves to be unsteady and surface waves are disturbing the flow measurement, flow straighteners can be applied in the flume. By inserting a grid in the flume cross-section, the surface will be more stable. Although, this installation will impact the degassing preventing a comparison with experiments conducted without the flow straightening grid and different flow rates.

The general observation for the flow patterns with the double-inlet geometry is that the flow is more attached before the bend, and the recirculation zone in this area is smaller. The losses in the system calculated in Table 5.1 reflect this pattern by the large losses in the single-inlet geometry compared to the double-inlet geometry. The difference in flow loss occurs from the inlet recirculation zone which is smaller for the double-inlet. The estimated flow loss with simple equations is an applicable approximation for the double-

inlet geometry but fails to predict the loss in this area for the single inlet.

The degassing in the setup is of importance when discussing the properties of the setup design. The two sudden expansions in the setup are weak points for the flow field as they induce recirculation zones and swirls in the flow. The actual degassing effect of these flow structures is unknown. Although, the large difference in flow loss for the single-inlet and the double-inlet geometries raises a suspicion that the degassing effect in the recirculation zone at the rig inlet is different for the two geometries. This uncertainty can be controlled by always comparing the degassing with ultrasound to the degassing without ultrasound for all tested flow rate and geometry combinations. This will determine whether the experiments are comparable in terms of degassing due to the flow geometry. Observing whether the change from a laminar to a turbulent flow regime changes the degassing from the geometry is also interesting to investigate.

5.3 Ultrasound and the degassing effect

The residence time, the average time a particle of water is exposed to the ultrasonic field t_{res} , is changing with the flow rate. This is calculated by the time required for water to move over the ultrasound probe length in the post-bend diffuser and is presented in Figure 5.4. The calculation is provided in the attached MATLAB script in the Appendix.

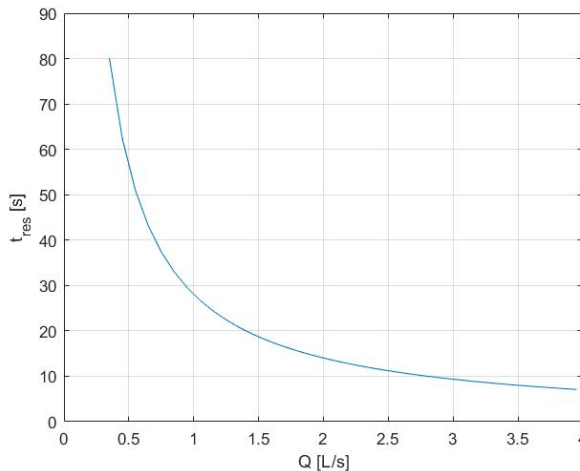


Figure 5.4: Residence time, t_{res} , for the water flowing over the ultrasound probe at different flow rates, Q , from 0.35 to 4 L/s.

The residence time is considerably large for flow rates of 1 L/s and lower, compared to higher flow rates. This range of flow rates is therefore favourable for initial experiments for validating whether degassing of flowing water can be effective. The maximum estimated power from the ultrasound probe is 1200 W rms, and emits an energy of 300 J/L at 4 L/s

and 2400 J/L at flow rate 0.5 L/s. It was shown in the project thesis that the degassing was highly dependent on the ultrasonic power level [1]. Hence, the degassing effect is expected to be considerably larger at low flow rates. Using this setup for identifying the required energy consumption per litre of sufficiently degassed water is a highly relevant research question.

To simplify the analysis of the flow pattern in CFD-calculations, the ultrasound transducer and probe were not modelled in the flow geometry. This choice results in an uncertainty of how the flow will behave in this region. However, the ultrasound equipment is displacing a volume for water in the bend and post-bend diffuser equivalent to the volume of the transducer, and hence, decreases the effective flow area. This will result in an acceleration of the flow through the bend section compared to a flow without the equipment installed. This can contribute to a more attached flow in the post-bend diffuser, as the acceleration contributes to less separation here. Although the size of the ultrasound equipment can be an advantage for the flow pattern presented in this setup, a similar prototype will cause large impacts on a hydropower plant's efficiency. Therefore, in a prototype the solution for the ultrasound equipment will be different and less intrusive in the flow system. Development of this equipment will therefore be an important part of a design process of a prototype solution.

When operating the ultrasound transducer at different power amplitudes the amount of produced heat will increase with increasing power. As the water in the rig is used for cooling the ultrasound equipment and temperature is affecting the degassing process, the temperature increase in the water must be monitored carefully. This becomes especially important at low flow rates and high power level where the residence time is long and heat production is high.

Conclusion

This thesis presents the geometry of a suggested experiment setup for degassing flowing, supersaturated water by employing ultrasound. Two main solutions for producing supersaturated water with air are presented along with specifications for the ultrasound equipment, measurement instrumentation and a suggested experiment procedure. The design is validated by performing a numerical calculation on the flow field. Strengths and weaknesses of the setup are pointed out and it is concluded with the following.

The flow field in the experiment setup is similar to the expected flow by design. For the turbulent flow cases, numerical calculations predict separation in the post-bend diffuser at high flow rates and this is especially apparent for the double-inlet diffuser. It is expected that this separation will be less prominent when the ultrasound equipment is installed in the test rig, and all evaluated flow rates are well suited for performing experiments in the suggested setup individually.

The analysis has identified the following challenges. The sudden expansions in the inlet diffuser and inlet to the flume create recirculation zones of different sizes depending on flow rate. It has been established that the flow losses in the inlet recirculation zone is large for the single-inlet geometry compared to the double-inlet geometry. Whether the degassing processes at different flow rates are comparable must be evaluated by comparing the degassing without ultrasound at different flow rates. Additionally, the ultrasound transducer is cooled by the water in the rig and the water temperature is expected to increase during experiments. Especially at low flow rates and high ultrasound power levels the temperature increase must be monitored carefully.

The setup is allowing for experiments on a large range of residence times and ultrasound power levels with flexibility in implementation. Hence, the setup fulfill the design criterion presented by allowing for monitoring the degassing of a controlled flow of supersaturated water by employing ultrasound.

Further work

In this thesis a suggested experiment setup for degassing flowing, supersaturated water has been presented. The final goal of the project is obtaining a prototype for degassing supersaturated water from hydropower plants by employing ultrasound. The next steps on this road are described in the following.

The development of the experiment setup is to be completed by implementing a solution for producing supersaturated water and obtaining a controlled flow rate through the setup. This is initiated by designing and installing a cone for producing supersaturated water based on the presented solution from the aquaculture industry or a solution with a fixed volume produced in the pressure tank. Testing the use of a pump to fill the pressure tank for a constant tank level is lowering the experiment uncertainty and is the preferred solution.

The measurement equipment must be calibrated and mounted on the rig, and a system for logging the measurements should be made to streamline the experiment procedure.

Installing the ultrasound equipment in the setup by mounting it in the bend. Further, testing the equipment by measuring the increase in temperature at different power levels and flow rates and verifying that the flow over the equipment is as expected.

When experiments can begin the following search questions are of interest. Using the setup for identifying the required energy consumption per litre of sufficiently degassed water is a highly relevant research question. This can be a starting point in the process of scaling up the degassing system to a prototype size. Also, investigating the residence times required for proper degassing of the water is of interest for evaluation of whether the solution of degassing with ultrasound is a practically and economically relevant solution.

Development of a less intrusive ultrasound transducer and probe system, which can be applied in a hydropower system without disturbing the flow, is an important part of further development on this research area.

Bibliography

- [1] M. Rognerud, *How to Avoid Gas Supersaturation in Rivers Downstream Hydropower Plants*. NTNU, 2019.
- [2] NVE, “Vannkraft.” <https://www.nve.no/energiforsyning/vannkraft/?ref=mainmenu>, 2019. Online; Accessed 11.10.19.
- [3] EnergiNorge, “Norsk vannkraft- kilden til fornybarsamfunnet.” <http://kunder.spire.as/norskvannkraft/>, 2014. Online; Accessed 10.10.19.
- [4] W. L. Ebel and H. L. Raymond, “Effect of Atmospheric Gas Supersaturation on Salmon and Steelhead Trout of the Snake and Columbia Rivers,” *MFR*, 1976.
- [5] T. Tekle, *Overmetning av oppløst luft i vann fra kraftverk- årsaksforhold, skadevirkninger og mottiltak*. Norges hydrodynamiske laboratorier, 1983.
- [6] G. R. Bouck, “Etiology of Gas Bubble Disease,” *Transactions of the American Fisheries Society*, vol. 109, pp. 703–707, 1980.
- [7] D. G. Eskin, “Ultrasonic Degassing of Liquids,” *Power Ultrasonics: Applications of High-Intensity Ultrasound*, pp. 611–631, 2015.
- [8] O. Guttormsen, *Vassdragsteknikk II*. Akademika, 2016.
- [9] Y. A. Cengel and J. M. Cimbala, *Fluid Mechanics, Fundamentals and Applications*. Mc Graw Hill Education, 2014.
- [10] S. L. Dixon and C. A. Hall, *Fluid Mechanics and Thermodynamics of Turbomachinery*. Elsevier, 2014.
- [11] Haas, R. and Hiebert, M. and Hoatson, E., “Francis Turbines - Fundamentals and Everything Else You Didn’t Know That You Wanted To Know.” <https://docplayer.net/31850733-Francis-turbines-fundamentals-and-everything-else-you-didn-t-know.html>, 2014. Online; Accessed 25.02.20.

-
- [12] H. Brekke, *Introduction to Hydraulic Machinery*. NTNU, 2000.
- [13] A. Zobeiri, “Investigations of time dependent phenomena in a turbine and a pump-turbine of francis type: rotor-stator interactions and precessing vortex rope. phd thesis.” <https://infoscience.ep.ch/record/128887>, 2009. Online; Accessed 09.03.20.
- [14] A. Nordvik, I. Iliev, C. Trivedi, and O. G. Dahlhaug, “Numerical prediction of hill charts of Francis turbines,” *Journal of Physics*, vol. 1266, 2019.
- [15] IEC, *Hydraulic turbines, storage pumps and pump-turbines - Model acceptance tests*. IEC, 2019.
- [16] Norwegian Hydropower Center (NVKS), “Francis 99, First workshop.” <https://www.ntnu.edu/nvks/f99-publication1>, 2014. Online; Accessed 14.05.20.
- [17] A. Kjølle, *Hydraulisk måleteknikk, Grunnleggende prinsipper og målemetoder*. NTNU, 2003.
- [18] H. Brekke, *Pumper og turbiner*. NTNU, 2003.
- [19] V. Chandavari and S. Palekar, “Diffuser angle control to avoid flow separation,” *International Journal of Technical Research and Applications*, vol. 2, pp. 16–21, 2014.
- [20] E. Mosony, *Low Head Power Plants, ch. 52. Fundamental Principles of Draft-Tube Design*. Akademiai Kiado, 1987.
- [21] J. Colt, *Dissolved Gas Concentration in Water, Computation as Functions of Temperature, Salinity and Pressure*. Elsevier, 2012.
- [22] U. Plug, T. E. Isaksen, G. Velle, S. Stranzl, E. O. Espedal, K. W. Vollset, E. Bye-Ingebrigtsen, and B. T. Barlaup, “Gassovermetning i vassdrag- En kunnskapsoppsummering ,” tech. rep., NORCE LFI, 2018.
- [23] U. Plug, K. W. Vollset, G. Velle, and S. Stranzl, “First observations of saturopeaking: Characteristics and implications,” *Science of the Total Environment*, vol. 573, pp. 1615–1621, 2016.
- [24] A. Berg, “Air entrainment and supersaturation of dissolved air in a shaft under atmospheric and reduced pressure conditions,” *Journal of Hydraulic Research*, vol. 30:3, pp. 327–340, 1992.
- [25] J. D. DeCoste and S. S. Zumdahl, *Chemical Principles*. Mary Finch, 2013.
- [26] K. Yasui, *Acoustic Cavitation and Bubble Dynamics*. Springer Nature, 2018.
- [27] M. Legay, N. Gondrexon, S. Le Person, P. Boldo, and A. Bontemps, “Enhancement of Heat Transfer by Ultrasound: Review and Recent Advances,” *International Journal of Chemical Engineering*, vol. 2011, 2011.

-
- [28] M. H. Islam, B. G. Pollet, and O. Burheim, "Sonochemical and sonoelectrochemical production of hydrogen," *Ultrasonics Sonochemistry*, vol. 51, pp. 533–555, 2019.
- [29] M. R. Kasaai, "Input power-mechanism relationship for ultrasonic irradiation: Food and polymer applications," *Natural Science*, vol. 5, pp. 14–22, 2013.
- [30] M. Ashokkumar, *Handbook of Ultrasonics and Sonochemistry*. Springer Science, 2016.
- [31] L. M. Ingebrigtsen, *Effects of Ultrasonic Frequency, Acoustic Power, and Liquid Height on Radical Production in a Sonochemical Reactor*. NTNU, 2019.
- [32] A. Brotchie, F. Grieser, and M. Ashokkumar, "Effect of Power and Frequency on Bubble-Size Distributions in Acoustic Cavitation," *Physical Review Letters*, vol. 102, 2009.
- [33] T. Leong, M. Ashokkumar, and S. Kentish, "The fundamentals of power ultrasound—a review," 2011.
- [34] O. Lindstrøm, "Physico-Chemical Aspects of Chemically Active Ultrasonic Cavitation in Aqueous Solutions," *The Journal of the Acoustical Society of America*, vol. 27, p. 654, 1955.
- [35] N. A. Pelekasis and J. A. Tsamopoulos, "Bjerknes forces between two bubbles. Part 1. Response to a step change in pressure," *Journal of Fluid Mechanics, Cambridge University Press*, vol. 254, pp. 467–499, 2006.
- [36] J. P. Franc, "The Rayleigh-Plesset equation: a simple and powerful tool to understand various aspects of cavitation.," *Fluid Dynamics of Cavitation and Cavitating Turbopumps*, pp. 1–43, 2007.
- [37] M. S. Plesset and A. Prosperetti, "Bubble Dynamics and Cavitation," *Fluid Mechanics*, vol. 9, pp. 85–145, 1977.
- [38] M. S. Plesset, "The Dynamics of Cavitation Bubbles," *Journal of Applied Mechanics*, vol. 70, pp. 277–282, 1949.
- [39] P. J. Zwart, A. G. Gerber, and T. Belamri, "A Two-Phase Flow Model for Predicting Cavitation Dynamics," *International Conference on Multiphase Flow*, vol. 152, 2004.
- [40] B. Ji, J. Wang, X. Luo, K. Miyagawa, L. Z. Xiao, X. Long, and Y. Tsujimoto, "Numerical simulation of cavitation surge and vortical flows in a diffuser with swirling flow†," *Journal of Mechanical Science and Technology*, vol. 30, pp. 2507–2514, 2016.
- [41] H. Alehossein and Z. Qin, "Numerical analysis of Rayleigh–Plesset equation for cavitating water jets," *International Journal for Numerical Methods in Engineering*, vol. 72, pp. 780–807, 2007.
-

-
- [42] J. A. Gallego-Juarez and K. F. Graff, *Title: Power Ultrasonics : Applications of High-Intensity Ultrasound*. WOODHEAD PUBLISHING, 2015.
- [43] A. Mærleie, *PIV measurements in the vaneless space of a Francis turbin*. NTNU, 2019.
- [44] F. White, *Fluid Mechanics, 6th edition*. Mc Graw Hill, 2008.
- [45] H. Ito, “Pressure Losses in Smooth Pipe Bends,” *Journal of Basic Engineering*, pp. 131–143, 1960.
- [46] P. Runstadler, *Diffuser Data Book*. Creare Inc Tec. Note 186, 1975.
- [47] ISO1438, *Hydrometry — Open channel flow measurement using thin-plate weirs*. Standards Norway, 2017.
- [48] H. J. C. Berendsen, *A Student’s Guide to Data and Error Analysis*. Cambridge University Press, 2011.
- [49] H. K. Versteeg and W. Malalasekera, *An Introduction to Computational Fluid Dynamics, 2nd ed*. Pearson Education Limited, 2007.
- [50] R. H. Pletcher, J. C. Tannehill, and D. A. Anderson, *Computational Fluid Mechanics and Heat Transfer, 3rd edition*. CRC Press, 2013.
- [51] ANSYS, *ANSYS CFX-Solver Theory Guide*. ANSYS Inc., 2011.
- [52] F. White, *Viscous Fluid Flow, 3rd ed*. McGraw-Hill, Inc., 2006.
- [53] LEAP Australia, “Computational fluid dynamics blog - leap australia.” <https://www.computationalfluidynamics.com.au/wp-content/uploads/2013/04/wallfunction.png>, 2020. Online; Accessed 01.05.20.
- [54] F. Menter, “Two-Equation Eddy-Viscosity Turbulence Models for Engineering Applications,” *AIAA Journal*, vol. 32, no. 8, pp. 1598–1605, 1994.
- [55] cfd online, “SST k-omega model.” https://www.cfd-online.com/Wiki/SST_k-omega_model, 2011. Online; Accessed 13.05.20.
- [56] Lindre Industrigasser Norge, “SOLVOX C oksygeneringskjegle.” https://www.linde-gas.no/no/products_ren/fish_farming_equipment/solvox_c/index.html, 2020. Online; Accessed 18.05.20.

Appendix

A.1 Paper for CRHT-X'20

The following paper was written in association with CRHT-X'20 symposium in Kathmandu, Nepal.

How to Avoid Total Dissolved Gas Supersaturation in Water from Hydropower Plants by Employing Ultrasound

Maren Elise Rognerud*, **Bjørn W. Solemslie**

Waterpower Laboratory, Department of Energy and Process Engineering, Norwegian University of Science and Technology, Trondheim, Norway

E-mail: marenrog@stud.ntnu.no

Md H. Islam, Bruno G. Pollet

Hydrogen Energy and Sonochemistry Research Group, Department of Energy and Process Engineering, Norwegian University of Science and Technology, Trondheim, Norway

Abstract. In Norway, more than 10 hydropower plants are known to have caused biologically relevant levels of total dissolved gas supersaturation in the rivers downstream power plants. This phenomenon is causing fish kills due to gas bubble disease and have large impacts on the biodiversity. The gas supersaturation is often caused by undersized or blocked brook intakes creating turbulent flows and resulting in large amounts of air dragged into the tunnel. One possible solution to this problem is employing power ultrasound (20 kHz - 1 MHz) for degassing water prior to releasing it back into the river system. Acoustic cavitation is known to have a positive effect on the degassing mechanism, and this paper is investigating whether ultrasound can be applied to create acoustic cavitation and avoid biologically relevant levels of total dissolved gas supersaturation from hydropower plants. The objective is to develop background knowledge for constructing an experimental setup in the Waterpower Laboratory at NTNU to investigate whether gas supersaturation can be decreased from power plants by application of ultrasound. Preliminary experiments, carried out at the NTNU Hydrogen Energy and Sonochemistry Laboratory, exploring the behaviour of the degassing process at different ultrasonic frequencies and amplitudes conclude that the most effective degassing occur at high acoustic amplitude and a frequency of 24 kHz.

1. Introduction

Hydropower is the most important resource for energy production in Norway as 94 % of the electricity production is based on hydroelectric power generation. Technological development has enabled power demanding industry and power system technology to evolve throughout the past 100 years [1]. During this century knowledge about hydropower systems has grown, and researcher's attention has been directed towards new challenges like preservation of environmental values and biodiversity. One of these more recent challenges is the issue of gas supersaturation in rivers and lakes downstream hydropower plants. This phenomenon was first observed downstream river power plants in the Colombia and Snake rivers in the 1960s [2]. In Norway suspicion that supersaturated water from power plants could cause fish kills were raised in 1972 when dead fish were observed downstream Matre power plant in Masfjorden [3].

Gas supersaturation occur if the amount of dissolved air in water is higher than the solubility threshold at a given ambient pressure and temperature. Supersaturated water can occur in hydropower plants when pressurized water with high concentration of dissolved gas is exposed to atmospheric pressure in the downstream river or lake. Air is usually entering the water system through the brook intakes [4]. The intakes are designed to avoid air from entering the system, although, undersized intakes and flood situations with high water levels cause turbulent flows around the intakes and results in air transportation into the tunnel system. When this phenomenon appear, fish and other aquatic species die from gas bubble disease if the supersaturation levels are high over a longer period of time [3, 5]. The supersaturated water is degassing slowly, especially in deep and calm rivers or lakes. This results in supersaturated water being transported for tens of kilometres downstream the power plant and affecting biodiversity in vast areas of the water system [3].

One possible solution to the challenge of minimizing emission of supersaturated water from hydropower plants, is by using ultrasound to enhance the degassing process. Utilizing ultrasound for degassing has been used widely in the food industry to improve quality and durability of food products, and in material technology to ensure better quality of metal, glass and other products. When ultrasound is applied to supersaturated water, the rarefaction induces cavitation bubbles that can contribute to accelerate the degassing mechanism [6]. Performing a literature review on acoustic cavitation creates a foundation of knowledge to perform experiments with degassing water with ultrasound, further, the hypothesis is tested by applying ultrasound to small amounts of oxygen saturated water and measuring the decay of dissolved oxygen over time.

2. Theory

The solubility of air in water increase with increasing pressure and decreasing temperature[7]. When the water is undersaturated air is slowly dissolving in the water, and conversely, when the water is supersaturated air is transported from the water[3]. This degassing mechanism can be enhanced by applying ultrasound to supersaturated water, and the background theory explaining this phenomenon is given in the following section.

2.1. Ultrasound

Ultrasound is acoustic waves with frequencies above the human hearing range i.e. above 10 kHz [8]. One way to classify ultrasound is according to frequency and power. Ultrasound with frequencies above 1 MHz is defined as low power ultrasound and is transmitting low levels of power with high frequencies. This type of ultrasound usually has an acoustic power of less than 10 W and is not affecting the medium of propagation. Therefore, it can be used for medical imaging and diagnostics [9]. Ultrasound with low frequencies, between 20 kHz and 1 MHz, is power ultrasound. These acoustic waves are transferred through a medium with power larger than 10 W, and the acoustic waves are altering the medium of propagation. This range of ultrasonic frequencies is used in sonochemistry where sound waves are introduced to produce chemical reactions in the medium of propagation, for instance to produce hydrogen from water [10].

An acoustic wave can be described mathematically with Equation 1.

$$P = P_a \sin(2\pi ft) [Pa] \tag{1}$$

P_a is the maximum pressure amplitude, f is the frequency and t is time [11]. The maximum pressure amplitude is directly proportional to the input power from the transducer. One important measure used for ultrasound is the ultrasonic intensity, I , defined as follows.

$$I = \frac{P_a^2}{2\rho a} [W/m^2] \quad (2)$$

ρ is the density and a is the speed of sound in the medium. The intensity is defined as the average rate of flow of energy through a unit area normal to the direction of propagation [8].

2.2. Acoustic Cavitation

Ultrasonic waves are pressure pulsations moving through a medium like illustrated in Figure 1. If the rarefaction pressure is below the vapour pressure for water, small bubbles of water vapor starts to form in the liquid. The rarefaction is followed by a compression phase where the pressure no longer can sustain the water vapour, resulting in a violent collapse of the bubble. This collapse launch shock waves into the water that can increase temperatures to about 5000 °C and pressure to 2000 atm at this point [10]. The bubble implosion can induce light emission (sonoluminescence) and chemical reactions where highly reactive radicals are produced (sonochemistry) [12]. If the bubble collapse happens close to a solid wall, the bubble implodes in a nonlinear manner and creates a jet with speeds up to 200 m/s directed towards the solid surface [10]. The forces induced by the collapse have erosive effects on the wall [8]. The process of bubble formation, growth and collapse due to changes in acoustic pressure is called acoustic cavitation. Acoustic cavitation is comparable to boiling, with two major differences. First, boiling is a result of increased temperature in a liquid, not a pressure decrease. Secondly, in boiling the bubble collapse is not present [8].

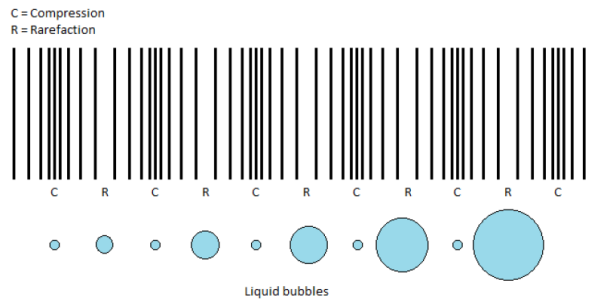


Figure 1. Ultrasonic pressure wave propagation and growth of a cavitation bubble during some cycles of ultrasound [13].

2.3. Other Phenomena Introduced by Ultrasound

In an ideal system with a fluid exposed to an ultrasonic wave, one parcel of fluid is moving back and forth to the same place with the ultrasonic pressure pulsation. However, in a real fluid the parcel will not move in this manner, and the position will change over time. This phenomenon is called acoustic streaming and results in a direct current flow in the wave propagation direction. This motion can be explained by the fact that the pushing of a viscous fluid along the direction of the acoustic wave is stronger than the pulling of it due to the moment of inertia of the fluid. This creates motion in the liquid. Acoustic micro-streaming is a phenomenon that occurs when the length scale of streaming caused by viscous stress near an object or wall is smaller than the acoustic wavelength [8].

[14] studied the effect of ultrasonic frequency and power on the bubble size of cavitation bubbles. Looking at bubble size for frequencies from 20 kHz to 1136 kHz it was shown that the bubble size decreased considerably with increasing frequency and increased with increasing power. Also, the study concluded that the difference in bubble size was larger for lower frequencies and higher power. To understand this phenomenon one can look at the mechanism of bubble collapse in an ultrasonic field. When a cavitation bubble is created it is vibrating with a natural frequency much higher than the ultrasonic frequency. The bubble starts growing and when the surface area becomes larger, the natural vibration frequency decreases. This process will continue until the oscillation frequency of the bubble equals the frequency of the ultrasonic field. When this happens, the bubble collapses [15]. At high frequencies, the maximum bubble size is therefore limited to a smaller size compared to lower frequencies.

[11] investigated the effect of ultrasonic power on the propagation medium. It was found that low frequencies produce high temperatures due to energy dissipation from high power ultrasound, cavitation and micro-streaming. For higher frequencies cavitation becomes less violent, and for frequencies in the MHz - range, only acoustic streaming is observed. The article concludes that the mode of action of ultrasonic waves changes as a function of input power. At low input powers no chemical or physical changes are detected, while at high power the medium changes chemically or physically. Additionally, [15] points out that bubble collapse is an almost adiabatic process where all energy is converted into heat. For low frequencies, the bubbles are larger and the energy discharge from the bubble collapse is stronger compared to smaller bubbles.

When a bubble collapses it produces highly reactive radicals due to the high temperature and pressure and fewer cavitation bubbles are introduced at low frequencies compared to higher frequencies. All together this means that the radical production which is attractive to achieve when doing sonochemistry will have a maximum when both bubble size and bubble numbers are large. For creating shear stress and movement in the solution on the other hand, frequencies lower than this are effective [15].

The theoretical cavitation threshold in water, the limit pressure where cavitation is initiated, is calculated by the pressure that is needed to overcome the tensile strength of pure water. Theoretically this limit is at about 1000 atm. Although, experiments show that the actual cavitation threshold is much lower than this limit. The reason for this phenomenon is that the cavity is more easily able to form around micro particles or bubbles that are already present in the water, so-called cavitation nuclei. In water small bubbles will always be present and the amount of bubbles will increase with the amount of dissolved air in the water [15]. [8] presents experimental results showing a decrease in cavitation threshold with increased dissolved air. This is evidence that the cavitation bubbles also contain air, not only water vapor. Therefore, cavitation bubbles can theoretically enhance the degassing process.

2.4. Degassing with Ultrasound

Ultrasound can have many effects on the medium of propagation. During the rarefaction phase acoustic cavitation occur if the rarefaction pressure is below the cavitation threshold pressure. When cavitation bubbles starts to form, they are pulsating and dissolved air is transported into the bubbles with diffusion [16]. When the pressure is high the bubble decrease in size and the gas diffuses from the bubble into the liquid. Conversely, when the pressure decreases, the bubbles expand, and gas diffuses from the liquid into the bubble. During the rarefaction the surface area is larger, and more gas can diffuse in through the bubble surface compared to the amount that escapes during the compression phase. This phenomenon is called the area effect on gas diffusion. Additionally, there is a resistance for molecules to move from a low density environment inside the bubble to a high density environment in the water phase. This effect is called the shell effect. Both the area effect and the shell effect is preventing air from leaving the bubble [15]. Hence, the bubble acts like a pump; for each expansion the bubble gain more

gas than it loses during the compression and is gradually filled with air. Therefore, the bubble manages to grow and after some time it floats to the surface driven by buoyancy forces. This process is called rectified diffusion. Additionally, microscopic acoustic streams are generated in the viscous boundary layers around the bubble surface and contribute to mass transfer that supplies the bubble with new liquid at the bubble surface. When the bubbles starts moving it creates convective flows in the liquid that contribute to increase the degassing efficiency because the bubbles are distributed around in the liquid [6]. The growth of a cavitation bubble during some cycles of ultrasound is described in Figure 1.

3. Experiment Setup

A small scale experimental setup was used to look at the degassing effect of different frequencies of ultrasound on 1.2 litres of oxygen saturated, distilled water. The water was pumped between two glass vessels at a flow rate of approximately 0.5 L/min. The first vessel had a cooling system and the ultrasonic transducers attached to it, and in the second vessel the measurements were taken. The measurements were separated from the ultrasonic transducer to avoid disturbances from the ultrasound. The two vessels are connected with silicon tubing to circulate the water between them. The silicon tubes should not be put in vicinity of the ultrasound. Therefore, glass pipes were used in the vessel with the ultrasonic transducer to circulate the solution and add oxygen to the water.

The probes used to measure pH, dissolved oxygen (DO) and electrical conductivity (EC) are Hanna Instruments Edge measurement probes. Three ultrasonic transducers were used to conduct experiments on ultrasonic degassing of oxygen from water. To produce the frequencies 580 kHz, 860 kHz and 1140 kHz, the Meinhardt Ultrasonics Multi-frequency System was used. A Meinhardt Ultrasonics Transducer was used for 40 kHz and the Hielscher UP400St was used for 24 kHz. The Multi-frequency system and the 40 kHz system use plate transducers while the Hielscher system uses a sonotrode.

The experimental procedure begun by filling the vessels with 1200 mL distilled water and the circulation pump was started. When the pH, EC and DO readings stabilized, oxygen was bubbled into the circulating solution at atmospheric pressure until it reached an oxygen saturation of about 19 mg/L. The oxygen bubbling was stopped, and the solution circulated until the saturation level stabilized and started to decrease. When the saturation level reached 18 mg/L the ultrasound was turned on, as well as the cooling system. The cooling system kept the solution at approximately 25°C. The transducer was on until the dissolved oxygen level decreased to its original level, about 7.8 mg/L. During this process the DO, pH and EC were logged once every minute, as well as the temperature. Each experiment was repeated three times to reduce the random experimental error and the presented results are the averaged values from the experiments.

4. Results and Discussion

The decay of dissolved oxygen for different frequencies is presented in Figure 2. The most effective degassing frequency was 24 kHz, therefore, different acoustic pressure amplitudes were tested for this frequency to look at the effect of acoustic intensity on the degassing effect. The results are shown in Figure 3. The change in pH and EC during the experiments is presented in Tables 1 and 2. Additionally the transferred energy from the transducer to the water was determined for the experiments on 24 kHz with calorimetry and the results are shown in Figure 4 [17, 18].

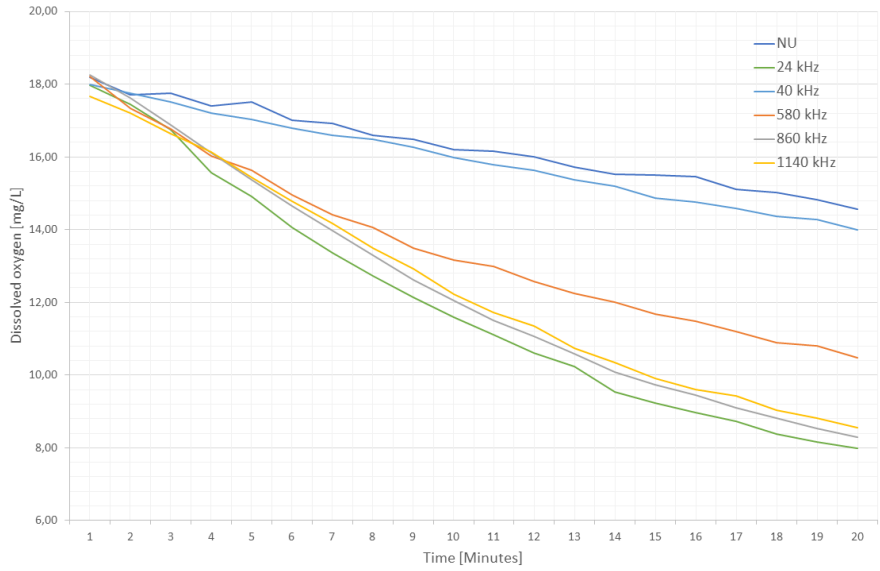


Figure 2. The decay of dissolved oxygen with time for ultrasonic frequencies 24 kHz, 40 kHz, 580 kHz, 860 kHz, 1140 kHz and no ultrasound (NU).

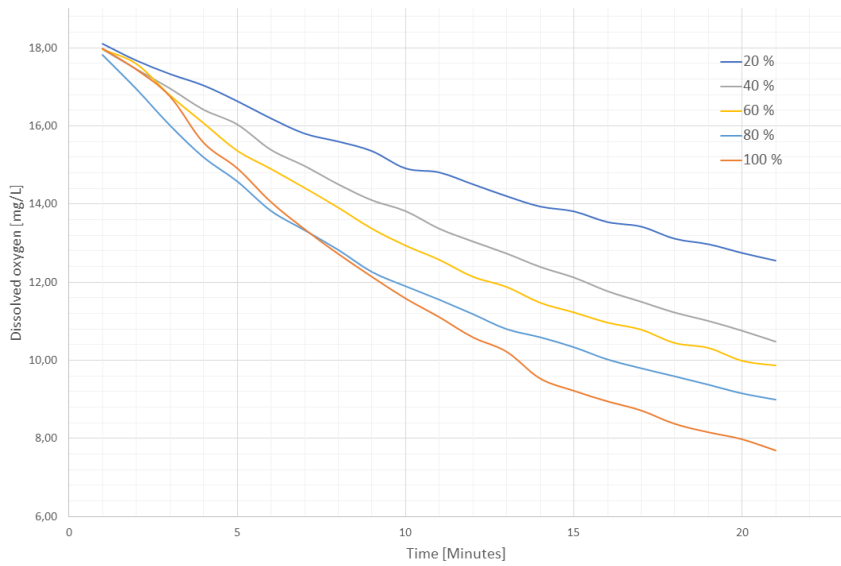


Figure 3. The decay of dissolved oxygen with time for ultrasonic frequency of 24 kHz and amplitudes 100 %, 80 %, 60 %, 40% and 20 %.

The explanation of this degassing behaviour is based on the provided theory. The effects that are increasing degassing efficiency are shear stresses created in the flow and thicker boundary layers around the bubbles. This increases the mass transfer of oxygen into the bubbles as micro-streaming is supplying the bubbles with high saturation levels of oxygen. A large bubble size allows each bubble to contain more oxygen that is transported out of the water when it floats to the surface. All these effects are dominating for low frequencies of ultrasound and can explain how 24 kHz can be the most effective degassing frequency.

For higher frequencies favourable effects that may increase the efficiency of degassing are the facts that a higher number of bubbles are created at higher frequencies and acoustic streaming is stronger and creates secondary flows inside the glass vessel. This leads to a larger amount of air inside bubbles in total, that is transported to the surface by the streaming effect. Although, if the frequency becomes too high the bubbles will collapse before they are transported to the surface and the degassing effect will be limited by this phenomenon. Therefore, the increase of acoustic frequency above 860 kHz is not increasing the degassing efficiency further.

In between the high frequencies and lower frequencies, the degassing effect is lower. When going from low to higher frequencies the bubble size decreases as well as acoustic micro-streaming decreases, lowering the degassing efficiency. While further increasing the frequency the number of bubbles increases as well as the acoustic streaming. Therefore, the degassing efficiency increases to a new maximum point until the more frequent early bubble collapse limits the amount of bubbles that can float to the surface. This can explain why frequencies of 40 kHz and 580 kHz are clearly less effective for degassing purposes.

When the experiments on frequency dependence were conducted, one acoustic frequency was chosen to experiment with amplitudes. 24 kHz was the most effective frequency for degassing but was very close to the 860 kHz degassing efficiency. [13] performed calorimetry experiments using the Multi-frequency transducer and the Heilcher sonotrode and found that the power transmitted to 250 mL water at 860 kHz was 34.5 % of the power transmitted at 24 kHz. These numbers are not directly comparable to the setup used in this experiment but shows that the energy usage is considerably larger for 24 kHz. Although, it was observed that the increase in pH was lower at 24 kHz, and the degassing efficiency was slightly better. Hence, 24 kHz was chosen.

The amplitude effect on degassing in Figure 3 shows that the higher acoustic pressure amplitude used, a more effective degassing was observed. When increasing the amplitude with 20 % steps the degassing efficiency increases almost linearly. This means that increasing the pressure amplitude, i.e. the acoustic intensity, improves the degassing efficiency at this frequency. With this in mind, another possible explanation of the poor degassing efficiency of 40 kHz is that the acoustic power transferred to the water using the 40 kHz plate transducer transmitted a significantly lower amount of acoustic power compared to the 24 kHz sonotrode, although this has not been proven in experiments. The degassing efficiency is highly dependent on the power and the ultrasonic intensity supplied to the water.

The water was saturated to 18 mg/L, corresponding to a 230 % saturation level at 25°C. The results in Figures 2 and 3 clearly show that the degassing efficiency is depending on the saturation level in water. The degassing slope is steeper for high saturation levels and flattens out when the saturation level is closer to the solubility limit. The explanation to this phenomenon is that the air content of the water supplied to the bubbles is lower at lower saturation levels. Therefore, the bubble growth is slower, and hence, the degassing is slower. This represents a challenge for using ultrasound for degassing in hydropower plants. The water in a hydropower plant is moving through an ultrasonic field and will only be exposed to the ultrasound for a short amount of time. If saturation levels are high, it might be possible to reduce the saturation level to some extent, but the exposure time will always be an issue. The question whether the degassing can be effective in these conditions is yet to be investigated.

Frequency	$\frac{dpH}{dt}$	$\frac{\frac{dpH}{dt}}{\frac{dpH}{dt}_{NU}}$	$\frac{dEC}{dt}$	$\frac{\frac{dEC}{dt}}{\frac{dEC}{dt}_{NU}}$
No ultrasound	-0.0051	1	0.0216	1
24 kHz	-0.0137	2.7	0.0626	2.9
40 kHz	-0.0151	2.9	0.0348	1.6
580 kHz	-0.0290	5.7	0.1185	5.5
860 kHz	-0.0210	4.1	0.0576	2.7
1140 kHz	-0.0311	6.1	0.0706	3.3

Table 1. The slopes of decrease of pH and increase of EC over time for the different frequencies. Additionally, the relative slopes compared to no ultrasound (NU) are listed.

Amplitude	$\frac{dpH}{dt}$	$\frac{\frac{dpH}{dt}}{\frac{dpH}{dt}_{NU}}$	$\frac{dEC}{dt}$	$\frac{\frac{dEC}{dt}}{\frac{dEC}{dt}_{NU}}$
20 %	-0.0197	3.9	0.0148	0.7
40 %	-0.0119	2.3	0.0254	1.2
60 %	-0.0097	1.9	0.0332	1.5
80 %	-0.0148	2.9	0.0500	2.3
100 %	-0.0137	2.7	0.0626	2.9

Table 2. The slopes of decrease of pH and increase of EC over time for the different amplitudes at frequency 24 kHz. Additionally, the relative slopes compared to no ultrasound (NU) are listed.

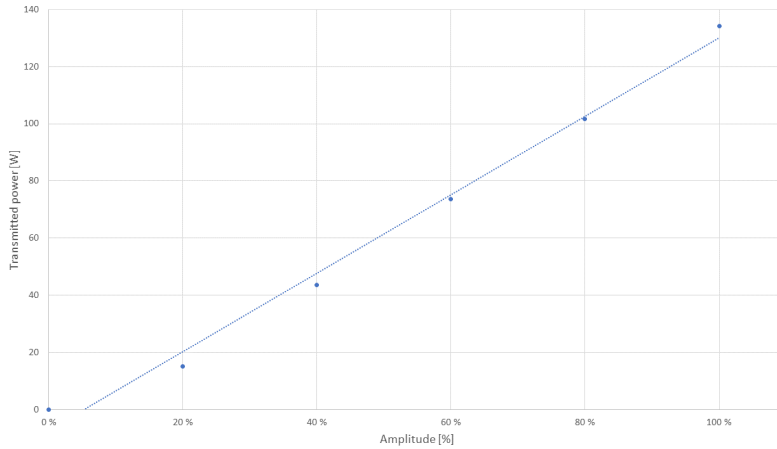


Figure 4. Relationship between acoustic pressure amplitude and acoustic power transferred to the system for 24 kHz ultrasound applied to a system containing 1200 mL water. The dotted line is a linear curve fitting to the data points.

The pH development shows a negative trend throughout all the experiments. In general, the negative slope is steeper when ultrasound is used compared to experiments without ultrasound. One explanation for the negative trend when ultrasound is not used is that deionized water was used to conduct the experiments. This water is neutral until it comes into contact with air. When

that happens, CO₂ gas starts dissolving in the water, making it slightly acidic. This process is continuing throughout the experiment because the glass vessels are open to the atmosphere, explaining the decay in pH. Further, the experiments with ultrasound induce an additional effect making the slope even more negative. The EC measurement is an indication of the amount of ions in the solution because electrically charged ions increase the electric conductivity. The EC is increasing gradually during the experiment for no ultrasound and the increase is steeper when ultrasound is used. One can understand the change of pH and EC over time as measures of sonochemical activity. In general, the sonochemical activity is high for high temperatures and pressures generated from the cavitation bubble collapse. This occurs at lower frequencies where large bubbles create high pressure and temperature, and at a large number of bubbles i.e. at higher frequencies. Therefore, there should be a best point at medium frequencies where radical production is high. At 580 kHz both the pH and EC- slopes are relatively steep, and this might indicate closeness to a point of high sonochemical activity. It is not favourable to have a decrease in pH in the water downstream a hydropower plant. It is best to avoid using frequencies that produce the steepest gradients of pH although the increase of pH when exposing water to ultrasound for a short amount of time is expected to be very small.

5. Conclusions

From the experiments it is found that the degassing effect is dependent on both acoustic power and frequency. Various phenomenon introduced by acoustic cavitation results in a high degassing effect for low frequencies around 24 kHz and higher frequencies around 860 kHz with a less effective region in between them. The sonochemical activity is high for medium frequencies around 580 kHz and should be avoided in degassing purposes for environmental reasons. The increase in power results in a higher degassing efficiency, and the power must be increased to maintain the degassing efficiency when the sonicated water volume is increased. The fastest completed degassing of 1200 mL water from 230 % saturation with a frequency of 24 kHz and a transmitted acoustic power of 134 W was measured to take about 20 minutes.

The presented results show that the application of ultrasound on oxygen-supersaturated water is making the degassing process more effective. Although, some challenges for future work are revealed. The sonochemical activity that is initiated when ultrasound is applied to water creates highly reactive radicals contributing to lowering the pH and increase the electrical conductivity. The extent of these phenomenon needs to be further investigated to ensure good water quality in the water systems. Additionally, the exposure time of ultrasound in these experiments have been in the order of twenty minutes. In a hydropower system this time may be in the order of one second, and proving that the concept works in cases of smaller exposure times will become an important task in further research.

References

- [1] Ulseth O *Norsk vannkraft- kilden til fornybarsamfunnet* EnergiNorge, Oslo, 2014
- [2] Ebel W L and Raymond H L *Effect of Atmospheric Gas Supersaturation on Salmon and Steelhead Trout of the Snake and Columbia Rivers* mfr paper 1191, 38 (7) , 1976
- [3] Tekle T *Overmetning av oppløst luft i vann fra kraftverk- årsaksforhold, skadevirkninger og mottiltak*. Norges hydrodynamiske laboratorier, 1983
- [4] Berg A *Air entrainment and supersaturation of dissolved air in a shaft under atmospherical and reduced pressure conditions* Journal of Hydraulic Research 30:3, pp. 327-340, 1992
- [5] Bouck G R *Etiology of Gas Bubble Disease* Transactions of the American Fisheries Society 109 pp. 703-707, 1980
- [6] Eskin D G *Ultrasonic Degassing of Liquids* Power Ultrasonics: Applications of High-Intensity Ultrasound pp. 611-631, 2015
- [7] Colt J *Solubility of Atmospheric Gases in Freshwater* Computation of Dissolved Gas Concentration in Water as Functions of Temperature, Salinity and Pressure (Second Edition) pp. 1-71, 2012
- [8] Yasui K *Acoustic Cavitation and Bubble Dynamics* Springer Nature, vol.8, isbn: 978-3-319-68236-5, 2018

- [9] Legay M, Gondrexon N, Le Person S, Boldo P and Bontemps A *Enhancement of Heat Transfer by Ultrasound: Review and Recent Advances* International Journal of Chemical Engineering, 2011
- [10] Islam M H, Pollet B G and Burheim O S *Sonochemical and sonoelectrochemical production of hydrogen* Ultrasonics Sonochemistry 51 pp. 533-555, 2019
- [11] Kasaai M R *Input power-mechanism relationship for ultrasonic irradiation: Food and polymer applications* Natural Science 5 pp.14-22, 2013
- [12] Ashokkumar M *Handbook of Ultrasonics and Sonochemistry* Springer Science, Singapore, 2016
- [13] Ingebrigtsen L M *Effects of Ultrasonic Frequency, Acoustic Power, and Liquid Height on Radical Production in a Sonochemical Reactor* NTNU, 2019
- [14] Brotchie A, Grieser F and Ashokkumar M *Effect of Power and Frequency on Bubble-Size Distributions in Acoustic Cavitation* Physical Review Letters 102 (8), 2009
- [15] Leong T, Ashokkumar M and Kentish S *The fundamentals of power ultrasound-A review* , SPRINGER SINGAPORE PTE LTD, November 2011
- [16] Lindström O *Physico-Chemical Aspects of Chemically Active Ultrasonic Cavitation in Aqueous Solutions* The Journal of the Acoustical Society of America 27 pp.654, 1955
- [17] Iida Y, Yasui K, Tuziuti T and Sivakumar M *Sonochemistry and its dosimetry* Microchemical Journal 80, pp. 159-164, 2005
- [18] Ratoarinoro F, Contamine A M, Wilhelm J, Berlan H and Delmas H *Power Measurements in Sonochemistry* Ultrasonics Sonochemistry 2.1, pp. 43-47, 1995

A.2 CFD-calculation details

y^+ -values for turbulent flow cases

The y^+ values in the two geometries for the turbulent flow cases are shown in Figures 7.1, 7.2, 7.3 and 7.4.

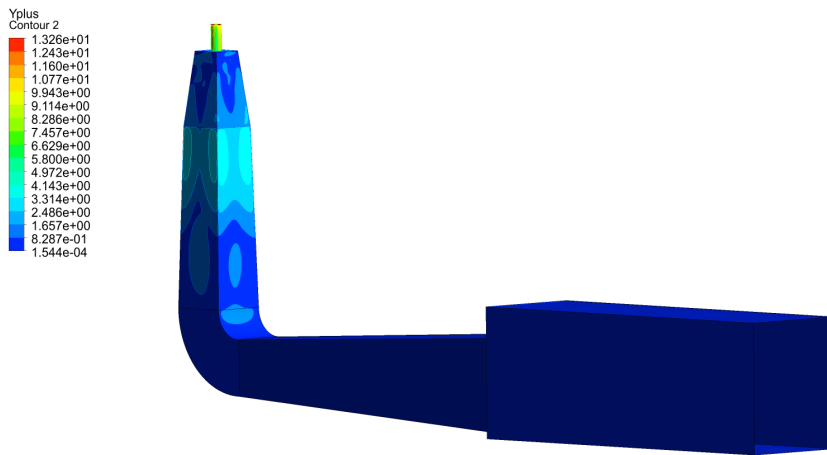


Figure 7.1: y^+ values for single-inlet turbulent flow case with flow rate 1 L/s.



Figure 7.2: y^+ values for double-inlet turbulent flow case with flow rate 1 L/s.

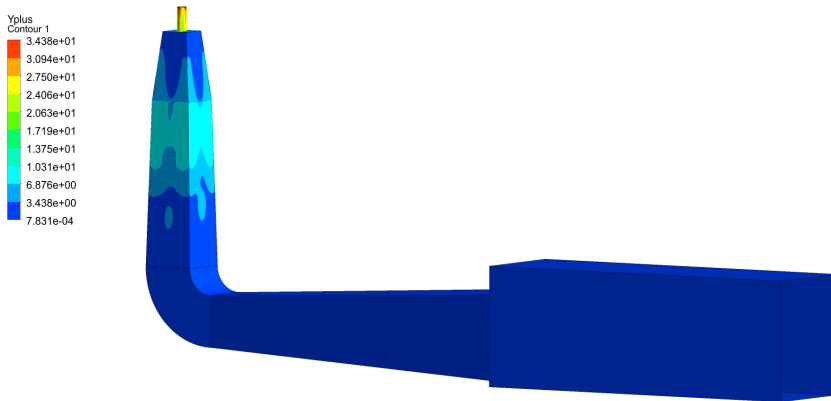


Figure 7.3: y^+ values for single-inlet turbulent flow case with flow rate 4 L/s.

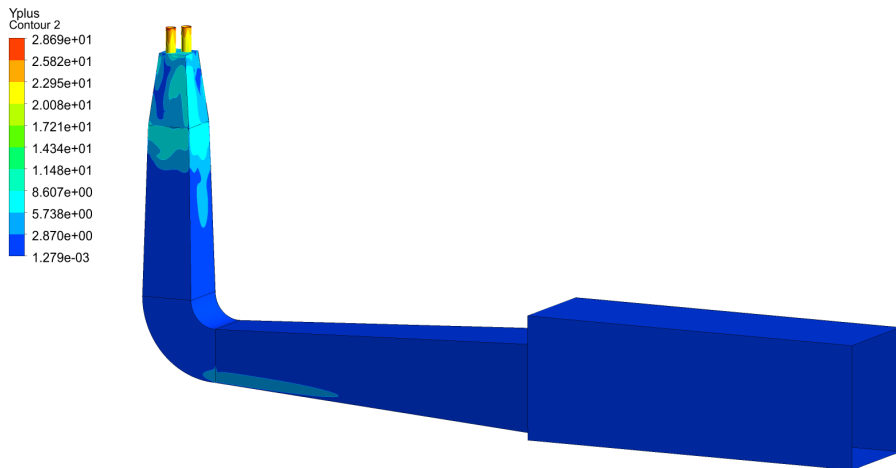


Figure 7.4: y^+ values for double-inlet turbulent flow case with flow rate 4 L/s.

Convergence history

The logged convergence history for the CFD-simulations are given in Figures 7.5, 7.6, 7.7, 7.8, 7.9, 7.10, 7.11, 7.12, 7.13 and 7.14.

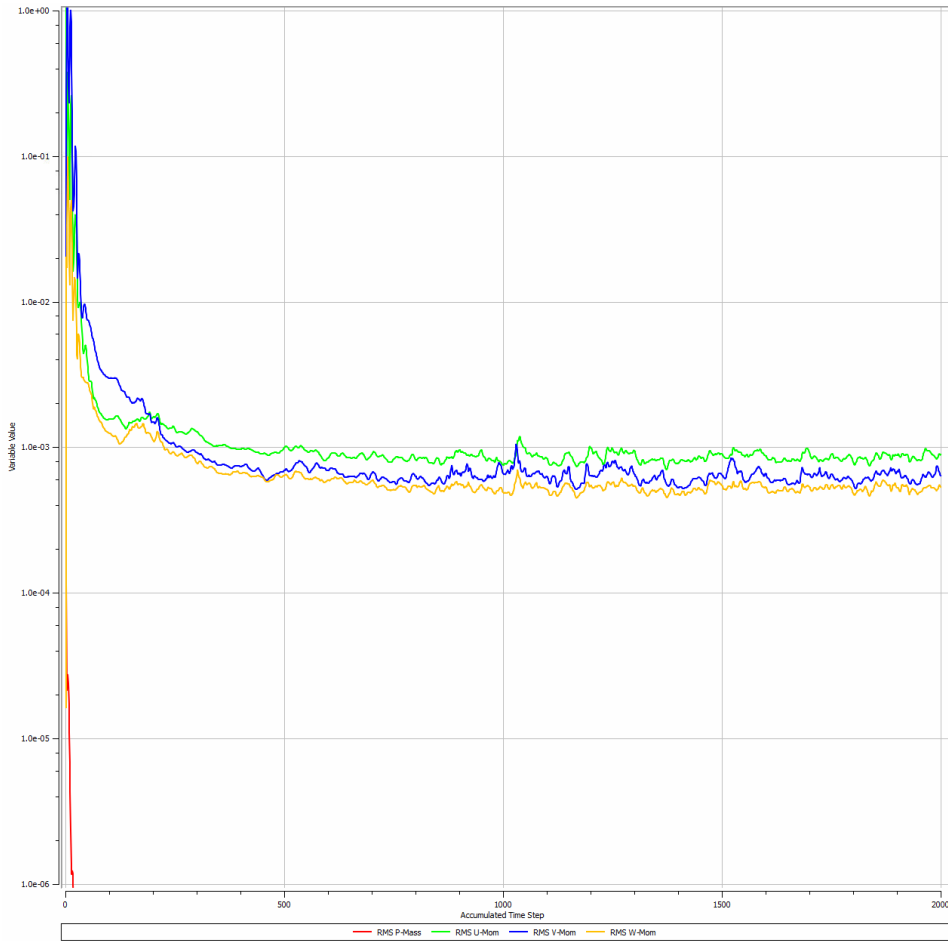


Figure 7.5: Convergence history for mass, momentum and pressure for laminar flow case on geometry type 1.

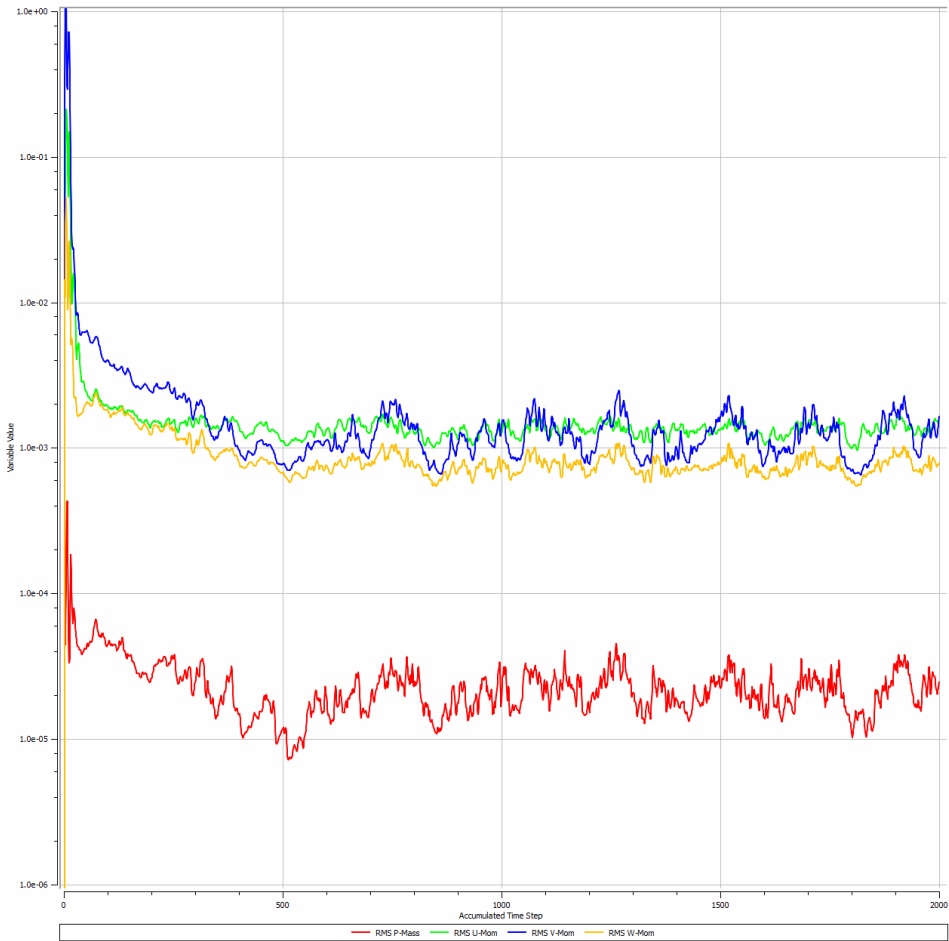


Figure 7.6: Convergence history for mass, momentum and pressure for laminar flow case on geometry type 2.

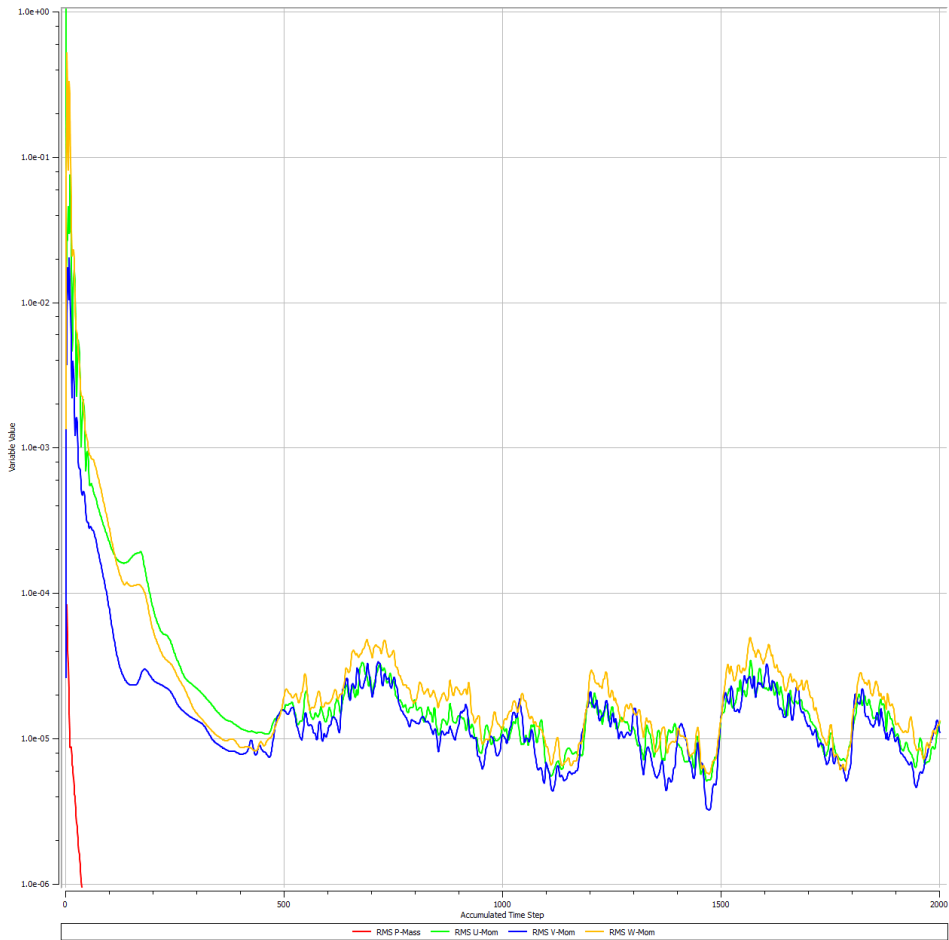


Figure 7.7: Convergence history for mass, momentum and pressure for turbulent flow case with flow rate 1 L/s on geometry type 1.

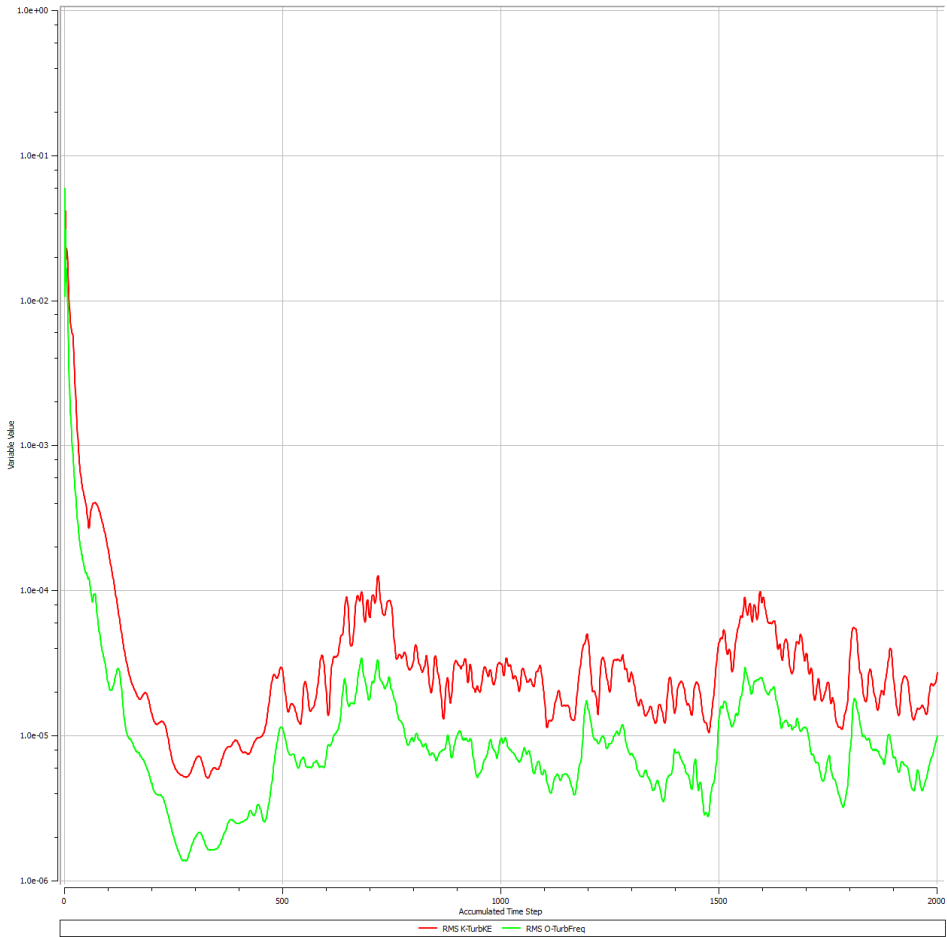


Figure 7.8: Convergence history for turbulence quantities for turbulent flow case with flow rate 1 L/s on geometry type 1.

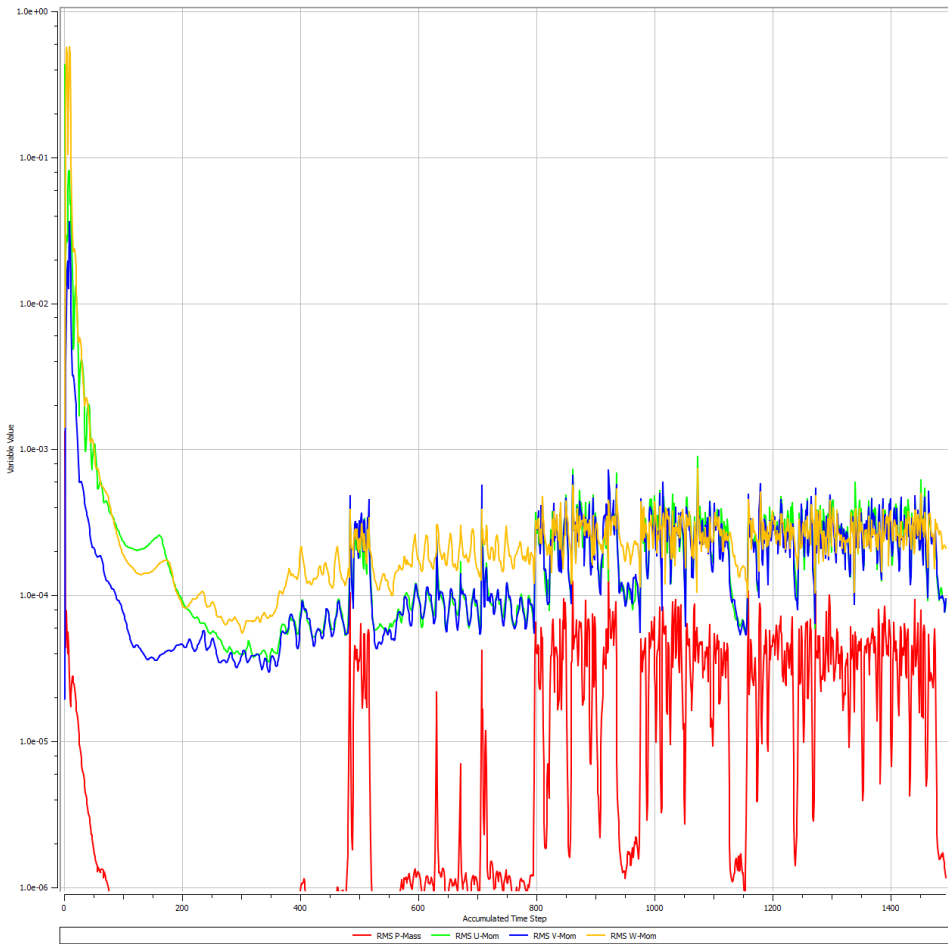


Figure 7.9: Convergence history for mass, momentum and pressure for turbulent flow case with flow rate 1 L/s on geometry type 2.

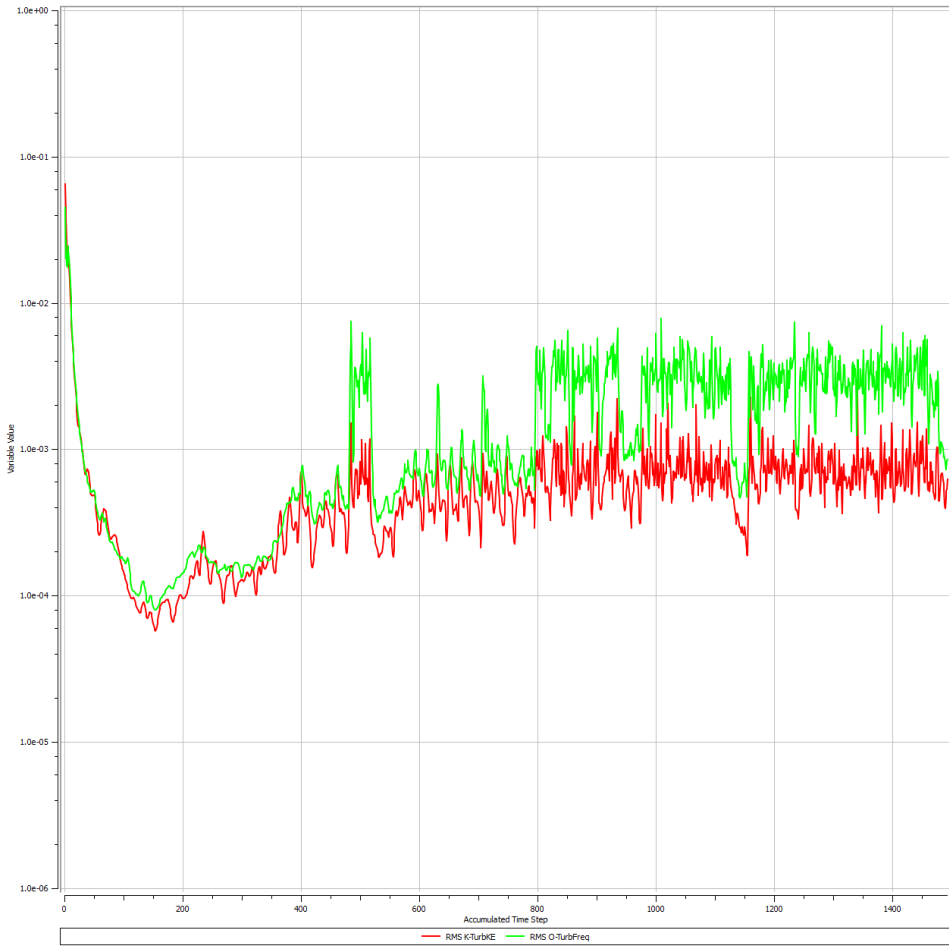


Figure 7.10: Convergence history for turbulence quantities for turbulent flow case with flow rate 1 L/s on geometry type 2.

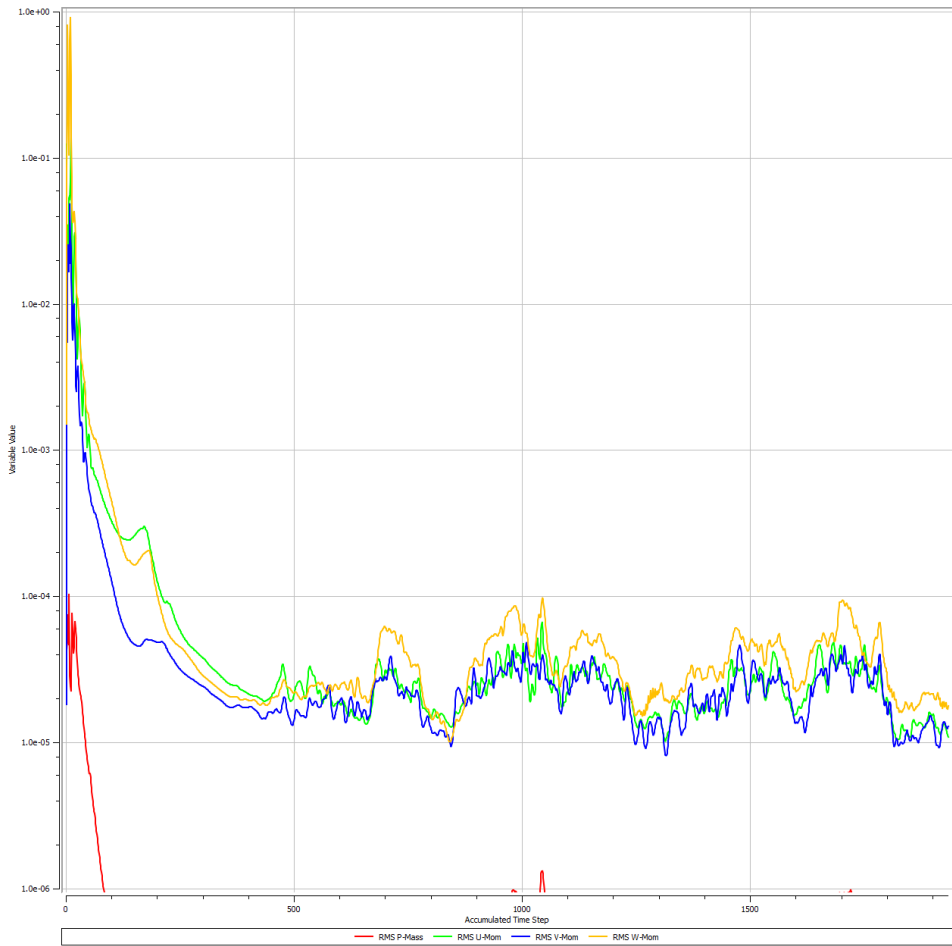


Figure 7.11: Convergence history for mass, momentum and pressure for turbulent flow case with flow rate 4 L/s on geometry type 1.

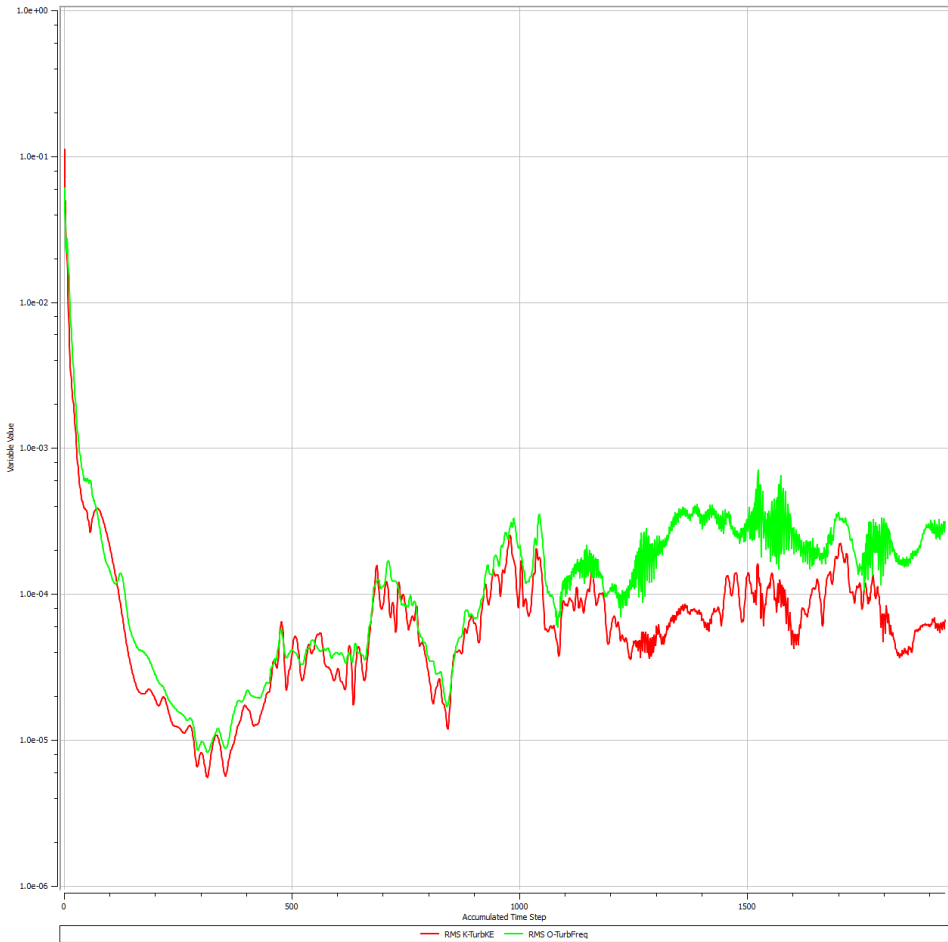


Figure 7.12: Convergence history for turbulence quantities for turbulent flow case with flow rate 4 L/s on geometry type 1.

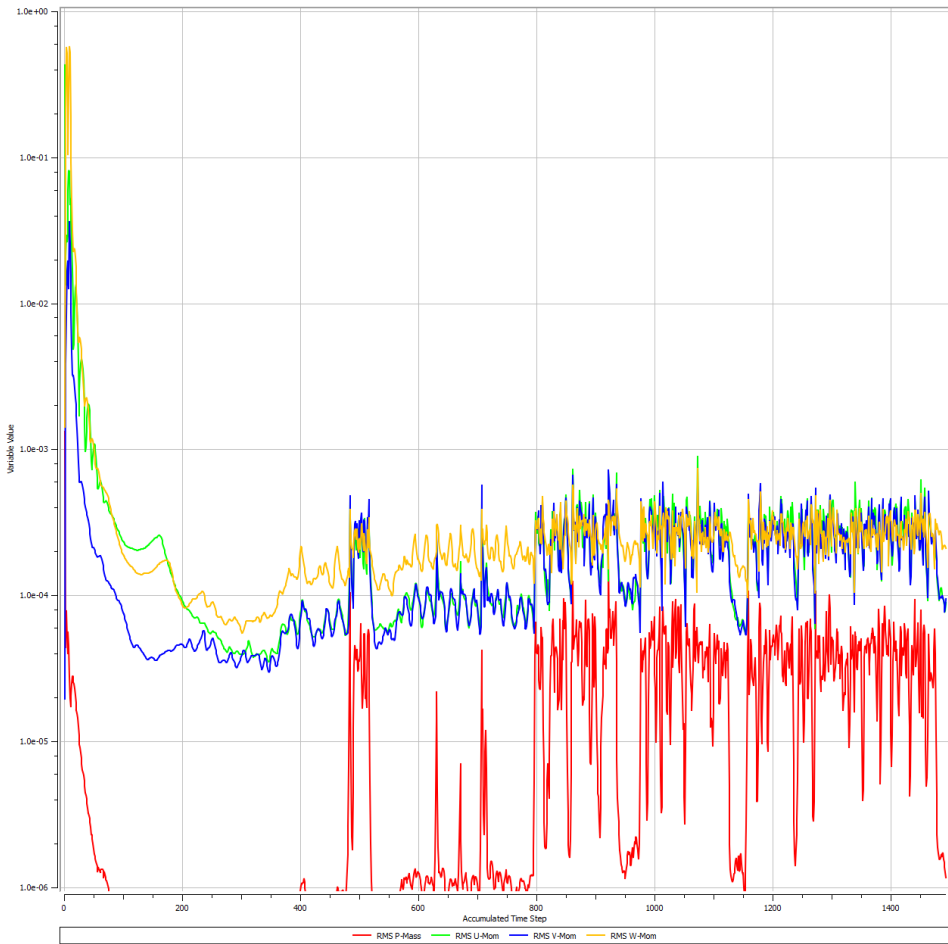


Figure 7.13: Convergence history for mass, momentum and pressure for turbulent flow case with flow rate 4 L/s on geometry type 2.

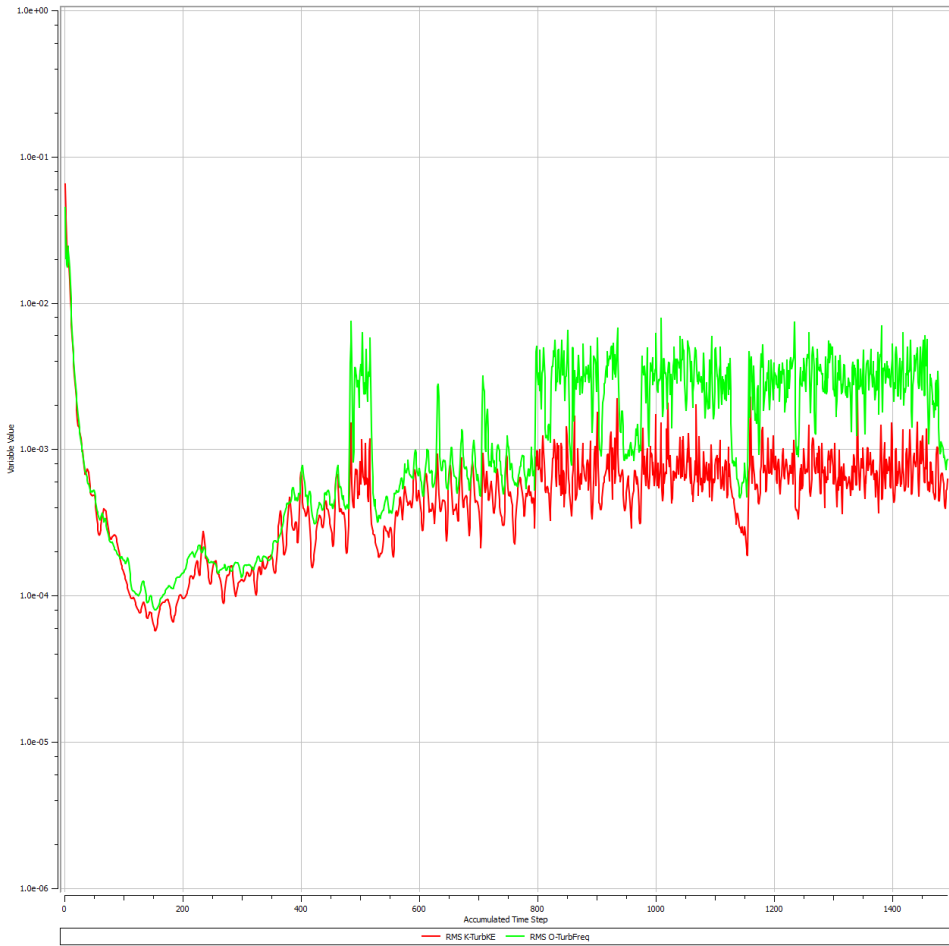


Figure 7.14: Convergence history for turbulence quantities for turbulent flow case with flow rate 4 L/s on geometry type 2.

A.3 MATLAB script for flow calculations

```

clear all
close all
clc
%-----
% This script is looking into properties of the different parts of the
% completed setup at different flow-rates.
%-----
% Constants and properties
g = 9.81; % Gravitational constant m/s^2
rho = 998; % Water density kg/m^3
mu = 0.0010256; % Dynamic viscosity kg/ms
Q = 0:0.00005:0.00495; % Flow rate in the setup in
    m^3/s
f_avg = 0.03; % Friction factor in flume
f_hose = 0.03; % Friction factor in hose.
%-----
% The physical dimentions of the setup:

    % Before hose inlet
    B = 0.3; % Diameter of measurement
section m

    % Inlet hose(es)
    d = 0.04; % Hose diameter m
    A = pi()*(d/2)^2; % Flow area in hoses m^2
    L_hose = 5; % Hose length, m

    % Inlet diffuser
    ih_ID = 0.08; % Inlet height inlet diffuser, m
    oh_ID = 0.125; % Outlet height inlet diffuser,
m

    L_ID = 0.2; % Length inlet diffuser, m
    beta_ID = 6.4; % Expansion angle deg

    % Pre-bend diffuser
    ih_PBD = 0.125; % Inlet height pre-bend
diffuser, m
    oh_PBD = 0.15; % Outlet height pre-bend
diffuser, m
    L_PBD = 0.48; % Length inlet pre-bend, m
    beta_PBD = 1.5; % Expansion angle deg

    % Bend
    d_h_bend = 0.15; % Bend dimention(height and
depth) m
    A_bend = (d_h_bend)^2; % Flow area in bend m^2
    R_D = 1.0; % R/D ratio in the bend

    % Post-bend diffuser
    ih_OBD = 0.15; % Inlet height post-bend
diffuser, m

```

```

        oh_OBD = 0.25;                % Outlet height post-bend
diffuser, m
        L_OBD = 1.0;                  % Length post-bend diffuser, m
        beta_OBD = 3;                % Expansion angle deg

        % Flume
        W = 0.3;                      % Flume width m
%-----
%Calculating average flow velocities in different parts of the setup
        % Inlet hose(es)
        V_1 = Q./A;                   % Velocity in hose m/s, one hose
        V_2 = Q./(2*A);               % Velocity in hose m/s, two hoses
        % Bend
        V_bend = Q./A_bend;           % Velocity in bend m/s
        % Inlet diffuser
        V_avg_ID = Q./((ih_ID^2 + oh_ID^2)/2);
                                                % Average velocity in inlet diffuser
m/s
        % Pre-bend diffuser
        V_avg_PBD = Q./((ih_PBD^2 + oh_PBD^2)/2);
                                                % Average velocity in pb diffuser m/
S
        % Post-bend diffuser
        V_avg_OBD = Q./((ih_OBD^2 + oh_OBD^2)/2);
                                                % Average velocity in post b
diffuser m/s
%-----
% Calculations for hoses

% Re in the hoses leading to the draft tube inlet
        %One hose
        Re_1 = rho*V_1*d./mu;

        figure(1)
        plot(Q*1000, Re_1)
        title('Re for varying flow for one pipe inlet')
        xlabel('Q[L/s]')
        ylabel('Re')
        grid on

        %Two hoses
        Re_2 = rho*V_2*d./mu;

        figure(2)
        plot(Q*1000, Re_2)
        title('Re for varying flow for two pipe inlet')
        xlabel('Q[L/s]')
        ylabel('Re')
        grid on

% Turbulent entrance length in the hoses depending on Re:

        L_c = d*1.359*(Re_1).^(1/4); % m

```

```

figure(3)
plot(Q*1000, L_c)
title('Entrance length for changing flow rate')
xlabel('Q [L/s]')
ylabel('L_c [m]')
grid on

%-----
% Calculations in bend

% Finding K_b
Re_bend = rho*V_bend*d_h_bend./mu;

K_b = 0.388* (0.95 + (4.42*(R_D)^-1.96))*R_D^0.84*Re_bend.^-0.17;

figure(4)
plot(Q*1000, K_b)
%title('Bend loss coefficient with flow rate ')
xlabel('Q [L/s]')
ylabel('K_b')
grid on

%-----
% Flow through sudden expansion

K_SE_1 = (1-((d)^2/(d_h_bend)^2))^2; % Sudden expansion into
inlet
K_SE_2 = (1-((oh_OBD)^2/(W)^2))^2; % Sudden expansion into
flume

% Flow through sudden contraction

K_SC = 0.42*(1-((d)^2/(B)^2)); % Sudden contraction into pipe

%-----
% Loss in diffusers

K_DIFF_INLET = 2.61 * sin(beta_ID*pi()/180)* ...
(1-((ih_ID)^2/(oh_ID)^2))^2 + f_avg*L_ID/((ih_ID+oh_ID)/2) ;

K_DIFF_PRE = 2.61 * sin(beta_PBD*pi()/180)* ...
(1-((ih_PBD)^2/(oh_PBD)^2))^2 + f_avg*L_PBD/ ((ih_PBD
+oh_PBD)/2);

K_DIFF_POST= 2.61 * sin(beta_OBD*pi()/180)*...
(1-((ih_OBD)^2/(oh_OBD)^2))^2 + f_avg*L_OBD/ ((ih_OBD
+oh_OBD)/2);

%-----
% Total loss in all sections measured in mVc
%-----
% SC loss into hoses, friction loss in hoses, SE loss into inlet
diffuser,
% loss in inlet diffuse, loss in pre-bend diffiser, loss in bend, loss
in
% post-bend diffuser, SE loss into open flume.

```

```

% SC loss into hoses
h_SC = K_SC * V_1.^2/(2*g); % m
% Inlet hose(s)
h_loss_hose_1 = f_hose.* L_hose* V_1.^2/(2*g*d); % m
% SE into inlet diffuser
h_SE_1 = K_SE_1 * V_1.^2/(2*g); % m
% Inlet diffuser
h_ID = K_DIFF_INLET * V_avg_ID.^2 /(2*g); % m
% Pre-bend diffuser
h_PBD = K_DIFF_PRE * V_avg_PBD.^2 /(2*g); % m
% Bend
h_b = K_b .* V_bend.^2/(2*g); % m
% Post-bend diffuser
h_OBD = K_DIFF_POST * V_avg_OBD/(2*g); % m
% SE into open flume
h_SE_2 = K_SE_2 * (Q/oh_OBD^2).^2/(2*g); % m

h_tot = h_SC +h_SE_1+h_ID+h_PBD+ h_b+h_OBD+h_SE_2; % m + h_loss_hose_1

figure(6)
plot(Q*1000, h_tot)
title('Total loss in flow system minus loss in inlet pipe for varying
flow rate')
xlabel('Flow rate [L/s]')
ylabel('System loss [m]')
grid on

%-----
% Flow rate resulting from a given total head
%-----
H = 0.01:0.01:1; % Total head = pressure - loss
Q_res = sqrt(2*g*H)*A*1000; % L/s Flow resulting from given total
head

figure (7)
plot(H,Q_res)
title('Flow rate resulting from a given total head')
xlabel('Water column height minus system loss[m]')
ylabel('Resulting flow rate [L/s]')
grid on

%-----
% Residence time for different flow rates.
%-----
L_p = 0.66; % probe length [m]
t_res = L_p./V_avg_OBD; % residence time
[s]

figure(8)
plot(Q*1000,t_res)
title('Residence time for different flow rates')
xlabel('Q [L/s]')
ylabel('t_{residence} [s]')

```

```

grid on

%-----
% Plotting the pipe loss for different pipe length and flow rates as
% an example.
%-----

L_hose = 0.1:0.1:10;
Q = [0.004,0.003,0.002,0.001,0.00035];
figure(9)
h_loss_hose_1 = f_hose.* L_hose* Q(1)/(pi()*(d/2)^2*(2*g*d));
plot(L_hose,h_loss_hose_1)
hold on

h_loss_hose_1 = f_hose.* L_hose* Q(2)/(pi()*(d/2)^2*(2*g*d));
plot(L_hose,h_loss_hose_1)
hold on

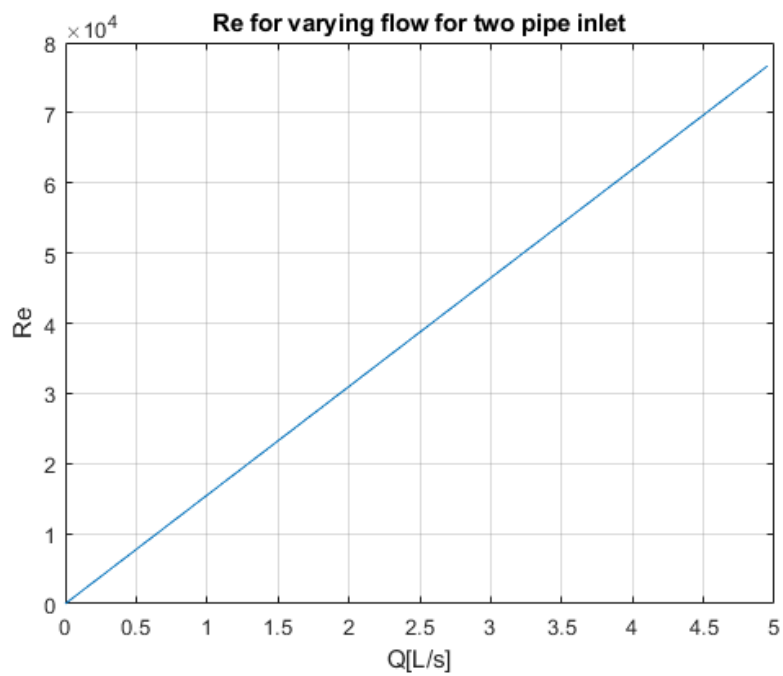
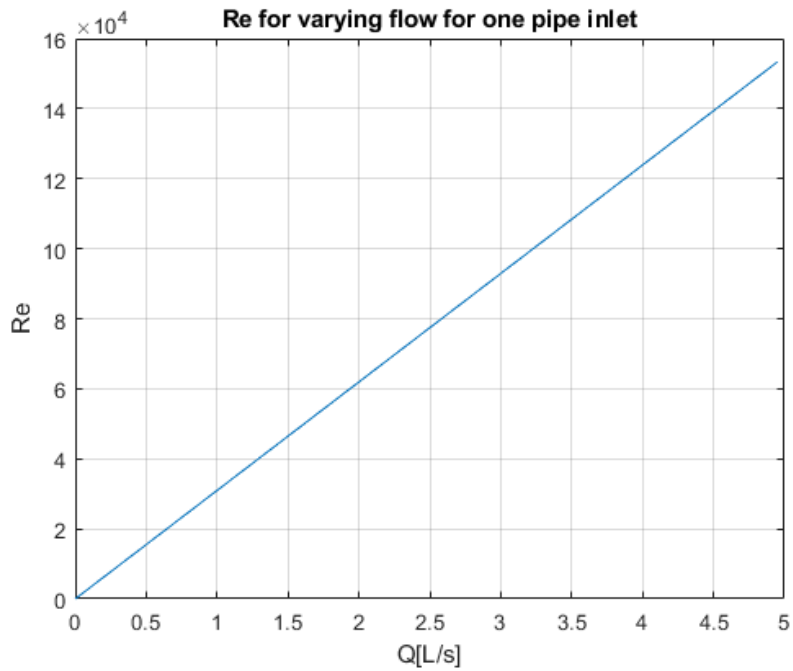
h_loss_hose_1 = f_hose.* L_hose* Q(3)/(pi()*(d/2)^2*(2*g*d));
plot(L_hose,h_loss_hose_1)
hold on

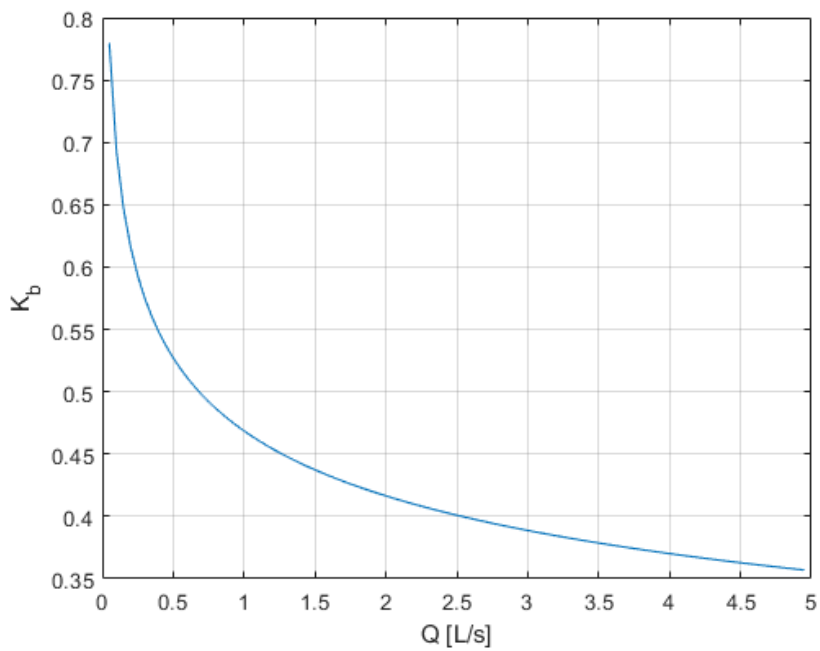
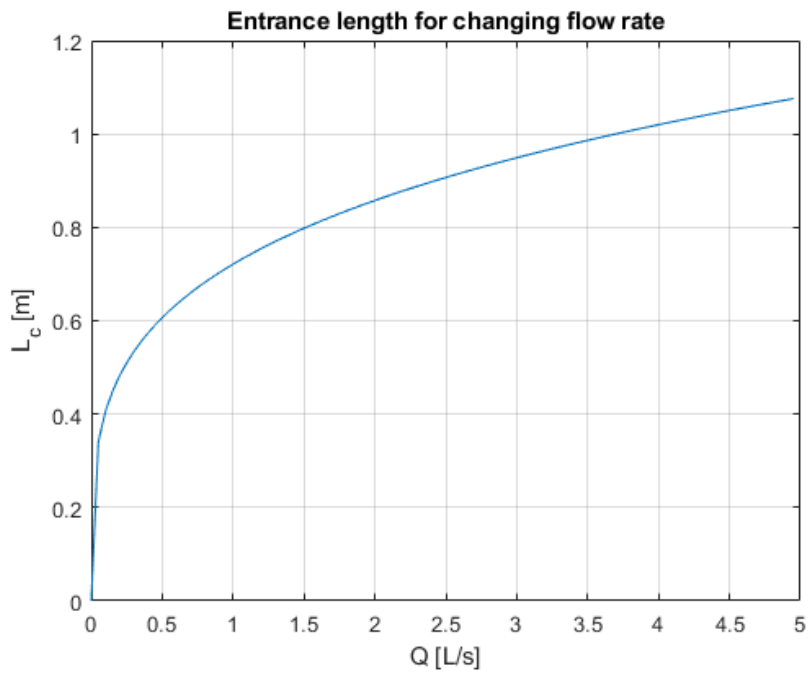
h_loss_hose_1 = f_hose.* L_hose* Q(4)/(pi()*(d/2)^2*(2*g*d));
plot(L_hose,h_loss_hose_1)
hold on

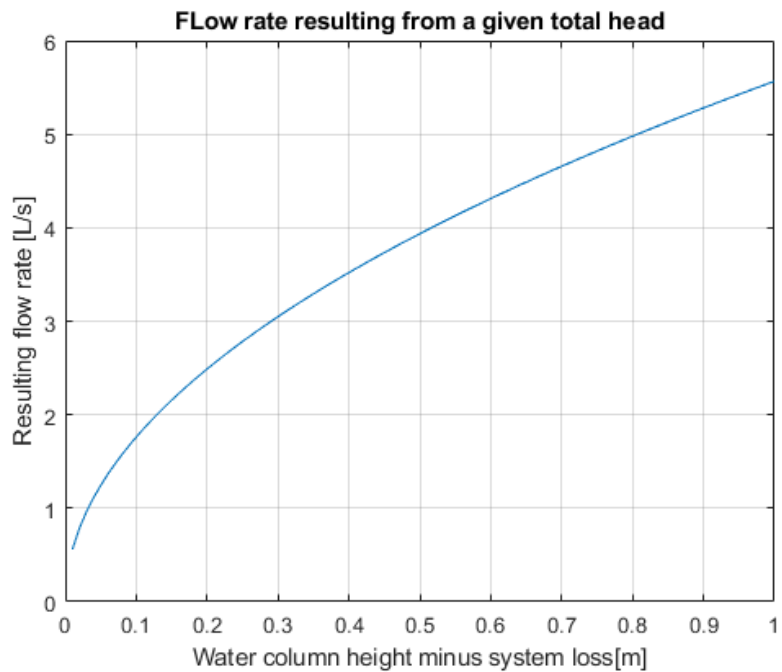
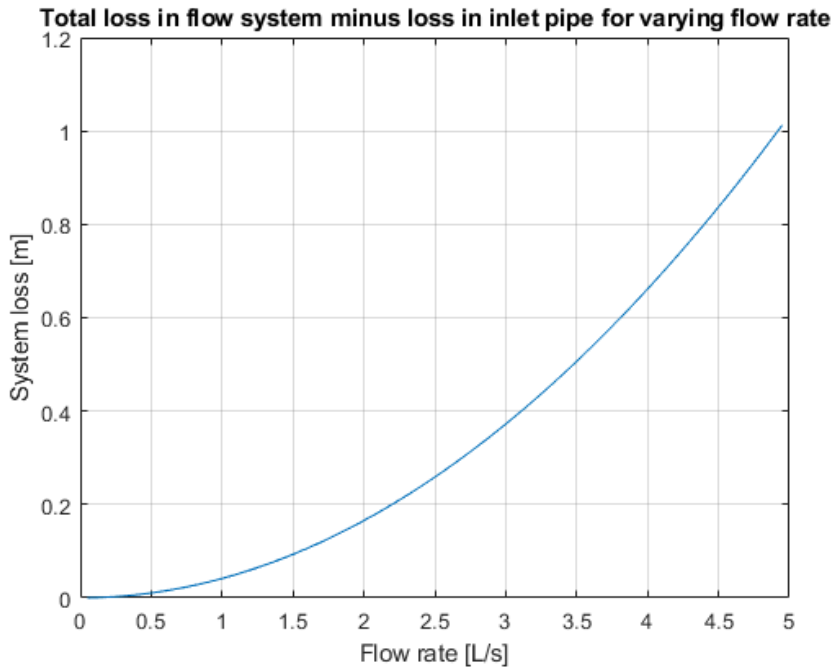
h_loss_hose_1 = f_hose.* L_hose* Q(5)/(pi()*(d/2)^2*(2*g*d));
plot(L_hose,h_loss_hose_1)
hold on

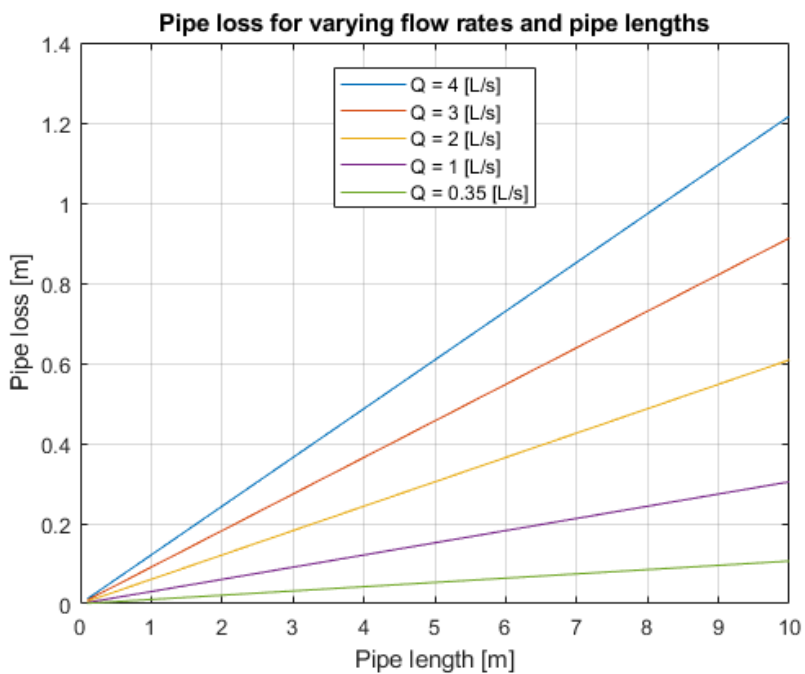
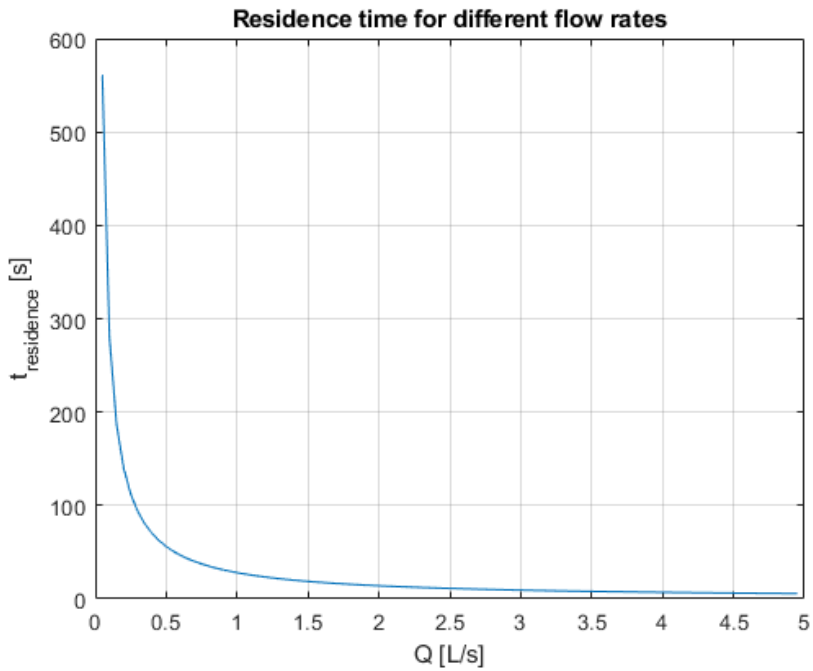
legend('Q = 4 [L/s]', 'Q = 3 [L/s]', 'Q = 2 [L/s]', 'Q = 1 [L/s]', ...
       'Q = 0.35 [L/s]', 'Location' , 'Best')
title('Pipe loss for varying flow rates and pipe lengths')
xlabel('Pipe length [m]')
ylabel('Pipe loss [m]')
grid on
hold off

```









Published with MATLAB® R2018b